Measurement of Relative Intensity of the Discrete γ Rays From the Thermal Neutron Capture Reaction ^{155,157}Gd(n,γ) Using ANNRI Detector (JPARC)

2017, September

PRETAM KUMAR DAS

Division of Mathematics and Physics

Graduate School of Natural Science and Technology

(DOCTOR'S COURSE)

OKAYAMA UNIVERSITY

Dissertation submitted to
Graduate School of Natural Science and Technology
of
Okayama University
for
partial fulfillment of the requirements
for the degree of
Doctor of Philosophy.

Written under the supervision of

Professor **MAKOTO SAKUDA**

OKAYAMA UNIVERSITY, September 2017

TO WHOM IT MAY CONCERN

We hereby certify that this is a typical copy of the original doctor thesis of
Mr. Pretam Kumar Das

Signature of

the Supervisor

Prof. Makoto Sakuda

Seal of

Graduate School of

Natural Science and Technology

OKAYAMA UNIVERSITY

Abstract

Graduate School of Natural Science and Technology
Division of Mathematics and Physics

Doctor of Philosophy

by **PRETAM KUMAR DAS**

The thermal neutron capture reaction on enriched gadolinium targets (^{155}Gd, ^{157}Gd isotopes) has been studied using Accurate Neutron-Nucleus Reaction Instruments (ANNRI) Germanium Spectrometer at Materials and Life Science Experimental Facility (MLF) of the Japan Proton Accelerator Research Complex (JPARC), which provides the most intense pulsed neutron beam for neutron time-of-flight experiments in the world. The purposes of our experiments and analysis are to provide precise γ-ray spectrum of ^{155,157}Gd(n,γ) reactions and provide precise Gd decay model to neutrino physics field and other related fields.

The γ rays produced from ^{155,157}Gd(n, γ) reactions were measured. The photo-peak efficiencies of the spectrometer have been calibrated from 0.1 to 9 MeV using γ rays from the standard radioactive sources (^{60}Co, ^{137}Cs, ^{152}Eu) and prompt γ rays from ^{35}Cl(n, γ) reaction. The relative intensities of prominent discrete γ rays produced from ^{155}Gd(n, γ) and ^{157}Gd(n, γ) reactions were measured. Our data of relative intensities from ^{157}Gd(n, γ) were found in fair agreement with the values published by the National Nuclear Data Center (NNDC) (CapGam). The relative intensities of prominent discrete rays from ^{155}Gd(n, γ) reaction were measured for the first time.

The properties of Gd nucleus and the previous Gd (n, γ) experiments have been reviewed. The accuracy of the γ-ray spectrum measurement for our thermal neutron capture experiments should be better than others, as we used most intense pulsed neutron beam in the world and used Germanium spectrometer with very high resolution in our experiments.

Contents

List of Figures

List of Tables

Dedicated To My Parents

And

My Teachers

Chapter 1

Introduction

1.1 Physics Background of Neutron-Nucleus Interaction

1.1.1 Characteristics of Neutrons

Neutrons (^1_0n) are charge neutral particle, so they can travel in a straight line. They deviate from their actual path only when they really collide with a nucleus. The interaction between neutron and nucleus is occurred only when the neutron goes inside the nucleus or very close to its boundary. Like γ rays, neutrons do not interact in matter via of Coulomb force. By interaction, a neutron may either totally be disappeared or be replaced by one or more secondary radiations, or else it may be changed its energy or direction significantly.

It is convenient to classify interactions of neutrons with nuclei of the matter according to the kinetic energy [1].

(a) Slow neutrons (0 <E< 100eV).

(i) Cold neutrons (<1 meV).

(ii) Thermal neutrons (< 0.5 eV).

(iii) Epithermal Neutrons (0.5 eV-50 eV).

(iv) Resonance neutrons (1eV-100 eV).

(b) Intermediate neutrons (1 keV<E< 500keV).

(c) Fast (high energy) neutrons (0.5MeV<E< 10 MeV).

(d) Very fast (very high energy) neutrons (10MeV<E< 50 MeV).

(e) Ultra fast (ultra-high energy) neutrons (E> 50 MeV).

1.1.2 Neutron Interaction with Nucleus

Neutrons can cause many different types of interactions depending on their energy. When a neutron comes into interaction with a nucleus, three types of interaction are possible (shown in Figure 1.1): (1) formation of compound nucleus (CN) (2) potential scattering and (3) direct reaction.

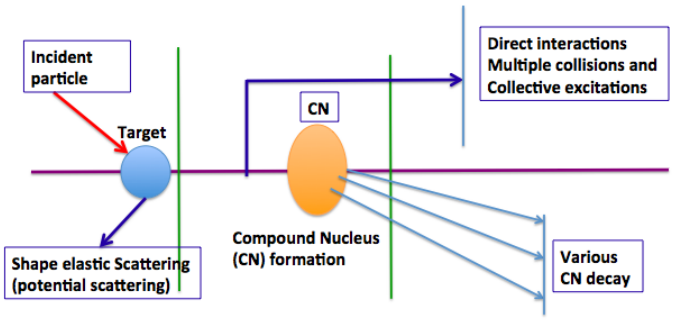

FIGURE 1.1: Formation and decaying of CN

(1) Formation of Compound Nucleus (CN)

The interaction which takes place in such a way that the incident particle is fully absorbed by the target nucleus and formed an excited compound nucleus (CN).
If the target nucleus is ${}^{A}_{Z}X$, then the CN formation can be represented as

$$ {}^{1}_{0}n + {}^{A}_{Z}X \rightarrow ({}^{A+1}_{Z}X)^{*} \rightarrow C^{*} \tag{1.1} $$

The energy of excitation of the CN is larger than the kinetic energy of the incident neutron. The CN will decay immediately after it formed. The de-excitation pathways for CN are given below.

TABLE 1.1: De-excitation pathways for CN

${}^{1}_{0}n + {}^{A}_{Z}X \rightarrow C^{*}$	$C^{*} \rightarrow {}^{A}_{Z}X + {}^{1}_{0}n$	Elastic resonant scattering (n,n)
	$C^{*} \rightarrow {}^{A}_{Z}X + {}^{1}_{0}n + \gamma$	Inelastic resonant scattering (n,n')
	$C^{*} \rightarrow {}^{A+1}_{Z}X + \gamma$	Radiative capture (n,γ)
	$C^{*} \rightarrow E + D$	Fission (n,f)
	$C^{*} \rightarrow {}^{A}_{Z-1}X + {}^{1}_{1}H$	Transmutation (n,p)
	$C^{*} \rightarrow {}^{A-3}_{Z-2}X + {}^{4}_{1}He$	(n,α) reaction
	$C^{*} \rightarrow {}^{A-2}_{Z}X + 2{}^{1}_{0}n$	(n, 2n), (n,3n)... reactions

(2) Potential Scattering

Potential scattering is a type of elastic scattering which can take place at any energy of the incident neutron. In potential scattering, formation of CN does not occur. It is a collision of the "billiard ball" type, where total energy is conserved.

$$ {}^{1}_{0}n + {}^{A}_{Z}X \rightarrow {}^{A}_{Z}X + {}^{1}_{0}n \tag{1.2} $$

It can also be known as a function of the forces which act on the neutron in the locality of the target nucleus. These forces depend on the dimensions and shape of the nucleus. At low energy, the cross-section of potential scattering for a target nucleus of radius R is

$$ \sigma_{ps} = 4\pi R^{2} \tag{1.3} $$

in the absence of resonance.

(3) Direct Reactions

Direct raction is a type of nuclear reaction which occurs so fast (within about 10^{-22}sec). A nuclear reaction is said to be a direct reaction if that reaction goes through directly from the initial state to the final state without forming an intermediate compound nucleus (CN). The higher energy neutrons (about 5 MeV) can be interacted with the nuclei by direct interaction. This interaction between neutron and nucleus results in the ejection of one or more nucleons. The cross-section of the direct nuclear reaction is proportional to the square of a matrix element and can be written as

$$M =< f|H|i > \tag{1.4}$$

where $|i >$ and $< f|$ are the wave functions of the initial and final systems and H is the part of the Hamiltonian responsible for the transition.

1.1.3 Reaction Mechanism with Different Neutron Energy

The type of interactions between the incident particle and the target nucleus depend both on the energy of the incident particle and mass of the nuclei. For light nuclei, the interaction has to be treated as individually. It is quite impossible to apply any general formulas describing nuclear reaction for light nuclei group. The reactions with intermediate nuclei (30<A<90) or heavy nuclei (A>90) are different types in the different energy region. Table 1.2 shows that the reaction mechanism of different incident energy particles (where el=elastic scattering, inel= inelastic scattering, Res= Resonance).

TABLE 1.2: Reaction mechanism for different incident energy [1]

Incident Energy (Incident Particle)	Intermediate nuclei(30<A<90)				Heavy nuclei (A>90)			
	n	p	α	d	n	p	α	d
Low energy (0-1 keV)	n(el), γ (Res)				γ, n(el) (Res)			
Intermediate energy (1-500 keV)	n(el), γ (Res)	n, γ, α (Res)	n, γ, p (Res)	p, n	n(el),γ (Res)			
High energy (0.5-10 MeV)	n(el), n(inel), p, α	n, p(inel), α	n, p, α(inel)	p, n, pn, 2n, d(inel)	n(el), n(inel), p, γ	n, p(inel), γ	n, p, γ	p, n, pn, 2n
Very high energy (10-50 MeV)	2n, n(inel), n(el), p, np,2p, α	2n, n, p(inel), np, 2p, α	2n, n, p, np, 2p, α(inel)	p, 2n, pn, 3n, d(inel)	2n, n(inel), n(el), p, pn, 2p, α	2n, n, p(inel), np, 2p, α	2n, n, p(inel), np, 2p, α(inel)	p, 2n, np, 3n, d(inel)

For neutron energy E_n <1MeV, (n,p) and (n,α) reactions are suppressed due to Coulomb barrier. For neutron energy E_n <200keV, only (n,n) and (n,γ) reactions are possible. For neutron energy E_n <1keV, (n,γ) dominates. For neutron energy E_n <1meV, diffraction is dominant. And for very high energy neutron E_n >10MeV, inelastic scattering (n,n$'$) and nuclear fission (n,f) are possible.

1.1.4 Neutron-Nucleus Interaction Mechanism with Optical Model

The interaction of nucleons with nuclei can also be represented by a complex potential. The basic knowledge of the optical model is that a nucleon may be elastically scattered by a nucleus or may be

gone through in different reactions. If the incident particle behaves like a wave, it may be scattered or it may be absorbed. This is similar to the refraction and absorption of a light wave by a medium with complex refractive index in optics. In nuclear physics, the imaginary part of the complex potential can be described a interaction which is responsible for all of the non-elastic reactions in a similar way as the imaginary part of the refractive index is responsible for the absorption of the light wave.

Feshbach el al. [2] found that the overall feature of the neutron cross-sections with nucleons could be reproduced very well by a complex neutron-nucleus potential of form $V = V_0(1 + i\xi)$ for r<R and V=0 for r>R. where ξ is a parameter which indicates an absorption for neutrons within nuclear matter, R is the nuclear radius and r is the distance between neutron and the nucleus. The total cross-sections as a function of energy as mass number [2] are shown in Figure 1.2 .

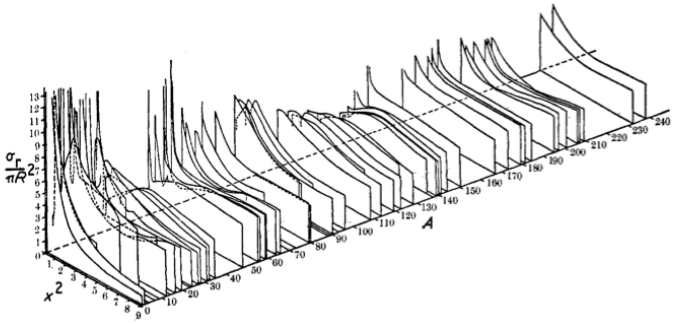

FIGURE 1.2: Observed neutron total cross-sections as a function of energy and mass number [2]

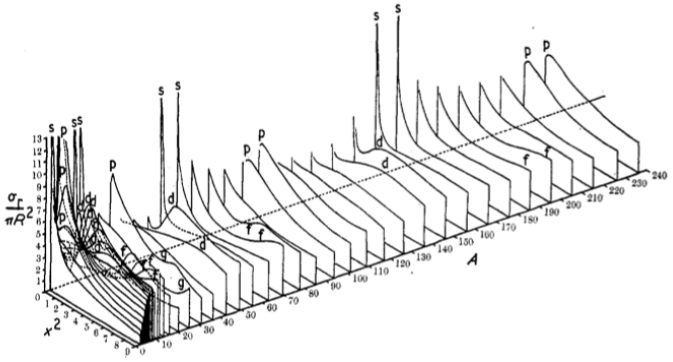

FIGURE 1.3: Calculated neutron total cross-section as a function of energy and mass number for a potential depth V_0=42 MeV [2]

Figure 1.3 shows the calculated neutron total cross-sections as a function of energy and mass number for a potential depth V_0=42 MeV, radius R=1.45 $A^{\frac{1}{3}}$fm and ξ=0.03 [2]. The energy ϵ can be expressed as $x^2 = A^{2/3}A/10(A+1)\epsilon$, where unit of ϵ is MeV. Good agreement between the calculation and theory established the necessity of the optical model and encourage to apply to wide range of nuclear interactions.

1.2 Physics of Neutron Capture Reaction

Low energy or slow neutrons are very important in disintegrating nuclei [3]. They have high probability to disintegrate nuclei because they can stay longer time inside the nucleus. For the non-fissionable nuclei, the only possible reaction is absorption reaction or capture reaction. Capture reactions result in the loss of a neutron coupled with the production of one or more γ rays. Capture cross-section is large for slow neutrons and it is inversely proportional to velocity [4].

Neutron capture ^{A}X(n,γ) is a reaction, in which the incident neutron is completely absorbed and a compound nucleus (CN) is formed. The excitation energy of the CN is the sum of the binding energy of neutron in the CN (neutron separation energy) plus the kinetic energy of the incident neutron. Then, the compound nucleus decays to its ground state by emitting electromagnetic energy as γ rays. The neutron capture reaction is given by

$$n + {}^{A}_{Z}X \rightarrow [{}^{A+1}_{Z}X]^{*} \rightarrow {}^{A+1}_{Z}X + \gamma \tag{1.5}$$

The neutron capture reaction is illustrated in Figure 1.4.

Among the natural elements, boron, cadmium, and gadolinium are the best absorbers for slow

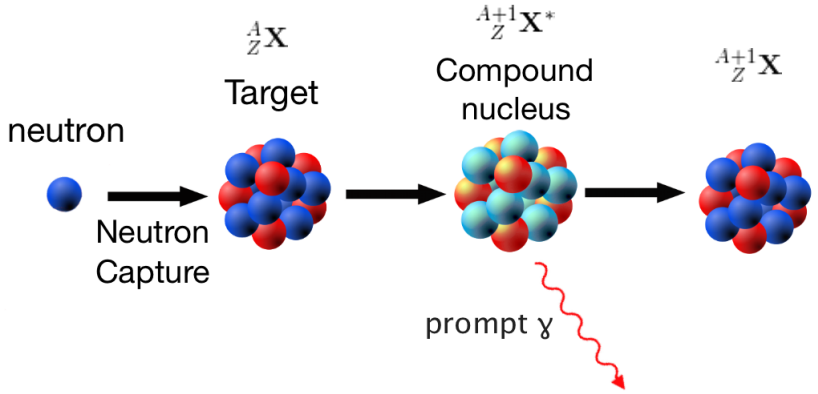

FIGURE 1.4: CN formation with n capture reaction

neutrons. The probability of the neutron capture reaction or (n,γ) reaction has increased greatly if the reaction is performed by very slow (low energy) neutrons.

The resonance spin can be written as

$$\vec{J} = \vec{I} + \vec{l} + \vec{S} \tag{1.6}$$

where, $\vec{I}$ be the spin of the target nucleus, $\vec{l}$ be the angular momentum of the incident neutron and $\vec{S}$ be the neuron spin ($S = \frac{1}{2}$). The neutrons neutrons with zero angular momentum (l=0) or s-wave neutrons interact with nuclei more strongly than the p-wave (l=1) neutrons or any higher angular momentum neutrons due to the centrifugal potential barrier. We have two possible spin state $J = I + S$ and $J = I - S$ for s-wave neutrons resonances in odd-A targets

1.3 Neutron Capture Nucleosynthesis

Neutron capture has played a very important role in nucleosynthesis. It is well known that the heavy elements, beyond iron (Fe) were formed in neutron capture nucleosynthesis process [5]. Elements beyond the Fe can not be produced by charge particle reaction due to higher Coulomb barrier. Neutron capture nucleosynthesis describes two pathways: (i) the slow neutron capture (s-process) and (ii) the rapid neutron capture (r-process). Depending on the neutron flux and neutron density, it is decided whether it happens s or r process.

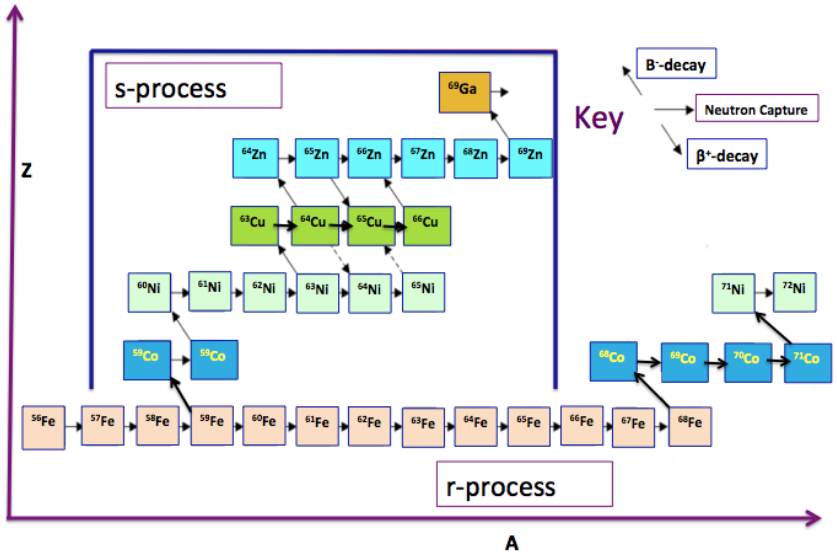

FIGURE 1.5: Neutron capture in nucleosynthesis

Consider neutron capture on target nucleus ${}^{A}_{Z}\mathrm{X}$

$$ {}^{A}_{Z}X + n \rightarrow {}^{A+1}_{Z} X + \gamma \tag{1.7} $$

if ${}^{A+1}_{Z}X$ is stable , then again capture neutron

$$ {}^{A+1}_{Z}X + n \rightarrow {}^{A+2}_{Z} X + \gamma \tag{1.8} $$

and if ${}^{A+1}_{Z}X$ is unstable, then it go through by β^{-}

$$ {}^{A+1}_{Z}X \rightarrow {}^{A+1}_{Z+1} X + e^{-} + \nu \tag{1.9} $$

1.3.1 s-process

s-process is the process of adding neutrons to nuclei one at a time (only stable elements can be made). It is a process of neutron capture with emission of γ ray (also known as (n,γ) reaction). It takes long time (about 100 years to 10^5years [6]) for each neutron capture. Neutron addition process or

neutron capture is so slow that it allows β decay to occur between steps. It occurs only in neutron dense environments, such as large stars collapsing before death. It is responsible for creating about half of the abundances of elements heavier than iron (Fe) in the galaxy. It operates in conditions characterised by low neutron densities (typically about 10^8 neutrons per cubic cm). It produces abundance peaks at A=90, 138 and 208 [6].

$$ {}^{A}_{Z}X + n \rightarrow {}^{A+1}_{Z} X + Energy(slow) \tag{1.10} $$

$$ {}^{62}Ni + n \rightarrow {}^{63} Ni + \gamma \tag{1.11} $$

$$ {}^{63}Ni \rightarrow {}^{63} Cu + \beta^- + \nu \tag{1.12} $$

$$ {}^{63}Ni + n \rightarrow {}^{64} Cu + \gamma \tag{1.13} $$

$$ {}^{64}Cu \rightarrow {}^{64} Zn + \beta^- + \nu \tag{1.14} $$

Neutron source in s-process: There are two important neutron sources during He burning in Asymptotic Giant Branch (AGB) stars: (1)^{13}C(α,n)^{16}O and (2)^{22}Ne(α,n)^{25}Mg

1.3.2 r-process

r-process is the process of neutron capture on a very short time-scale (about 0.01-10 sec). In r-process, neutron captures occur at a rapid rate or very fast compared to the β decays. It does not allow β decay to occur. It occurs only during high neutron flux events such as supernova. It is responsible for formation about half of the elements beyond ^{56}Fe. It is responsible for production of large number of isotopes mass number between $70 \leq A \leq 209$. It produces the abundance peaks at A=80, 130 and 194 [6].

$$ {}^{A}_{Z}X + {}^{1} n \rightarrow {}^{A+1}_{Z} X + Energy(fast) \tag{1.15} $$

$$ {}^{65}Cu + 5n \rightarrow {}^{70} Zn + \beta^- + \nu \tag{1.16} $$

It occurs only in core-collapse supernova. Fe-core is collapsed with co-existence of heavy nuclei associated with α, β, n, e$^-$ and ν particles. The electron capture reaction give the source of neutrons.

$$ p + e^- \rightarrow n + \nu \tag{1.17} $$

The Eq. 1.17 is the reaction which leads to neutron rich matter. The r-process in general can be written as

$$ {}^{A}_{Z}X + n \rightarrow {}^{A+1}_{Z} + n \rightarrow {}^{A+2}_{Z} + n \rightarrow ..... \tag{1.18} $$

1.4 Neutron Capture Reaction on Gadolinium

The thermal neutron capture reaction on gadolinium (Gd) or Gd(n,γ) reaction is expected to produce few γ-rays, which have the total energy of about 8 MeV. Reactions with ^{155}Gd and ^{157}Gd are described as follows:

$$n + {}^{155}Gd \rightarrow [{}^{156}Gd^{*}] \rightarrow {}^{156}Gd + \gamma,\ [8.5\ MeV] \tag{1.19}$$

$$n + {}^{157}Gd \rightarrow [{}^{158}Gd^{*}] \rightarrow {}^{158}Gd + \gamma,\ [7.9\ MeV] \tag{1.20}$$

Gd is one of the few nuclei which has resonance in the thermal energy region for the neutron capture reaction. The resonance energy is 26.8 meV for ^{155}Gd and 31.4 meV for ^{157}Gd [7]. Gd has the largest thermal neutron cross section, among all the stable nuclides. The thermal neutron capture cross-section for ^{155}Gd is 60900 barn and for ^{157}Gd is 254000 barn [7]. The ground state spin-parity of ^{155}Gd and ^{157}Gd is $\frac{3}{2}^{-}$. Capturing an s-wave neutron leads to $J^{\pi}=1^{-}$ and $J^{\pi}=2^{-}$ resonance in ^{156}Gd and ^{158}Gd. The more details of ^{155,157}Gd are given in Table 1.3.

TABLE 1.3: Basic atomic properties of ^{155,157}Gd

Isotope	Mass number	Atomic mass (a.m.u)	Atomic number	S_n (MeV)	I^{π}	Magnetic moment, μ_N
^{155}Gd	155	154.9226	64	8.538	$\frac{3}{2}^{-}$	-0.2591
^{157}Gd	157	156.92396	64	7.937	$\frac{3}{2}^{-}$	-0.3399

In natural gadolinium the abundances of ^{155}Gd and ^{157}Gd are 14.80% and 15.65% respectively. The ratio of cross-section of ^{155}Gd/^{157}Gd is about 1/4. Table 1.4 shows the natural abundances of Gd and their thermal neutron capture cross-section.

TABLE 1.4: Isotopic abundance and thermal cross-section of Gd

Isotope	Isotopic abundance and thermal cross-section of Gd						
	^{152}Gd	^{154}Gd	^{155}Gd	^{156}Gd	^{157}Gd	^{158}Gd	^{160}Gd
Natural Abundance	0.2%	2.18%	14.8%	20.5%	15.7%	24.8%	21.9%
Thermal cross-section	735 barn	85 barn	60900 barn	1.8 barn	254000 barn	2.2 barn	1.4 barn

Table 1.5 shows that some thermal neutron capture reactions and their thermal neutron capture cross-sections.

TABLE 1.5: List of cross-sections of the typical neutron reactions

Reaction	Cross-section (barn)	Resonance energy E_0 (meV)
$n + p \rightarrow d + \gamma(2.2MeV)$	0.3326	
$n + {}^{3}He \rightarrow p + {}^{3}H$	5333	
$n + {}^{6}Li \rightarrow \alpha + {}^{3}He$	940	
$n + {}^{10}B \rightarrow \alpha + {}^{7}Li$	3837	
$n + {}^{113}Cd \rightarrow {}^{114}Cd^{*} \rightarrow {}^{114}Cd + \gamma$	20,615	178
$n + {}^{149}Sm \rightarrow {}^{150}Sm^{*} \rightarrow {}^{150}Sm + \gamma$	40,140	97.3
$n + {}^{155}Gd \rightarrow {}^{156}Gd^{*} \rightarrow {}^{156}Gd + \gamma$	60,900	26.8
$n + {}^{157}Gd \rightarrow {}^{158}Gd^{*} \rightarrow {}^{158}Gd + \gamma$	2,54,000	31.4
$n + {}^{161}Eu \rightarrow {}^{162}Eu^{*} \rightarrow {}^{162}Eu + \gamma$	9,200	321
$n + {}^{235}U \rightarrow$ A+B (Fission)	583	

A list of thermal neutron cross-section of ^{155,157}Gd from other experiments are given in Table 1.6 [8] .

TABLE 1.6: Thermal neutron capture cross-section of Gd [8]

Data Set	Thermal neutron capture cross-section $\sigma_{0\gamma}$ (barn)		
	^{152}Gd	^{157}Gd	Notes
Lapp et. al	$\sigma_\gamma(^{157}Gd)/\sigma_\gamma(^{155}Gd) \approx 3.5$	$\sigma_\gamma(^{157}Gd)/\sigma_\gamma(^{155}Gd) \approx 3.5$	Pile neutron, mass spectroscopy
Pattenden	66000 (2000)	264000 (4500)	Transmission
Tattersall et. al	49800 (2000)	213000 (2000)	Pile Oscillator
Moller et. al	60699 (500)	254000 (2000)	Resonance measurement
Groshev et. al	61000 (5000)	240000 (12000)	(n,γ)
Sun et.al	59100 (4600)	232000 (14000)	Prompt γ measurement
Leinweber et. al	60200	226000	Resonance measurement
Mughabghab	60900 (500)	254000 (815)	Evaluation

1.4.1 Resonances of Gd

Gd is one of the rare earth elements and is a metal with atomic number 64, and it has seven naturally stable isotopes. Among them, two isotpes (^{155}Gd and ^{157}Gd) have large thermal neutron capture cross section. In this section, the reaction cross section is concretely described taking these two kinds of Gd isotopes as examples. Table 1.7 shows the resonance parameters of ^{155}Gd and ^{157}Gd obtained from the JENDL [9] database and [7, 10]. Since focusing on low energy neutrons this time, only the resonance in the range of 1 meV to 10 eV is shown in the table. For neutron energy in between 1 meV and 10 eV, ^{155}Gd has seven resonances and ^{157}Gd has 2 resonances.

TABLE 1.7: Resonance parameters of 1 meV to 10 eV region of ^{155}Gd and ^{157}Gd

Gd isotope	E_r(eV)	J$^\pi$	Γ_n(eV)	Γ_γ (eV)
^{155}Gd	0.02515	2^-	9.70×10^{-5}	1.04×10^{-1}
^{155}Gd	2.0120	2^-	4.00×10^{-5}	1.28×10^{-1}
^{155}Gd	2.5729	2^-	1.71×10^{-5}	1.07×10^{-1}
^{155}Gd	3.6160	1^-	5.00×10^{-5}	1.30×10^{-1}
^{155}Gd	6.3057	2^-	2.20×10^{-5}	1.09×10^{-1}
^{155}Gd	7.7477	2^-	1.16×10^{-5}	1.09×10^{-1}
^{155}Gd	9.9910	2^-	2.0×10^{-5}	1.10×10^{-1}
^{157}Gd	0.03200	2^-	4.28×10^{-5}	1.07×10^{-1}
^{157}Gd	2.8287	2^-	3.77×10^{-5}	1.10×10^{-1}

Among them, the lowest energy resonance energy is 25 meV and 32 meV, respectively, which is just the thermal neutron energy region. This shows that Gd has a high cross-sectional area with respect to thermal neutrons. By using this parameter, the cross sectional area can be concretely obtained from the Breit - Wigner formula.

Find the nucleus radius for the connection condition at the potential surface. The relation between the nucleus radius R and the mass number A, generally,

$$R = 1.2A^{1/3}\ [fm] \tag{1.21}$$

The radius for ^{155}Gd is R$\simeq$6.44 fm and for ^{157}Gd is R$\simeq$6.47.

1.4.2 Resonant Scattering

The elastic scattering cross section can be obtained by using the Eq. 2.100 for ^{155,157}Gd using the parameters from Table 1.7 and the values of the nucleus radius. Figure 1.6 shows the elastic scattering cross-section for ^{155,157}Gd from the nuclear data center of JAEA [11]. If resonance does not occur, the scattering is found to be about the surface area of the nucleus $4\pi R^2$ =571 $[fm^2]$= 5.71 [barns]. On the other hand, the resonance energy has a peak, and the cross sectional area is three times or more larger.

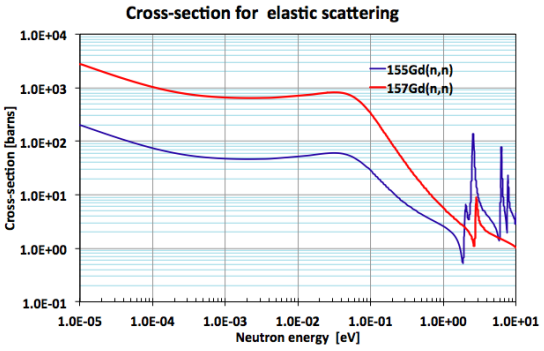

FIGURE 1.6: Elastic scattering for Gd

1.4.3 Capture Resonance

The capture cross section of ^{155,157}Gd can be obtained using Eq. 2.105. Figures 1.7 & 1.8 shows the both the elastic scattering cross section and capture cross-section together and total cross-section from the nuclear data center of JAEA [11]. In the thermal neutron region of 1 eV or less, the capture cross section is larger by about 3 orders of magnitude than the elastic scattering cross section. The capture cross-section are dominant in thermal region. Because of the interaction between Gd and thermal

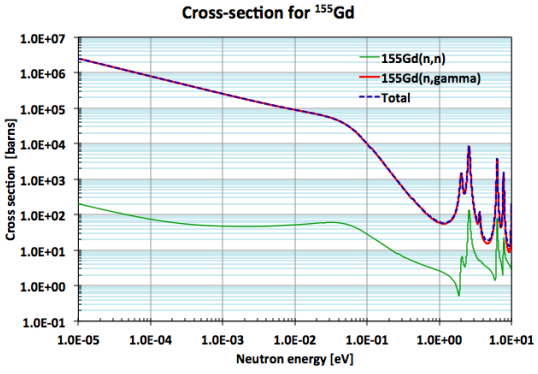

FIGURE 1.7: Cross-section for ^{155}Gd

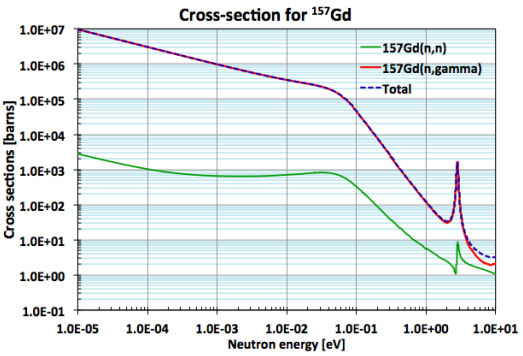

FIGURE 1.8: Cross-section for ^{157}Gd

neutrons, the trapping reaction is predominant and can be considered ignoring scattering. Likewise, thermal neutron capture cross sections can be obtained for seven isotopes.

The probability that one isotope reacts when a neutron capture reaction occurs can be obtained. The probability that ^{157}Gd reacts when natural Gd undergoes a thermal neutron reaction is about 80%,

and the probability of ^{155}Gd reacting is about 20%. That is, it is sufficient to investigate the reaction between ^{157}Gd and ^{155}Gd for the thermal neutron capture reaction of natural Gd. Figure 1.9 shows that the thermal neutron cross-section for all the stable nuclei [7].

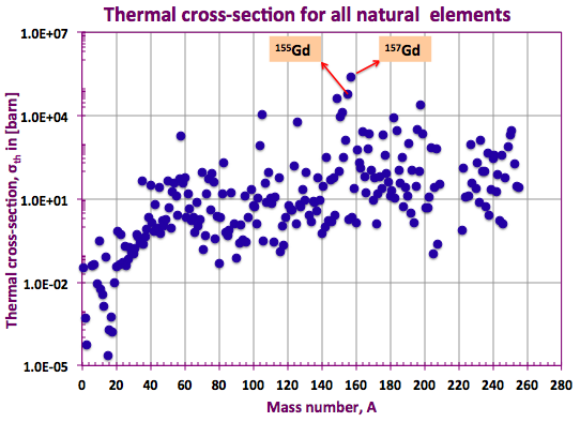

FIGURE 1.9: Thermal neutron capture cross-section for all elements [7]

1.4.4 Emission of γ Ray form Gd

When a neutron capture by ^{A}Gd nucleus, it forms a compound nucleus of $^{A+1}$Gd. This compound nucleus is in an excited state and releases γ rays when returning to the ground state. The total energy of γ rays to be emitted can be calculated using the mass difference between the ^{A}Gd and $^{A+1}$Gd, and the difference is called the Q value. For example, the sum of energies of γ rays E_γ emitted by neutron capture of ^{157}Gd as

$$n + {}^{157}Gd \rightarrow {}^{158}Gd^{*} \rightarrow {}^{158}Gd + \gamma \tag{1.22}$$

$$E_\gamma = (mass\ of\ {}^{157}Gd) + (mass\ of\ neutron) - (mass\ of\ {}^{158}Gd) \simeq 7.94\ MeV \tag{1.23}$$

Figure 1.10 shows the schematic diagram of capture reaction for ^{157}Gd(n,γ) and shows the resonance state of ^{158}Gd.

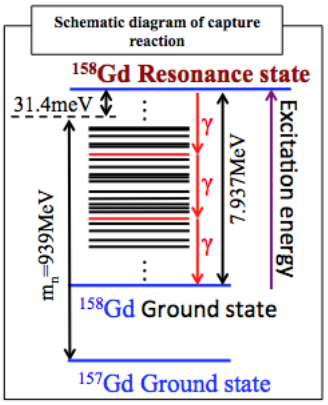

FIGURE 1.10: Resonance state of ^{158}Gd

The excited CN $^{A+1}$Gd* will go to its ground state by emitting γ rays. It emits γ rays in two different ways: (i) Discrete prompt γ rays (ii) Continuum spectrum.

(i) Discrete prompt γ rays: Discrete peaks are fixed transition between nuclear levels. It contribute about 4-6 $\%$ to the data.

(ii) Continuum spectrum: Continuum spectrum of continuum level stems from random transitions especially with the high Nuclear Level Density (NLD) domain. It contribute about 94-96$\%$ to the data.

Figure 1.11 show the discrete and continuum level of ^{158}Gd.

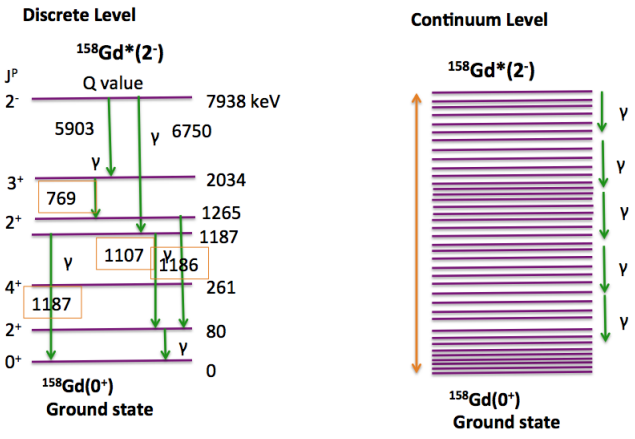

FIGURE 1.11: Discrete and continuum levels of ^{158}Gd

Similarly, for ^{155}Gd we can get

$$n + ^{155}Gd \rightarrow ^{156}Gd^* \rightarrow ^{156}Gd + \gamma \tag{1.24}$$

In this reaction, the sum of the energies of the released γ is

$$E_\gamma = (mass\ of\ ^{155}Gd) + (mass\ of\ neutron) - (mass\ of\ ^{156}Gd) \simeq 8.54\ MeV \tag{1.25}$$

Figure 1.12 shows the schematic diagram of capture reaction for ^{155}Gd(n,γ) and shows the resonance state of ^{156}Gd.

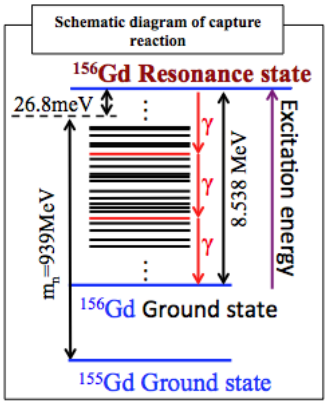

FIGURE 1.12: Resonance state of ^{156}Gd

Figure 1.13 show the discrete and continuum level of ^{156}Gd. The energy of each of the released γ rays

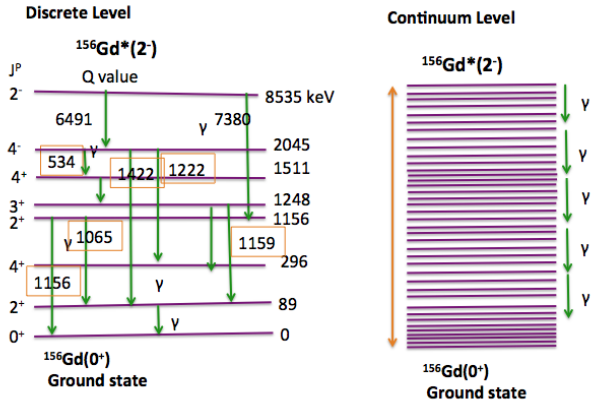

FIGURE 1.13: Discrete and continuum levels of ^{156}Gd

depend on which excitation level they collapse. For γ rays with particularly high intensity, their intensity ratios have been measured so far. Also, the number of γ rays released is already measured for neutron energy in the eV to keV region, but not in the thermal neutron region.

1.5 Application of Gd(n,γ) Reaction

The γ-ray spectrometry of the high-energy region (about 10 MeV) has wide range of application in nuclear engineering and nuclear science [12]. Because of having the largest thermal neutron cature cross-section, Gd has so many scientific, medical and industrial applications. Gd(n,γ) reaction is used for neutron tagging to identify elctron anti-electron neutrinos. Recently, Super Kamiokande (SK) has started to develope a Gd-loaded water Cherenkov detector "Sk-Gd" for detection of elctron anti-electron neutrinos $\overline{\nu_e}$ [13, 14]. Gd can also be used in reactor neutrino monitroing. Gd is also used as a burnable poison in the fuel pin or moderator of the reactor core mainly in nuclear power plants with boiling water reactor (BWR) and Canada Deuterium Uranium (CANDU) reactor [15, 16]. It is of the very important nuclides in the safety consideration of reactor core criticality. Gd can also be used as a capture agent for Neuton Capture Therapy(NCT) [17, 18].

The n-capture Gd or Gd(n, γ) reaction is important for :
(1) Neutrino detection technology
(2) Reactor neutrino monitoring
(3) Neutron poisons in a nuclear reactor
(4) Neutron capture therapy in nuclear medicine

1.5.1 Neutrino Detection Technology

1.5.1.1 Neutrino

Neutrinos are electrically-neutral leptons with half integer spin which only undergo weak interactions. They are one of the fundamental particles which are responsible for creating the universe. They are found in three different flavors, electron (ν_e), muon (ν_μ) and tau (ν_τ), analogous to the charged leptons.

Neutrino sources :

There are two types of neutrino sources (1) Natural sources and (2) Artificial sources.
(1) **Natural Sources:** (i) Atmospheric neutrinos, (ii) Solar neutrinos , (iii) Supernova neutrinos, (iv) High energy neutrino sources , (v) Cosmic neutrino background or Big bang relic neutrinos , (vi) Neutrinos from center of the earth
(2) **Artificial Sources:** (i) Accelerator neutrinos , (ii) Reactor neutrinos

1.5.1.2 Neutrino Detection

Neutrinos have an extremely small interactions probability with matter. So, it is very difficult to detect neutrinos directly. One can detect only the existence of neutrinos if they interact. There are two main ways by which a neutrino can interact with matter:
(i) Charged-current interactions: In this type of interaction, the neutrinos are converted into another equivalent charged particle (e.g inverse β decay).

$$\bar{\nu_e} + p \rightarrow e^+ + n \tag{1.26}$$

Here, a charged particle (lepton) can be detected to find the exiting of neutrino.
(ii) Neutral-current interactions: It is a kind of interaction by which neutrino can remain a neutrino, but only transfers energy and momentum to whatever it interacted with.(e.g neutrino-electron scattering or neutrino-deuteron interaction)

$$\nu_e + e \rightarrow \nu_e + e \tag{1.27}$$

and

$$^2H + \nu \rightarrow p + n + \nu \tag{1.28}$$

To find the existence of neutrino one needs to detect this energy transfer either because the target recoils or because target breaks up.

The neutrinos were observed for the first time by Fred Reines and Clyde Cowan with the help of charged-current interaction in 1956, in the time of measuring anti-electron neutrinos ($\bar{\nu_e}$) via the inverse β-decay interaction in a water tank.

$$\bar{\nu_e} + p \rightarrow e^+ + n \tag{1.29}$$

The positron, e^+ annihilates with the electron and produces two γ-rays of energy 511 keV in the water, which were amplified by surrounding organic scintillator, and could be observed. A good neutron absorber, cadmium (Cd), was added to the water for enhancing the efficiency of neutron capture events. These neutron capture events would produce a further, delayed γ-ray signal. Observation of delayed signal in addition to the primary signal allowed background to be reduced greatly.

1.5.1.3 Super- Kamiokande

Super-Kamiokande is the largest underground neutrino detector in the world. It is a Cherenkov detector which is used to study neutrinos from different sources like the neutrinos from sun, supernovae, the atmosphere and the accelerator for proton detector. It is located in Kamioka mine in Gifu Prefecture of Japan. It consists of 50,000 tons of pure water in cylindrical tank of 41.4 meters tall and 39.3 meters in diameter. Figure 1.14 shows the schematic diagram Super-Kamiokande neutrino detector.

It has 11,129 photomultipliers (PMTs) [19] of 20-inch diameter in its inner detector and 1,885

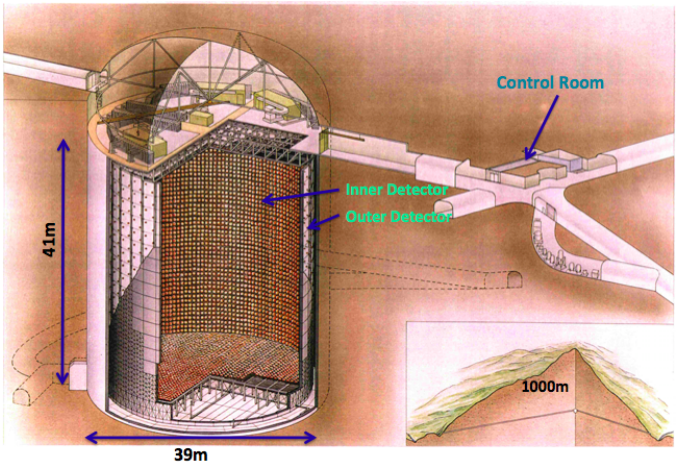

FIGURE 1.14: Schematic diagram of Super-Kamiokande detector [20]

PMTs of 8-inch-diameter in its outer detector. It has various purposes in neutrino physics and in the measurement of proton life time. It has been observing solar neutrinos [21], atmospheric neutrinos [22] as well as accelerator neutrinos [23] and has also found several evidences for neutrino oscillations.

1.5.1.4 SRN Search and SK-Gd Project

It is very important way to study supernova models by using neutrinos, because about 99% of the energy releases as neutrino flux from supernovae process. We know that supernova occurs two or three times within one century in our galaxy. Last time world observed supernova from SN1987A in 1987. Supernova has been occurring regularly in the 15 billion years history of the universe. The neutrinos from past supernovae are called Supernova Relic Neutrinos (SRN), or known by another name as Diffuse Supernova Neutrino Background (DSNB).

Both solar and reactor neutrinos are dominant at energy below 10 MeV. Atmospheric neutrinos

are dominant at energy above 30 MeV. SRN are dominant at energy in between 10 MeV to 30 MeV. The event rate of SRN is very small and which is expected to be about 1.3-6.7 events/year/22.5 kton in Super-Kamiokande. SRN has not been observed due to the high background and low event rate. Inverse beta decay (IBD) has played a significant role in detection of SRN because it has larger cross-section than the cross-section of electron neutrino ν_e elastic scattering with electron by a factor 2. The elastic scattering of electron neutrino ν_e with electron is the second most visible interaction of SRN in Super-Kamiokande. In IBD reaction, a anti-electron neutrino ($\bar{\nu_e}$) interacted with proton of the water and emit positron and a neutron, can be written as

$$\bar{\nu_e} + p \rightarrow e^+ + n \tag{1.30}$$

Currently, SK is getting two signals from IBD process (shown in Figure 1.15). Those signals

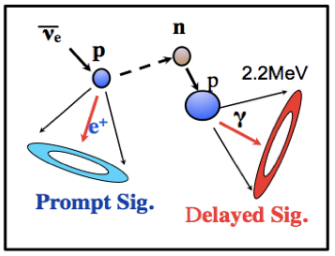

FIGURE 1.15: Anti-neutrino interaction with proton of water

are: (i) prompt signal comes form chrenkov light by positron motion in water and two 0.511 MeV γ rays from annihilation (ii) delayed signal comes (2.2 MeV γ rays from deuteron) from neutron capture by hydrogen of the water [19]. The coincidence detection of prompt and delayed signal can effectively reduce the background. The detection of 2.2 MeV of γ rays and the method of tagging neutrons by 2.2 MeV γ ray is very difficult due to their low efficiency. For increasing the neurton capture efficiency, a project was proposed of adding gadolinium into Super-K [13].

1.5.1.5 Neutron capture on gadolinium at SK

Common techniques (using IBD process in water) of neutrino detection with water may have lots of background. To reduce background, one needs:

(i) small time difference between prompt and delayed signal (need element of high thermal neutron capture cross-section).

(ii) released high energy.

Gd features both the conditions because it has largest thermal neutron capture cross-section among all stable nuclei and it releases γ of energy about 8 MeV.

Figure 1.16 shows the anti-electron neutrino detection using Gd loaded water. The prompt signal will get from the Chrenkov light by positron motion in water and two 0.511 MeV γ rays from annihilation and the delayed signal from the γ ray from the neutron capture on Gd. The background can be

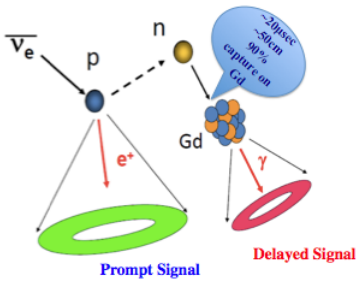

FIGURE 1.16: Anti-neutrino interaction with Gd mixed water

reduced by measuring coincidence detection of prompt and delayed signal.

The thermal neutron capture cross-section for natural gadolinium (cross-section is 49000 b) is much more larger than the cross-section of free proton (cross-section is 0.3 b) [19]. The thermal neutron capture on ^{155}Gd can emit about 8.5 MeV γ rays (thermal neutron capture cross-section is 60900 b and emit about 3-4 γ rays) and on ^{157}Gd can emit about 7.9 MeV γ rays (thermal neutron capture cross-section is 254000 b and emit about 3-4 γ rays). This high energy will make neutron tagging much more easier and more efficient than 2.2 MeV γ rays. In this process, there are two signal from IBD: (i) prompt signals comes from Cherenkov light by positron emission in water and two γ rays from annihilation (ii) the delayed signal come from neutron capture by Gd.

Coincidence detection of the prompt and delayed signal will reduce the background in neutrino detection. Recently, there are a lots of Research & Development (R&D) works are ongoing and the project of adding gadolinium into SK is known as SK-Gd project. The authority of SK are planning to start "SK-Gd" project in 2018. Evaluating Gadolinium's Action on Detector Systems (EGADS) is a research and development project for planning to enrich the water in the Super-Kamiokande (SK) detector with gadolinium (Gd) sulfate ($Gd_2(SO_4)_3$). EGADS was added $Gd_2(SO_4)_3$ into the 200 tons water in April 21st, 2015 is about 0.2% (about 90% neutron capture on Gd). Table 1.8 shows that the present and future neutrino experiments using Gd.

TABLE 1.8: Present and future neutrino experiments using Gd

Experiment	Detector	Measure
EGADS	Water Cherenkov	R and D for SK-Gd
SK-Gd (2018∼)	Water Cherenkov	SRN, SN ν, Solar ν, atm ν, p^+ decay
Daya Bay, RENO Double Chooz	Liquid scintillator	The mixing angle θ_{13}

1.5.2 Reactor neutrino monitoring

1.5.2.1 Neutrinos from nuclear reactor

Nuclear reactors, generally used for power generation, are sources of anti-electron neutrinos ($\bar{\nu_e}$) by β decay from fission product. Fission reactors are known to be the most intense source of anti-electron neutrino $\bar{\nu_e}$. They produce fission fragments in highly excited states with the help of β decays. There are about six neutrinos are emitted per fission on average. A 1-GW (Giga-Watt) thermal power reactor will emits total flux of 2×10^{20} [24] anti-electron neutrinos ($\bar{\nu_e}$) per second, as about 200 MeV energy is released for each fission reaction.

Figure 1.17 shows that the comparison of the neutrino flux of ^{235}U, ^{238}U, ^{239}Pu and ^{241}Pu

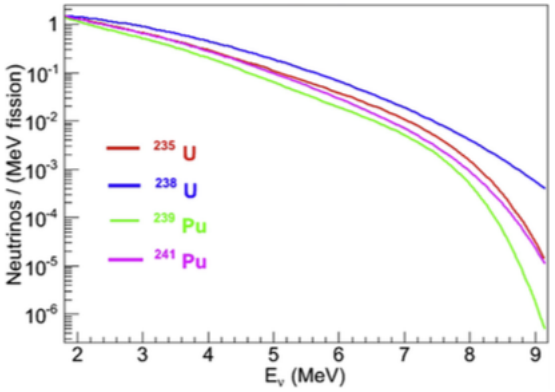

FIGURE 1.17: Number of neutrinos for each isotope in the nuclear reactor [24]

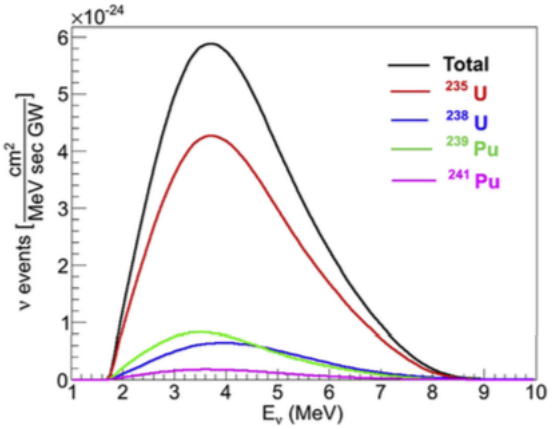

FIGURE 1.18: Number of events of the IBD of reactor neutrinos for each isotope [24]

normalized per fission [24] (which is the result from Huber+Mueller model). Figure 1.18 shows that the comparison between the number of neutrino absorption events with different target as a function of energy [24] This neutrino absorption events calculation is done for a 1-GW reactor for every isotope having the initial isotopic configuation for 4% enriched fuel.

1.5.2.2 Detection of neutrinos for reactor monitoring

C. L. Cowan and his group [25] detected the reactor neutrinos for the first time using IBD reaction as $\bar{\nu_e}$+p$\rightarrow$e$^+$+n. In the beginning of 1980s, scientist tried to use neutrinos for reactor monitoring and developed an optimized detector for reactor safeguard. There are two different types of detector by which we can detect rector neutrinos for reactor neutrino monitoring: (1) Reactor neutrino monitoring with liquid scintillator (2) Reactor neutrino monitoring with plastic scintillator

(1) Reactor neutrino monitoring with liquid scintillator:

Basically, hydrogen or carbon atom are used as the material of the liquid scintillator (LS). The ratio of hydrogen and carbon atoms inside the LS is in between 1:1 and 2:1. The threshold energy for

IBD is about 1.8 MeV. So, the neutrinos which have energy less than 1.8 MeV energy, have never be detected in IBD method. In IBD process, positron and neutron are produced. The prompt signal can be found from annihilation of positron with electron of the liquid by producing two γ rays of energy 511 keV. The delayed signal can be found by the γ ray emitted from the neutron capture by the proton (hydrogen) of the liquid. It is about 180μs need to capture the neutron by the proton of the liquid. And the Q value of neutron capture proton reaction (n+p$\rightarrow$d+γ) is 2.225 MeV, that is why this process will emit 2.2 MeV prompt γ rays. The combination of prompt and delayed signal helps to minimise the background events. For subtracting background accurately, we need the neutron capture time shorter. To make neutron capture quickly, we need to add Gd (which has largest thermal neutron capture cross-section) into the central liquid scintillator. This is known as gadolinium-loaded liquid scintrillator (Gd-LS). This Gd loaded liquid scintillator is also known as target. It will reduce the neutron capture time 180μs to 30μS. Then the neutron capture by Gd can be happen as n+^{155,157}Gd$\rightarrow$ ^{156,158}Gd+γ. It will emit γ rays of about 8 MeV.

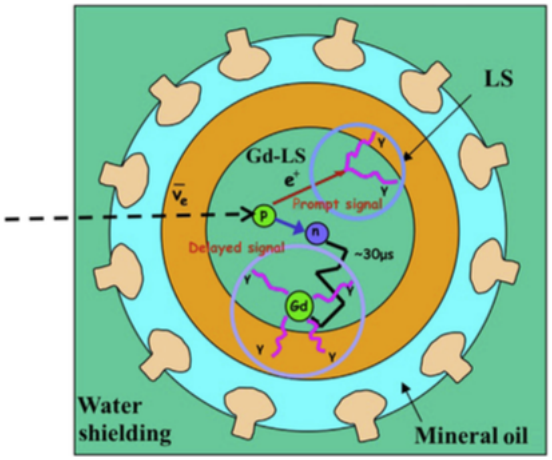

FIGURE 1.19: Schematic layout of antineutrino detector of gadolinium loaded liquid scintillator [24]

Figure 1.19 shows that the schematic diagram of anti-neutrino detector concept [24]. In the figure, Gd-LS is the liquid scintillator with Gd doped and LS is the liquid scintillator without Gd doped known as gamma catcher. There is layer of mineral oil which is used a nonscintillating light transparent material. The size of the LS should be 60 cm for measuring γ rays which is produced inside the Gd-LS. The neutrino goes inside the Gd-LS and produce neutron and positron with the help of IBD process. The positron signal produces two γ ray of 511 keV energy by annihilation with the electron inside the liquid scintillator. The target volume is covered by anther layer of liquid scintillator without Gd LS to prevent the leakage of 511 keV from the target LS and which is called as gamma catcher.

(2) Reactor neutrino monitoring with plastic scintillator:

Anti-neutrino is very important tool for reactor monitoring. The well known project for anti-neutrino detection for rector monitoring is PANDA. Where PANDA stands for Plastic Anti-neutrino Detector Array.

Figure 1.20 shows that the schematic view of anti-neutrino detector or PANDA detector. The

FIGURE 1.20: Schematic view of antineutrino detector (PANDA detector) [26]

PANDA detector has 36 identical modules. This modules are PANDA modules. Figures 1.21 and 1.22 show the schematic diagram of PANDA module. One module has about 10 kg of plastic scintillator in it. Two acrylic cubic light guides with sizes 10cm×10cm×100cm are added to both ends of the plastic scitillator. Two PMTs are added to the light guides. Both the plastic scintillator and light guides are covered by aluminized mylar and Gd_20_3 coated polyester sheet. This polyester sheets contains about 4.9 mg/cm^2 of Gd.

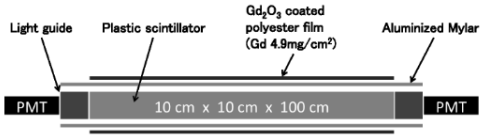

FIGURE 1.21: Schematic diagram of PANDA module [26]

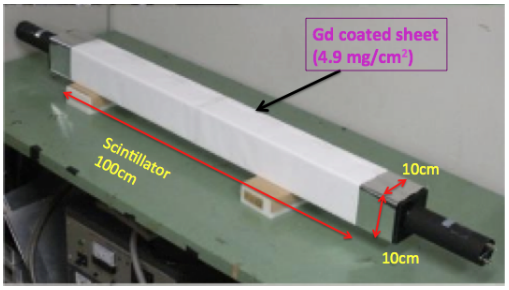

FIGURE 1.22: Schematic diagram of PANDA module [27]

The anti-neutrinos can be detected by the IBD interaction on proton in the Plastice scintillator having energy threshold of 1.8 MeV.

$$\bar{\nu_e} + p \rightarrow e^+ + n \tag{1.31}$$

The neutron and positron created from IBD can be detected separately. Positron produces prompt events by annihilation with the electron as

$$e^+ + e^- \rightarrow 2\gamma \tag{1.32}$$

The neutron is captured by the Gd which embedded in between plastics scintillators and produced γ rays with total energy about 8 MeV as

$$n + {}^{155}Gd \rightarrow {}^{156}Gd^* \rightarrow {}^{156}Gd + \gamma's \tag{1.33}$$

$$n + {}^{157}Gd \rightarrow {}^{158}Gd^* \rightarrow {}^{158}Gd + \gamma's \tag{1.34}$$

which is known as delayed events. Figure 1.23 shows the prinple of anti-neutrino detection method in PANDA module. By using delayed coincidence method we can detected the prompt and delayed events.

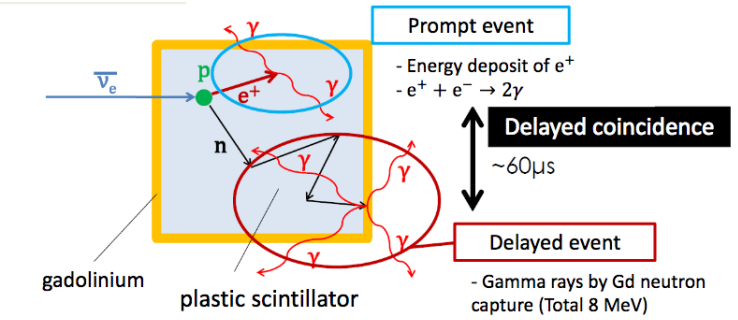

FIGURE 1.23: Priciple of anti-neutrino detection in PANDA module [27]

1.5.3 Neutron Poison in a Nuclear Reactor

An element with a large thermal neutron capture (or absorption) cross-section, uses in a nuclear reactor to diminish the high reactivity of their fresh fuel is known as neutron poison or neutron absorber. Neutron poisons are inserted into the reactor core intentionally. There are different types of poisons. Those are

(1) Control poisons, (2) Burnable poisons, (3) Non-burnable poison, (4) Soluble poisons

Mostly, Gd is widely used as a burnable absorber or burnable poison [15, 16] in the fuel pin or moderator in the reactor core like boiling water reactor (BWR) and Canada Deuterium Uranium (CANDU) reactor.

1.5.3.1 Burnable poison

Burnable poisons are inserted intentionally inside the nuclear reactor core to control the high reactivity of fuel without control rod. They have a high thermal neutron capture or absorption cross-section and they are converted into other materials with relatively low thermal neutron capture cross-section by capturing neutron. They are used mainly to compensate for high reactivity in following ways: (i) in the initial core when all fuel are seemed to be fresh and (ii) during and following the reactor shut down when the concentration of ^{135}Xe is delayed below normal levels. Boron(B) can be used in the initial core and gadolinium(Gd) can be used following reactor shut down. Gd can also be used as burnable poison in Pressurized Heavy Water Reactors (PHWR) in both cases as (i) at 15 ppm concentration in the time of emergency shut down and (ii) at 2 ppm during the start up of reactor [28]. Figure 1.24 shows the typical CANDU reactor and Figure 1.25 shows the special shut down system for CANDU reactor. Advantage of using Gd is that burnout rate compensates for ^{135}Xe growth.

Gd is mostly used as a neutron absorber in nuclear indutries like nuclear reactor because of its high thermal neutron capture (or absorption) cross-section (two isotopes ^{155}Gd and ^{157}Gd has largest cross-section in thermal neutron). It is widely used as a burnable absorber [15, 16]. It is very effective in compensation of the excess of reactivity, but any kind of inhomogeneous distribution of it may change the neutron-flux density in the core. Currently, Pressurised Water Reactor (PWRs) and Boiling Water Reactor (BWRs) are using the burnable neutron poisons extensively in various forms as Fuel assemblies

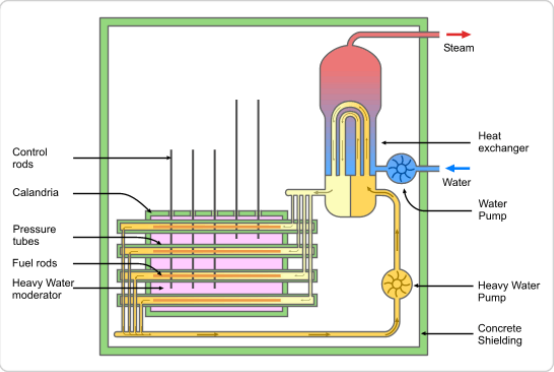

FIGURE 1.24: Schematic diagram of CANDU reactor [29]

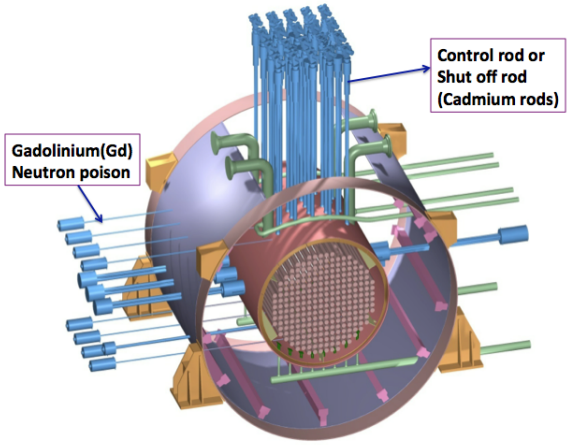

FIGURE 1.25: CANDU reactor special shutdown systems[30]

(FAs). Element which has larger thermal neutron capture cross-section than one of the neutron - induced fission of ^{235}U, can be used as a burnable poison. Burnable poison have been tested in different forms over last few decades. The most commonly used one is gadolina (Gd_2O_3) mixed within the nuclear fuel UO_2 [31].

1.5.4 Neutron Capture Therapy for Cancer

A kind of noninvasive therapy which is used for the treatment of locally fast-growing malignant tumors (like primary tumors and recurrent head and neck cancer) is known as neutron capture therapy (NCT). NCT is a suitable method for the treatment of intractable tumor such as brain tumors [32]. Currently, the non-radioactive element ^{10}B is using as a capture agent of NCT for all the clinical experience and which is known well as born neutron capture therapy (BNCT) [33]. NCT performs in two process: (i) first we need to inject the capture agent ^{10}B into the tumor cell and (ii) then the patient need to be radiated with thermal neutrons. Figures 1.26 and 1.27 show the schematic diagram of BNCT for a tumor. The neutrons are captured by the ^{10}B and formed ^{11}B. Then the excited ^{11}B splits by producing two low energy ions (^{4}He^{2+} (α-particle) and ^{7}Li^{3+}). These low energy charge particles can selectively kill the tumor cells.

$$^{10}B + n_{th} \rightarrow [^{11}B]^* \rightarrow^4 He^{2+} +^7 Li^{3+},\ [2.31MeV] \tag{1.35}$$

The chance of happening this reaction is about 94% and remaining 6% will decay in following equation

$$^{10}B + n_{th} \rightarrow [^{11}B]^* \rightarrow^4 He^{2+} +^7 Li^{3+},\ [2.79MeV] \tag{1.36}$$

Gd (mainly ^{157}Gd) is another promising element which can also be used as a capture agent for NCT [18]. The possible interest for using ^{157}Gd as a capture agent in NCT are due to the following reasons: (i) it has very high thermal neutron capture cross section among all stable nuclei. (ii) it containing compounds that target tumors are being developed as MRI contrast agent. (iii) neutron capture on ^{157}Gd

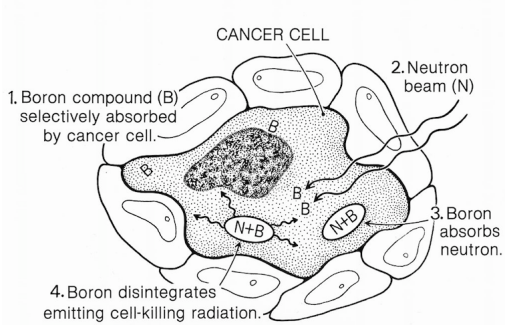

FIGURE 1.26: Schematic diagram of BNCT [34]

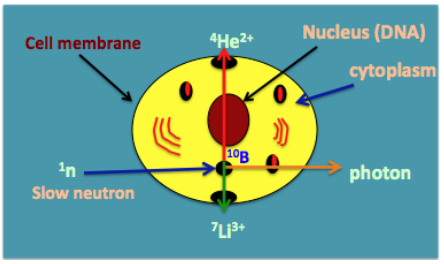

FIGURE 1.27: BNCT cell killing Mechanism

i.e, ^{157}Gd (n,γ) emits γ rays and internal conversion and Auger electrons .

$$^{157}Gd + n_{th}(0.025eV) \rightarrow [^{158}Gd]^{*} \rightarrow ^{158}Gd + \gamma \tag{1.37}$$

$$^{157}Gd + n_{th}(0.025eV) \rightarrow [^{158}Gd]^{*} \rightarrow ^{158}Gd + internal\ converion\ electron \tag{1.38}$$

These internal conversion electron can produce auger electrons and characteristic X-rays as

$$internal\ converistion\ electron \rightarrow Auger\ electrons + characteristic\ X-rays \tag{1.39}$$

γ rays, internal conversion electrons, characteristic X-rays and auger electron have 99.2%, 0.592%, 0.153% and 0.041% of total reaction energy respectively.

Many studies are going on using Gd as a capture agent in neutron therapy for cancer treatment or tumor treatment [17, 18]. Gadolinium neutron capture therapy (GdNCT) is a potential treatment for malignant tumors. GdNCT works in two different steps (i) injection of a specific element ^{157}Gd inside the tumor (ii) then tumor need to be radiated with thermal neutron [18]. Internal conversion electrons and auger electrons are responsible for killing tumor cells. The advantages of using ^{157}Gd over ^{10}B is that it has larger thermal neutron capture cross-section among all the stable nuclei and it containing compounds that target tumors are being developed as MRI contrast agent.

Before GdNCT is applicable, the following problems must be solved: neighbouring cells or tissues of tumor will receive cross-fire dose prompt gamma rays and also received absorbed dose from gamma rays.

1.5.5 Previous Experiment for Gd(n,γ) Reaction

Gd(n,γ) reaction is very important for nuclear and medical industry so that this reaction was performed by several groups in the world to find precise information. There are several publications on measured γ-ray spectra from Gd(n,γ) reactions for neutron beam energies in 1eV, keV and MeV region [35–37]. Recently, Detector for Advanced Neutron Capture Experiments (DANCE) at Los Alamos

National Laboratory's LANCE (LANCE) has extensively studied the γ-ray energy spectra from the radiative neutron capture reaction at various multiplicities in the neutron kinetice energy range from 1 to 200 eV for ^{152,154,156,158}Gd targets [38–40]. And the LiBerACE HPGe detector measure neutron capture ^{153,155,157}Gd(n,γ) cross-sections for neutrons energy up to 3 MeV [41] by using surrogate reaction technique with proton beam. Neutron capture has also performed at the Rensselaer Institute using liquid Gd samples (enriched either ^{155}Gd or ^{157}Gd) [10]. Table 1.9 shows that the list of some experiment of Gd(n,γ) reaction in all over the world.

TABLE 1.9: Some detector for Gd(n,γ) reaction

Detector	Center
DANCE (Array consists of 160 BaF_2)	LANCE, USA
Prompt γ activation analysis facility	Budapast Research Reactor
Capture detector 20l of NaI(Tl)	Rensselaer Polytechnic Institute (RPI) Linac facility
LiBerACE HPGe detectors	Lawrence Berkeley National Laboratory

1.5.5.1 DANCE Detector

DANCE stands for Detector for Advanced Neutron Capture Experiments. It is an array of detectors designed to measure prompt γ rays following neutron capture reaction. It is a segmented 4π γ rays calorimeter for measuring (n,γ) and (n, fission) cross-section of stable and long-lived radioactive samples. It is located at the Los Alamos National Laboratory's LANCE (Los Alamos Neutron Science Center) facility. It is an array of BaF_2 which consists of 160 BaF_2 crystals of four different shapes arranged in a 4π geometry [40, 42]. Volume of every crystal is 734 cm^3 volume and length of the each crystal is 15cm. The important part of this detector is that it measures the total reaction energy due to its nearly 4π geometry. The system can distinguish γ rays from α particles based on the signal waveform from the BaF_2 crystals.

The cross-section of ^{155}Gd(n,γ) reaction were measured with DANCE calorimeter at LANCE using the time of flight method for neutron energies 1.36-185 eV [40]. It has extensively studied the γ-ray energy spectra from the radiative neutron capture reaction at various multiplicities in the neutron kinetice energy range from 1 to 200eV for ^{152,154,156,158}Gd targets [38–40].

1.5.5.2 Budapest Research Reactor

The Budapest research reactor (BRR) is a research reactor. It is situated at Budapest in Hungary. It is one of the topmost research infrastructure in Hungary and also in central Europe. The general scientific activity at BRR is done by using of neutron beam lines for neutron scattering investigations. BRR is a reactor of water cooled and water-moderated reactor and it is designed and built by soviet. Initially, the power of the reactor was 2MW but the power was upgraded upto 5 MW in 1967 and upto 10 MW

in 1993. BRR is tank type reactor, moderated and cooled by light water and where the partial γ-ray production cross-sections of Gd from thermal neutron capture reaction were measured using neutron beam with beam power 10 MW at BBR.

Choi et al have determined the ^{155,157}Gd capture cross-sections using a precise method of measuring the partial γ-ray production cross-section using cold neutron beam at the BRR [8].

1.5.5.3 Rensselaer Polytechnic Institute

Rensselaer Polytechnic Institute (RPI), is a private research institute, was built in 1824. It is located in New York, USA. The RPI LINAC is a 60 MeV electron acceleartor. Neutron capture experiements were performed at the RPI linac facility using metalic and liquid Gd samples by using the time-of-flight (TOF) method [10]. Here liquid sample were isotropically enriched in either ^{155}Gd or ^{157}Gd. The capture measurements were made at the 25m flight station with a multiplicity type capture detector [10]. They proposed twenty eight new resonances and reviewed other previously identified resonances. Here they determined the neutron energy for a detected event using TOF method.

1.5.5.4 LiBerACE HPGe Detector

LiBerACE stands for Livermore-Berkeley Array for Collaborative Experiments. It consist of five clover-type high purity germanium (HPGe) detectors with bismuth-germanate-oxide(BGO) Compton-suppression shields. Beam is bombarded from 88-Inch Cyclotron at the Lawrence Berkeley National Laboratory (LBNL). LBNL is known as Berkeley lab. It is located in the Berkeley Hills near Berkeley, California, USA. The scattered photon were detected using the Silicon Telescope Array for reaction Studies (STARS). Here they uses surrogate nuclear reaction technique for neutron capture on targets (^{153,155,157}Gd). Inelastic proton scattering experiments were carried out on ^{154,156,158}Gd nuclei, which, in principle, can be used to measure ^{153,155,157}Gd(n,γ) cross-sections for neutrons energy up to 3 MeV [41].

1.6 Our Contributions

In this thesis, we studied the thermal neutron capture experiments on enriched gadolinium (^{155}Gd, ^{157}Gd isotopes). The experiment was performed using the Accurate Neutron -Nucleus Reaction Measurement Instrument (ANNRI) Germanium spectrometer at Materials and Life Science Experimental Facility (MLF) of the Japan Proton Accelerator Research Complex (JPARC), which provides the most intense pulsed neutron beam for neutron time-of-flight experiments in the world. The purposes of our experiments and analysis are to provide precise γ-ray spectrum of ^{155,157}Gd(n,γ) reactions and provide precise Gd decay model to neutrino physics field and other related fields. We studied the γ rays spectrum produced from thermal neutron capture on gadolinium isotopes (^{155}Gd, ^{157}Gd). We analysed only the

relatively intense and isolated (discrete) γ-ray peaks from the ^{155}Gd(n,γ) and ^{157}Gd(n,γ) reactions .We estimated the photo-peak efficiency using the calibration sources (^{60}Co,^{137}Cs and ^{152}Eu) and prompt γ rays from ^{35}Cl(n,γ) reaction and MC(Geant4) simulation. The purpose of the present work is to study the following:

(1) to measure the discrete γ rays from ^{152}Eu source and ^{35}Cl(n,γ), ^{157}Gd(n,γ) and ^{155}Gd(n,γ) reactions.

(2) to measure absolute photo-peak efficiency form ^{60}Co, ^{137}Cs, ^{152}Eu sources.

(3) to measure absolute photo-peak efficiency for MC(Geant4)

(4) to measure relative photo-peak efficiency from the prompt γ rays of ^{35}Cl(n,γ) reaction

(5) to measure the energy resolution of each Ge detector.

(6) to measure the position dependencies on count rate using ^{22}Na source and hence measure the target position

(7) to measure the relative intensities of discrete γ-rays from ^{152}Eu source and ^{35}Cl(n,γ), ^{157}Gd(n,γ) and ^{155}Gd(n,γ) reactions.

The absolute photo-peak efficiencies were measured from ^{60}Co, ^{137}Cs and ^{152}Eu sources and the relative efficiencies were measured from the prompt γ rays from ^{35}Cl(n,γ) reaction. The photo-peak efficiencies were calibrated from 0.1 to 9 MeV using the standard source ^{60}Co , ^{137}Cs and ^{152}Eu and the prompt γ rays from ^{35}Cl(n,γ) reaction with Monte Carlo (MC) simulation.

The relative intensities of discrete γ rays from ^{152}Eu source; ^{35}Cl(n,γ) and ^{157}Gd(n,γ) reactions were measured and compared with the values published by NNDC (CapGam)[43, 44]. The relative intensity of discrete γ-rays from the ^{155}Gd(n,γ) reaction has been measured for the first time. The main purposes of this experiment and analysis are to provide precise information of the Gd(n,γ) reaction to generate the MC simulation for neutrino detection, neutron poison, neutron therapy and all other industries where this reaction is used. As we used most intense neutron beam in the world for our experiment and used Ge -detector of very high resolution for measurement of γ-rays, so the accuracy of our result should be higher than other experiment.

1.7 Thesis Overview

In chapter 2, basic physics of scattering theory has been explained, including brief introduction of neutrons interaction with nucleus, Optical model, Compound Nucleus formalism and capture cross-section

In chapter 3, the details of basic semiconductor detector has been explained including the types and properties of the semiconductor, configuration of Ge-detector, γ-ray spectroscopy with Ge-detector and Interactions of γ radiation with detector crystal.

In chapter 4, the study of the properties of the Ge detector has been explained including Ge-detector experiment with ^{60}Co and ^{137}Cs

In chapter 5, the details of JPARC , MLF and ANNRI have been explained including its different

facilities.

In chapter 6, we have explained the Experimental Techniques and Data Processing system in ANNRI. Here we also explained about the samples, measurement condition, detector calibration and dead-time correction.

In chapter 7, we have explained details of our analysis and results including measurement of efficiency. measurement of energy resolution, measurement of position dependency of target, generation of MC(Geant4) simulation and also compared Data and MC .

In chapter 8, the analysis of discrete peaks of γ-rays from the n-capture γ-ray spectrum has been explained in details and measurement of relative intensities of discrete γ-ray has been explained here.

In chapter 9, we have concluded this dissertation with the discussion of this thesis and conclusion with some future works.

Chapter 2

Neutron Scattering Formalism

2.1 Scattering Theory

2.1.1 Formulation of the Scattering Theory

A beam particle is needed to direct towards the target material in the scattering experiment. As it is not easy to know the exact form of the interaction between particles due to nuclear forces, so the scattering experiment is very important for deriving the information about the force acting between them. The potential energy can be used to represent the interaction between the projectile and the scatterer.

In quantum theory of scattering, we imagine an incident plane wave travelling in the z direction, which encounters a scattering potential, and it produces an spherical outgoing wave by encountering with that scattering potential. Then the total wave function can be written as the sum of the incident plane wave function and spherically scattered wave function (shown in Figure 2.1). Therefore, the complete wave function is given by

$$\psi = incident\ plane\ wave + scattered\ wave \tag{2.1}$$

where incident plane wave function is $\psi_Z = e^{ikz}$ and spherical scattered wave is $\psi_{scatter} = f(\theta, \phi)\frac{e^{ikr}}{r}$.

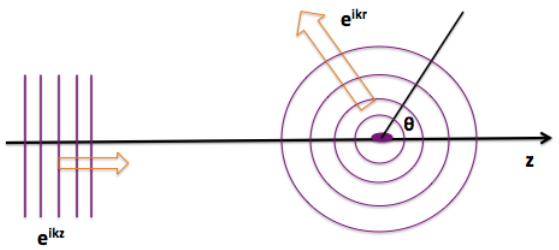

FIGURE 2.1: Scattering of waves; incoming plane wave generating outgoing spherical wave

$$\begin{aligned}\psi &= \psi_Z + \psi_{scatter} \\ &= e^{ikz} + f(\theta,\phi)\frac{e^{ikr}}{r}\end{aligned} \tag{2.2}$$

where k is the wave number and which is related to the energy of the incident particles in the usual way:

$$k \equiv \frac{\sqrt{2mE}}{\hbar} \tag{2.3}$$

The magnitude of the incident flux density along z-axis can be written as

$$v|\psi_Z|^2 = v|e^{ikz}|^2 \tag{2.4}$$

while the magnitude of scattered flux can be written as

$$v|\psi_{scatter}|^2 = v|f(\theta)\frac{e^{ikr}}{r}|^2 \tag{2.5}$$

where $v = \frac{\hbar k}{\mu}$.

If we placed a detector of area dA at a distance r from the target (scatterer) (Figure 2.2), then the solid angle $d\Omega$ subtended by the detector at the scattering centre is

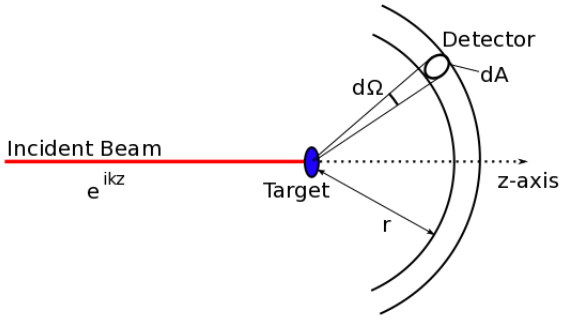

FIGURE 2.2: Scattering of a beam from a target

$$d\Omega = \frac{dA}{r^2} \tag{2.6}$$

The total number of particles goes through the area dA per unit time i.e the detector measures the number of particles per unit time, N$d\Omega$, scattered into an element of solid angle $d\Omega$ in direction (θ,ϕ) and is given by

$$\begin{aligned}Nd\Omega = &= v|f(\theta)\frac{e^{ikr}}{r}|^2 dA \\ &= v|f(\theta)e^{ikr}|^2\frac{dA}{r^2} \\ &= v|f(\theta)e^{ikr}|^2 d\Omega\end{aligned} \tag{2.7}$$

And this number is directly proportional to the number of particles per unit time crossing a unit area normal to direction of incidence (incident flux of particles), j_I. Then, the differential scattering cross-section defined as the ratio of the number of scattered particles into direction (θ, ϕ) per unit solid angle, divided by incident flux. Can be written as

$$\frac{d\sigma}{d\Omega} = \frac{N}{j_I} \tag{2.8}$$

$$\frac{d\sigma}{d\Omega} = \frac{v|f(\theta)e^{ikr}|^2}{v|e^{ikz}|^2} = \frac{|f(\theta)e^{ikr}|^2}{|e^{ikz}|^2} = |f(\theta)|^2 \tag{2.9}$$

or,

$$\frac{d\sigma}{d\Omega} = |f(\theta)|^2 \tag{2.10}$$

This is our observable quantity. In angular distributions, this differential scattering cross-section is plotted against the scattering angle.

The total cross-section can be obtained by integrating the differential cross-section over all solid angles.

$$\sigma = \int \frac{d\sigma}{d\Omega} d\Omega \tag{2.11}$$

The cross-section has a dimensions of area and can be separated into scattering (σ_s)[elastic (σ_{el}), inelastic (σ_{inel})], absorption(σ_{abs}) and transmission (σ_{tran}) depending on the sensitivity on energy of incoming particles.

$$\sigma = \sigma_s + \sigma_{abs} + \sigma_{tran} \tag{2.12}$$

For a two-body problem, the general Schrdinger equation is

$$[-\frac{\hbar^2}{2m_1}\nabla_1^2 - \frac{\hbar^2}{2m_2}\nabla_2^2 + V(\vec{r_1}, \vec{r_2}) - E]\psi(\vec{r_1}, \vec{r_2}) = 0 \tag{2.13}$$

where, m_1 and m_2 are the masses of the two particles, r_1 and r_2 are the respective position vectors, ∇_1 and ∇_2 are the corresponding operators, E is the energy of the system and V is the potential for the interaction between the particles.

In the centre of mass (CM) co-ordinate system the calculation is easier than in the laboratory system because of the fact that the six degrees of freedom in the laboratory system are reduced to three in the case of CM system. One can introduce the CM co-ordinates by

$$\vec{R} = \frac{m_1\vec{r_1} + m_2\vec{r_2}}{(m_1 + m_2)} \tag{2.14}$$

where, $\vec{R}$ is the co-ordinate of the centre of mass in the laboratory frame.
and the relative coordinate vector

$$\vec{r} = \vec{r_1} - \vec{r_2} \tag{2.15}$$

where r is the relative position vector between the two particles and

$$\vec{r_1} = \vec{R} + \frac{m_2}{m_1 + m_2}\vec{r} \tag{2.16}$$

$$\vec{r_2} = \vec{R} - \frac{m_1}{m_1 + m_2}\vec{r} \tag{2.17}$$

Therefore in the CM system the Schrdinger equation reduces to

$$[-\frac{\hbar^2}{2\mu}\nabla^2 + V(r) - E]\psi(\vec{r}) = 0 \tag{2.18}$$

where , μ is the reduced mass which can be defined by

$$\mu = \frac{m_1 m_2}{m_2 + m_2} \tag{2.19}$$

and energy of the system, E is the CM energy and can be written as

$$E = E_{Lab}\frac{\mu}{m_1} \tag{2.20}$$

where E_{Lab} is the energy in laboratory system.
The potential is assumed to be central and local, i.e

$$V(\vec{r}, \vec{r'}) = V(|\vec{r}|)\delta(\vec{r} - \vec{r'}) = V(r) \tag{2.21}$$

2.1.2 Partial Wave Analysis

Consider the potential is spherically symmetric and which is V(r). The radial part of the Schrdinger equation

$$-\frac{\hbar^2}{2m}\frac{d^2u}{dr^2} + [V(r) + \frac{\hbar^2}{2m}\frac{l(l+1)}{r^2}]u = Eu \tag{2.22}$$

where $\frac{l(l+1)}{r^2}$ is due to centrifugal contribution.
At very large r i.e in zone-III (shown in Figure 2.3), the radial Schrdinger equation become

$$-\frac{\hbar^2}{2m}\frac{d^2u}{dr^2} \approx Eu \tag{2.23}$$

or,

$$\frac{d^2u}{dr^2} \approx Eu \tag{2.24}$$

The general solution of this equation is

$$u(r) = Ce^{ikr} + De^{-ikr} \tag{2.25}$$

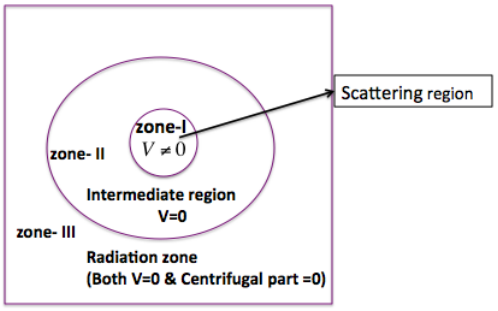

FIGURE 2.3: Scattering from localized potential: the scattering region, the intermediate region, and the radiation zone

where the first term represents as outgoing spherical wave and the second an incoming one. For scattered wave we have D=0. the solution become

$$u(r) = Ce^{ikr} \tag{2.26}$$

at very large r,

$$R(r) \approx \frac{e^{ikr}}{r} \tag{2.27}$$

which is the outgoing spherical wave.

The radial part of the Schrdinger equation in the intermediate region i.e in zone-II is

$$-\frac{\hbar^2}{2m}\frac{d^2u}{dr^2} + \frac{\hbar^2}{2m}\frac{l(l+1)}{r^2}u = Eu \tag{2.28}$$

$$\frac{d^2u}{dr^2} - \frac{l(l+1)}{r^2}u = -k^2u \tag{2.29}$$

solution of this equation is spherical Bessel function

$$u(r) = Arj_l(kr) + Brn_l(kr) \tag{2.30}$$

we get the value of u(r) using Spherical Hankel function as [45]

$$u(r) = Arh_l^{(1)} \tag{2.31}$$

Then we get,

$$R(r) = \frac{u}{r} \sim h_l^1(kr) \tag{2.32}$$

The wave function at outside of the scattering region is

$$\psi(r,\theta,\phi) = A[e^{ikz} + \sum_{l,m} C_{l,m}h_l^{(1)}(kr)Y_l^m(\theta,\phi)] \tag{2.33}$$

where $Y_l^m(\theta,\phi)$ is the spherical harmonic and which is at m=0 is

$$Y_l^m(\theta,\phi) = \sqrt{\frac{2l+1}{4\pi}} P_l(cos\theta) \tag{2.34}$$

We redefine the expansion co-efficient, $C_{l,m}$ as

$$C_{l,0} = i^{l+1} k \sqrt{4\pi(2l+1)} a_l \tag{2.35}$$

where a_l is the scattering amplitude for the l-th partial wave.
Then the wave function become

$$\psi(r,\theta,\phi) = A[e^{ikz} + k\sum_{l=0}^{\infty} i^{l+1}(2l+1)a_l h_l^{(1)}(kr)P_l(cos\theta)] \tag{2.36}$$

for large r, the Hankel function goes like $(i)^{l+1}\frac{e^{ikr}}{kr}$. Then we get

$$\psi(r,\theta,\phi) = A[e^{ikz} + k\sum_{l=0}^{\infty}(2l+1)a_l P_l(cos\theta)\frac{e^{ikr}}{r}] \tag{2.37}$$

Comparing this equation with $\psi(r,\theta,\phi) = A[e^{ikz} + f(\theta)\frac{e^{ikr}}{r}]$ and we get the scattering amplitude as

$$f(\theta) = \sum_{l=0}^{\infty}(2l+1)a_l P_l(cos\theta) \tag{2.38}$$

where a_l is called partial wave amplitude (since wave with different values of orbital angular momentum l are referred to as partial wave).

Then the differential cross-section can be written as

$$\frac{d\sigma}{d\Omega} = |f(\theta)|^2 = \sum_l \sum_{l'}(2l+1)(2l'+1)a_l^* a_{l'} P_l(cos\theta)P_{l'}(cos\theta) \tag{2.39}$$

and the total cross-section can be written

$$\begin{aligned}\sigma &= \int \frac{d\sigma}{d\Omega} d\Omega \\ &= 4\pi \int_0^{\pi} \sum_l \sum_{l'}(2l+1)(2l'+1)a_l^* a_{l'} P_l(cos\theta)P_{l'}(cos\theta)Sin\theta d\theta\end{aligned} \tag{2.40}$$

For orthogonal condition of Legendre polynomial $\int_{-1}^{1} P_l(x)P_{l'}(x)dx = \frac{2}{2l+1}\delta_{ll'}$ we get the total cross-section as

$$\sigma = 4\pi \sum_{l=0}^{\infty}(2l+1)|a_l|^2 \tag{2.41}$$

We can redefine our scattering problem in terms of calculating the phase shifts rather than partial wave amplitudes as

$$a_l = \frac{1}{2ik}(e^{2i\delta_l} - 1) = \frac{1}{k} e^{i\delta_l} sin(\delta_l) \tag{2.42}$$

where $S_l = e^{2i\delta_l}$ is the partial wave S-matrix element
Then the scattering amplitude can be written as

$$f(\theta) = \frac{1}{k}\sum_{l=0}^{\infty}(2l+1)e^{i\delta_l}sin(\delta_l)P_l(cos\theta) \tag{2.43}$$

and total cross-section is given by

$$\sigma = \frac{4\pi}{k^2}\sum_{l=0}^{\infty}(2l+1)sin^2(\delta_l) \tag{2.44}$$

At low energy, the partial wave expansion has an advantage for calculations, because in this case only the partial waves with small l-values come close to the scattering center. The partial wave can be employed only when the potential is spherically symmetric.

2.1.3 Elastic Scattering and Absorption

The elastic scattering is a type of scattering in which there is no change in the quantum state of the nucleus. The incoming and outgoing channel are same for this scattering process. The elastic scattering has an angular dependency which can be expressed by differential scattering cross-section. The reaction or absorption cross-section is a types of scattering cross-section which contains all channel in which the residual nucleus come out from different form or different state form target nucleus. In this process exit channel differs from the entrance channel.

We assumed that the nucleus is replaced by a complex potential and the complex potential is acting upon the incoming particle. The complex potential can be written as

$$V(r) = V_0 + iV_I \tag{2.45}$$

where V_0 is the real part of the potential which explains the elastic scattering. Elastic scattering describes the average potential energy of the incident particle within the nucleus. Its shape give an indication about the form of the potential well inside the nucleus.
And V_1 is the imaginary part of the potential which explains absorption or reaction. It indicates the strength and location of the processes that lead to an energy exchange between the incoming particle (neutron) and the target nucleus.

Then the phase shift, δ_l is also complex and it can be expressed as

$$\delta_l = \alpha_l + i\beta_l \tag{2.46}$$

where, α_l and β_l are real. The partial wave S-matrix element is defined as

$$S_l = e^{2i\delta_l} = e^{2i\alpha_l - 2\beta_l} \tag{2.47}$$

Then the total scattering amplitude is given as

$$f(\theta) = \frac{1}{2ik}\sum_{l=0}^{\infty}(2l+1)(S_l - 1)P_l(cos\theta) \tag{2.48}$$

where k is the wave number and P_l is the Legendre Polynomial.

The total elastic scattering cross-section is

$$\sigma_{el} = 2\pi\int_0^{\pi}|f(\theta)|^2 sin\theta d\theta = \frac{\pi}{k^2}\sum_{l=0}^{\infty}(2l+1)|1 - S_l|^2 \tag{2.49}$$

And the total absorption cross-section is obtained as

$$\sigma_{abs} = \frac{\pi}{k^2}\sum_{l=0}^{\infty}(2l+1)(1 - |S_l|^2) \tag{2.50}$$

The total scattering cross-section is

$$\sigma = \frac{2\pi}{k^2}\sum_{l=0}^{\infty}(2l+1)[1 - Re(S_l)] = \sigma_{el} + \sigma_{abs} \tag{2.51}$$

Sometimes we use reaction cross-section instead of absorption cross-section. Then total cross-section [2] can be written as

$$\sigma = \sigma_{el} + \sigma_r \tag{2.52}$$

where σ_{el} is the elastic scattering cross-section and σ_r is the reaction cross-section.

The elastic scattering cross-section can be divided into two parts including shape elastic scattering cross-section and compound elastic cross-section.

$$\sigma_{el} = \sigma_{se} + \sigma_{ce} \tag{2.53}$$

where, σ_{ce} is the compound elastic cross-section and which is part of elastic scattering that comes from the compound nucleus and the subsequent emission of incident particle at the entrance channel. σ_{se} is the shape elastic scattering cross-section and which is a part of the elastic scattering which occurs without the formation of compound nucleus.

From the compound nucleus hypothesis, we know that all the possible actual reactions to occur after compound formation. Hence, the cross-section of the compound nucleus can be written as

$$\sigma_c = \sigma_{ce} + \sigma_r \tag{2.54}$$

where σ_r is the cross-section for reaction or absorption.

The scattering which the incident particle suffer in Eq. 2.45 should be reproduced from the shape

elastic scattering and absorption caused by the imaginary part V_1 should reproduce the compound nucleus formation. The total cross-section can be written as

$$\sigma = \sigma_{se} + \sigma_{ce} + \sigma_r \tag{2.55}$$

and finally comparing Eq. 2.54 and Eq. 2.55 , we can write

$$\sigma = \sigma_{se} + \sigma_c \tag{2.56}$$

The total cross-section is sum of the shape elastic cross-section and cross-section of compound nucleus.

2.2 Optical Model Analysis

The optical model was established by H. Freshbach and his collaborators in 1953 [46] and in this model, the interaction with the nuclei in a reaction is described by a complex potential U(r), where r be the distance between the two nuclei. In a optical model, nucleus can also be represented by a complex potential. Where the real part of the potential explains elastic scattering and the imaginary part of the potential describes inelastic scattering or absorption or reaction. The optical potential can be written as

$$U(r) = U_R(r) + U_I(r) + U_D(r) + U_S(r) + U_c(r) \tag{2.57}$$

where the first term of the right hand side of Eq. 2.57 $U_R(r)$ =-Vf(r,R,a)= is the real part of the potential and represents a nuclear well with depth -V, being multiplied by a Wood-Saxon form factor,

$$f(r, R, a) = [1 + exp[(r - R)]/a]^{-1} \tag{2.58}$$

where R is the radius of the nucleus and a be the diffuseness parameter of the potential.
The 2nd and 3rd terms of the right hand side of Eq. 2.57 are the imaginary part of the potential. Those are

$$U_I(r) = -iW_V f(r, R_I, a_I) \tag{2.59}$$

and

$$U_D(r) = 4ia_I W_D df(r, R_I, a_I) \tag{2.60}$$

An imaginary part produces absorption. U_I is responsible for the absorption in the whole volume of the nucleus but U_D is responsible in the region close to the nuclear surface. At low energies there are no available unoccupied states for the nucleons inside the nucleus and the interactions are essentially at the surface. In this case (at low energies) U_D important and U_I is ignored. And at higher energies, the incident particle has larger penetration and that is why in this case U_I is important.

The fourth terms of the right hand side of Eq. 2.57, $U_S(r)$ = is the spin-orbit terms of the potential. And can be written as

$$U_S(r) = V_s \frac{1}{r} \frac{d}{dr} f(r, R_S, a_S) \vec{s}.\vec{l} \tag{2.61}$$

where s is the spin operator and l be the angular orbital momentum operator. $U_S(r)$ is only important at the surface of the nucleus as it contains the derivative of the form factor f. The values of V_S, R_S and a_S must be adjusted by experiment.

The presence of the term U_S is needed to describe the effect of polarization. The polarization can be written as

$$P = \frac{N_c - N_b}{N_c + N_b} \tag{2.62}$$

where N_c is the number of nucleons in the beam with spin up andN_b is the number of the nucleons in the beam with spin down.

And the final term of the right hand side of Eq. 2.57 is the Coulomb potential and can be written as

$$U_c(r) = \frac{Z_1 Z_2 e^2}{2R_e}(3 - \frac{r^2}{R_c^2}) for\ (r \leq R_c) \tag{2.63}$$

where it is assumed that the nucleus is a homogeneously charged sphere of radius equal to the Coulomb barrier radius, R_c.

2.2.1 The optical Model of Scattering

In optical model, the interaction potential between neutron-nucleus is complex and can be written as [2] for r$<R$

$$U(r) = V_0 + iV_1 \tag{2.64}$$

and for r>R,

U(r)=0.

where V_0 is the real part of the potential and V_1 is the imaginary part of the potential.

We have $V_0 = -U$ and $V_1 = \xi V_0$, where ξ is a parameter which indicate an absorption for neutrons within nuclear matter. Then the complex potential for r$<R$ can be written as [46]

$$U(r) = -U(1 + i\xi) = -U - iW \tag{2.65}$$

where $W = U\xi$.

The Schrodinger equation for scattering due to a complex potential [47] is given by

$$\nabla^2\psi + \frac{2\mu}{\hbar^2}(E - U(r))\psi = 0 \tag{2.66}$$

Comparing Eq. 2.65 and Eq. 2.66 we get

$$\nabla^2\psi + \frac{2\mu}{\hbar^2}(E + U + iW)\psi = 0 \tag{2.67}$$

Multiplying by ψ^* on both side of Eq. 2.67 we get

$$\psi^*\nabla^2\psi + \frac{2\mu}{\hbar^2}(E + U + iW)\psi^*\psi = 0 \tag{2.68}$$

Taking complex conjugate of Eq. 2.67 we get

$$\nabla^2\psi^* + \frac{2\mu}{\hbar^2}(E + U - iW)\psi^* = 0 \tag{2.69}$$

Multiplying by ψ on both side of Eq. 2.69 we get

$$\psi\nabla^2\psi^* + \frac{2\mu}{\hbar^2}(E + U - iW)\psi\psi^* = 0 \tag{2.70}$$

and subtracting Eq. 2.68 and Eq. 2.70 we get

$$\psi^*\nabla^2\psi - \psi\nabla^2\psi^* = -\frac{4i\mu W}{\hbar^2}\psi\psi^* \tag{2.71}$$

The quantum mechanical current density can be expressed as

$$\vec{j} = \frac{\hbar}{2i\mu}(\psi\vec{\nabla}\psi - \psi\vec{\nabla}\psi) \tag{2.72}$$

taking divergence of (2.72) and then using (2.71), one can write

$$\vec{\nabla}.\vec{j} = \frac{2}{\hbar}W\psi\psi^* \tag{2.73}$$

the probability density is $\psi^*\psi$ and $W = \frac{\hbar}{2}$vK, where K is the absorption co-efficient, the Eq. 2.73 is equivalent to the classical continuity equation.

$$\frac{\partial\rho}{\partial t} + \vec{\nabla}.\vec{j} = Kv\rho \tag{2.74}$$

Here v is the velocity of the particle inside the nucleus. A steady state has been attained so that the term $\frac{\partial\rho}{\partial t}$ in the above equation vanishes. Eq. (2.73) shows that W>0, the imaginary part of the complex potential has the effect of absorbing flux from the incident beam.

The scattering amplitude is given by [47]

$$f(\theta) = \frac{1}{2ik}\sum_L(2l+1)(S_l - 1)P_l(cos\theta) \tag{2.75}$$

where $S_l = e^{2i\delta_l}$ is the partial wave S-matrix element for the l-th partial wave, δ_l being the phase shift, l is the orbital angular momentum.

Then, the differential cross-section is given by

$$\frac{d\sigma}{d\Omega} = |f(\theta)|^2 = \frac{1}{4k^2}|\sum_L(2l+1)(1 - S_l)P_l(cos\theta)|^2 \tag{2.76}$$

Integration of (2.76) over angles gives the total elastic scattering cross section.

$$\sigma_{el} = \frac{\pi}{k^2}\sum_l (2l+1)|1-S_l|^2. \tag{2.77}$$

The total absorption cross-section, that measures the loss of flux from the elastic channel, is given as

$$\sigma_{abs} = \frac{\pi}{k^2}\sum_l (2l+1)(1-|S_l|^2) \tag{2.78}$$

Now the total cross-section is given by,

$$\sigma = \sigma_{el} + \sigma_{abs} = \frac{2\pi}{k^2}\sum (2l+1)(Re(S_l)) \tag{2.79}$$

2.3 Discrete Levels of the Compound Nucleus

Consider the projectile particle is a and the target nucleus is X. By their interaction CN, C^* is created and then the CN decay to entrance channel as

$$a + X \rightarrow C^* \rightarrow Y + b \tag{2.80}$$

where C^* is the CN of the excited state. and b in the out going particle.
For neutron capture reaction we can write the equation as

$$n + {}^{A}X \rightarrow [{}^{A+1}X]^* \rightarrow {}^{A+1}X + \gamma \tag{2.81}$$

Kinetic energy of the excited CN, $E^*=S_n+E_n$. Figure 2.4 shows the energy level of CN and Figure 2.5 shows the decaying level of CN.

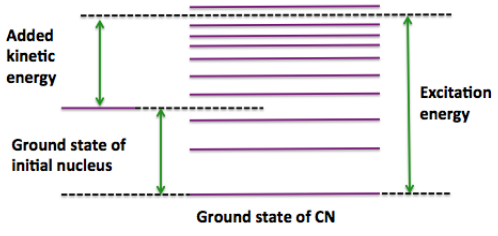

FIGURE 2.4: Energy level of CN

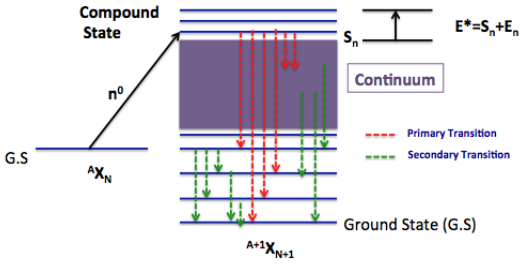

FIGURE 2.5: Decaying level of CN

The wave function of the state of the CN is given by

$$\begin{aligned}\psi(t) &= \psi_0 e^{-(\frac{iE_r t}{\hbar})} e^{(-\frac{\Gamma t}{2t})} \\ &= \psi_0 e^{-(E_r - \frac{i\Gamma}{2})\frac{t}{\hbar}}\end{aligned} \tag{2.82}$$

where $\frac{\Gamma}{2}$ is the half width of the level (decaying state which life time is $\tau = \frac{\hbar}{\Gamma}$). and E_r=is the energy of excitation of the CN.

This wave function does not represent a stationary state. We can get the superposition of states of different energies by Fourier integral method

$$\psi(t) = \int_{-\infty}^{\infty} A_E e^{(-\frac{iEt}{\hbar})dE} \tag{2.83}$$

By taking the Fourier transform of Eq. 2.83 we can get the amplitude A_E

$$\begin{aligned} A_E &= \frac{1}{2\pi}\int_0^{\infty} \psi(t')e^{(\frac{iEt'}{\hbar})dt'} \\ &= \frac{1}{2\pi}\int_0^{\infty} \psi_0 e^{[i(E-E_r+i\frac{i\Gamma}{2})\frac{t'}{\hbar}]} \end{aligned} \tag{2.84}$$

Taking positive value we get amplitude after integrating as

$$A_E = \frac{\psi_0}{2\pi}\frac{i\hbar}{E - E_r + i\frac{\Gamma}{2}} \tag{2.85}$$

and

$$|A_E|^2 = \frac{|\psi_0|^2}{4\pi^2}\frac{\hbar^2}{(E-E_r)^2 + \frac{\Gamma^2}{4}} \tag{2.86}$$

The cross-section for for the formation of the compound nucleus as [48]

$$\sigma_a = \pi ƛ^2 \frac{\Gamma_a \Gamma}{(E-E_r)^2 + \frac{\Gamma^2}{4}} \tag{2.87}$$

The relative probability of CN through exit channel Y+b is $\frac{\Gamma_b}{\Gamma}$. Then the cross-section for the reaction X(a,b)Y is given by

$$\sigma(a,b) = \sigma_a \frac{\Gamma_b}{\Gamma} = \pi ƛ^2 \frac{\Gamma_a \Gamma_b}{(E-E_r)^2 + \frac{\Gamma^2}{4}} \tag{2.88}$$

Eq. 2.88 is known as the Breit-Wigner one level formula for spin less nucleus at very low energies so that l=0 for entrance channel. for higher energies i.e $l \neq 0$, one need to account the statistical factor of compound state formed with spinless nucleus x and X we get, $g_l = 2I_C + 1 = 2l + 1$, then we can write the Eq. 2.87 and Eq. 2.88 as

$$\sigma_a = \pi ƛ^2 (2l+1) \frac{\Gamma_a \Gamma}{(E-E_r)^2 + \frac{\Gamma^2}{4}} \tag{2.89}$$

$$\sigma(a,b) = \pi ƛ^2 (2l+1) \frac{\Gamma_a \Gamma_b}{(E-E_r)^2 + \frac{\Gamma^2}{4}} \tag{2.90}$$

Particle with spin:

Consider projectile particle, x has a spin I_a and the target nucleus has spin I_X then we get spin of CN as $I_c = I_X + I_a + l$ and the statistical factor -g can be written as [48]

$$g = \frac{2I_c + 1}{(2I_X + 1)(2I_a + 1)} \tag{2.91}$$

Then the cross-section of X(a,b)Y reaction with the particle with spins can be written as

$$\sigma(a,b) = \pi\lambda\!\!\!^{-2} g \frac{\Gamma_a \Gamma_b}{(E-E_r)^2 + \frac{\Gamma^2}{4}} \tag{2.92}$$

Neutron resonances at low energy:

When the reaction undergo compound elastic scattering , we have $b \equiv a$ so that $\Gamma_b = \Gamma_a$. Then Eq. 2.92 becomes

$$\sigma_{el}^{(l)} = \sigma(a,a) = \pi\lambda\!\!\!^{-2} g \frac{\Gamma_a^2}{(E-E_r)^2 + \frac{\Gamma^2}{4}} \tag{2.93}$$

In the resonance position we know $E = E_r$, then Eq. 2.93 become

$$\sigma_{el}^{(l)} = 4\pi\lambda\!\!\!^{-2} g (\frac{\Gamma_a}{\Gamma})^2 \tag{2.94}$$

For a projectile neutron of low energy $(l = 0)$, only exit channel (n,n) and (n,γ) are opened. Hence $\Gamma = \Gamma_n + \Gamma_\gamma \approx \Gamma_\gamma$ since $\Gamma_n << \Gamma_\gamma$ we get

$$\sigma(n,n) = \pi\lambda\!\!\!^{-2} g (\frac{\Gamma_n^2}{(E-E_r)^2 + \frac{\Gamma^2}{4}} \tag{2.95}$$

$$\sigma(n,\gamma) = \pi\lambda\!\!\!^{-2} g (\frac{\Gamma_n \Gamma_\gamma}{(E-E_r)^2 + \frac{\Gamma^2}{4}}) \tag{2.96}$$

In the time of resonance Eq. 2.95 and Eq. 2.96 becomes

$$\sigma(n,n) = \sigma_{el} = 4\pi\lambda\!\!\!^{-2} g (\frac{\Gamma_n}{\Gamma})^2 \tag{2.97}$$

$$\sigma(n,\gamma) = \sigma_{abs} = 4\pi\lambda\!\!\!^{-2} g (\frac{\Gamma_n}{\Gamma_\gamma})^2 \tag{2.98}$$

2.3.0.1 Interference Between Resonance and Potential Elastic Scattering

Consider the case in which both the resonance and potential scattering are taken place together. For that case, we need to combine the amplitude due to potential scattering, A_{pot} with the amplitude of resonance scattering. Then the total elastic scattering cross-section can be written as

$$\sigma_{el} = \pi\lambda\!\!\!^{-2} [A_{pot} + A_{res}]^2 \tag{2.99}$$

By putting the value of amplitudes we can write the total scattering cross-section as

$$\sigma_{el} = \pi\lambda\!\!\!^{-2} |2e^{ikR} sinkR + \frac{\Gamma}{(E-E_r) + i\Gamma/2}|^2 \tag{2.100}$$

Where,

A_{pot}=$2e^{ikR} sinkR$ and A_{res}=$\frac{\Gamma}{(E-E_r)+i\Gamma/2}$ and R is the effective radius of the nuclei.

For far away from the resonance point , the potential scattering is dominant i.e $A_{res} << A_{pot}$. Then

equation of the total scattering cross-section is become

$$\sigma_{el} = 4\pi ƛ^2 sin^2 kR \tag{2.101}$$

If $kR << 1$ we get

$$\sigma_{el} = 4\pi R^2 \tag{2.102}$$

which is four times of the geometrical cross-section. Potential scattering represents the scattering cross-section between the resonances. The potential scattering is dominant for light nuclei.

At resonance, the resonance scattering amplitude is much larger than the potential scattering amplitude. So the total scattering cross-section dominant by resonance amplitude. So we can write

$$\sigma_{el} = \pi ƛ^2 \frac{\Gamma^2}{(E - E_r)^2 + \Gamma^2/2} \tag{2.103}$$

the value of cross-section become maximum at resonance $E = E_r$

$$\sigma_{el} = 4\pi ƛ^2 \tag{2.104}$$

In a region near the energy E_r, the scattering cross-section shows typical resonance shape common to many phenomena, most notable the refractive index of a medium near the absorption line. When the two amplitudes are of the same order, there is interference between them. For $E < E_r$, A_{res} and A_{pot} have opposite signs, so that they interfere destructively. For $E > E_r$, they have same sign and they produce constructive interference [48].

2.3.1 Capture Cross-Section

2.3.1.1 Briet-Wigner Formalism

The thermal capture cross-sections can be conveniently explained by the Briet-Wigner formalism [7]. The Briet-Wigner single-level resonance formula can be written as

$$\sigma_\gamma(E_c) = \sigma(n,\gamma) = \pi ƛ^2 g \frac{\Gamma_n \Gamma_\gamma}{(E_c - E_r)^2 + \frac{\Gamma^2}{4}} \tag{2.105}$$

where E_r is the resonance energy in the CM system. We know the relation between the CM energy,E_c and the laboratory energy E_L, as $E_c = \frac{A}{A+1} E_L$ For heavy nuclei it can be $E_c \cong E_L$.
Γ_n is the width of the neutron. It has the an energy dependency of the form:

$$\Gamma_n(E_c) = \Gamma_n(E_r)\sqrt{\frac{E_c}{E_r}} \tag{2.106}$$

Γ_γ is the width of the reaction (or width of the CN)
Γ is the total width. Total width at (E_r)

$$\Gamma = \Gamma_n(E_r) + \sum_\gamma \Gamma_\gamma \tag{2.107}$$

g is the statistical factor that measure the probability that a particular compound state and can be written as

$$g = \frac{2J+1}{2(2I+1)} \tag{2.108}$$

where I is the spin of the target nuclei for a given orbital angular momentum l. J is the spin of the CN which is bound as

$$|I - l \pm \frac{1}{2}| \leq J \leq |I + l + \frac{1}{2}| \tag{2.109}$$

At low energy neutron, resonances are likely to be s-wave l=0 and we get

$$g = \frac{1}{2}(1 \pm \frac{1}{2I+1}) \tag{2.110}$$

ƛ is the reduced neutron wave-length. ƛ can be written as

$$ƛ = \frac{\hbar}{\sqrt{(\frac{Mm}{M+m})2E_c}} \tag{2.111}$$

where, M is the target mass and m is the neutron mass. The reduced neutron wavelength can also be written as

$$ƛ^2 = ƛ_0^2 \frac{E_r}{E_c} \tag{2.112}$$

Here $ƛ^2$ can be written as

$$ƛ_0^2 = \lambda^2(E_r) = \frac{\hbar^2}{\frac{Mm}{M+m}2E_r} \cong \frac{A+1}{Am}\frac{\hbar^2}{2E_r} \tag{2.113}$$

Substituting the Eq. 2.110 and Eq. 2.106 into Eq. 2.105 and we get

$$\sigma_\gamma(E_c) = \pi ƛ_0^2 \frac{E_r}{E_c} g \frac{\Gamma_n(E_r)\sqrt{\frac{E_c}{E_0}}\Gamma_\gamma}{(E_c - E_r)^2 + \frac{\Gamma^2}{4}} = 4\pi ƛ_0^2 g \sqrt{\frac{E_r}{E_c}} \frac{\Gamma_n(E_r)\Gamma_\gamma}{4(E_c) - E_r)^2 + \Gamma^2} \tag{2.114}$$

The Eq. 2.114 can be rewritten as

$$\sigma_\gamma(E_c) = 4\pi ƛ_0^2 g \frac{\Gamma_n(E_r)}{\Gamma}\frac{\Gamma_\gamma}{\Gamma}\sqrt{\frac{E_r}{E_c}}\frac{\Gamma^2}{4(E_c - E_r)^2 + \Gamma^2} = \sigma_0 \frac{\Gamma_\gamma}{\Gamma}\sqrt{\frac{E_r}{E_c}}\frac{\Gamma^2}{4(E_c - E_r)^2 + \Gamma^2} \tag{2.115}$$

Eq. 2.115 is the well-known Breit-Wigner equation.

Where

$$\sigma_0 = 4\pi ƛ_0^2 g \frac{\Gamma_n(E_0)}{\Gamma} = 4\pi \frac{A+1}{Am}\frac{\hbar^2}{2E_r} g \frac{\Gamma_n(E_r)}{\Gamma} = \frac{4\pi\hbar^2}{2m}\frac{A+1}{E_0 A}\frac{g\Gamma_0(E_r)}{\Gamma} \tag{2.116}$$

putting the value of the constants we get σ_0

$$\sigma_0 = \frac{2.608\times10^6}{E_r}\frac{A+1}{A}\frac{g\Gamma_n(E_r)}{\Gamma} \tag{2.117}$$

At resonance ($E_c = E_r$), the value of the cross-section become $\sigma_0\frac{\Gamma_\gamma}{\Gamma}$.

2.3.1.2 Westcott Factor, g_w

Neutron capture reaction cross sections are measured generally by techniques on a relative basis. Westcott [7] developed a method for converting the thermal cross-section σ_0 (also know as 2200 ms^{-1}) to effective cross-section, $\hat{\sigma}$ by describing the neutron spectrum as a combination of Maxwellian-Boltzmann distribution characterized by temperature,T and a component of epithermal energy neutrons. Neutron flux distribution for epithermal neutron is proportional to the reciprocal of the neutron energy i.e $\frac{dE}{E}$.

The effective cross-section, for an isotope whose cross-section does not vary inversely with the neutron velocity, is given by

$$\hat{\sigma} = \sigma_0(g_w + rs) \tag{2.118}$$

where, g_w is the Westcott factor, r is the epithermal index (which is approximately the fraction of the total neutron density in the epithermal component), ans s is a temperature dependent quantity and which is given by

$$s = \sqrt{\frac{4T}{\pi T_0}}\frac{I'}{\sigma_0} \tag{2.119}$$

where $I^{'}$ is the reduced resonance integral.
Consider a case in which epithermal component is absent i.e r=0. For this case the g_w factor is the ratio of the Maxwellian averaged cross-section, σ to the 2200 m/sec cross-section, σ_0

$$g_w = \frac{\sigma}{\sigma_0} = \frac{1}{v_0\sigma_0}\int_0^\infty \frac{4}{\sqrt{\pi}}\frac{v^3}{v_T^3}e^{-(\frac{v}{v_T})^2}\sigma(v)dv \tag{2.120}$$

where v_T is the most portable velocity for a Maxwellian spectrum specified by the temperature T and is given by

$$v_T = \sqrt{\frac{2kT}{m}} = \sqrt{\frac{2E_n}{m}} \tag{2.121}$$

where k is the Boltzmann constant and m is the mass of the neutron.

At room temperature i.e T=293 K we have E_n=0.0253eV and v_T=2200 m/sec. It can be easily shown that if the cross-section varies as 1/v, then the Maxwellian capture cross-section is equivalent to 2200 m/sec value and then g_w=1. The accuracy of the g_w factors depends on the accuracy of the slope of the cross-section.

Chapter 3

Germanium Detector

3.1 Semiconductor Detector

A semiconductor detector is a device which uses a semiconducting material to measure the energy loss of ionization from effect of incident charged particles or photons. These detectors are the detectors of choice for the γ-ray studies. Often used semiconductor detectors are silicon (Si) or germanium (Ge) based. The germanium semiconductor detector was first introduced in 1962. These detectors directly collect the charges produced by the ionization of the semiconductor material, when a charged particle posses through. The energy required to produce one electron-hole pair is about 3 eV energy [49].

3.2 Semiconductor Properties

3.2.1 Band Structure in Solids

The allied energy bands for electrons (those electrons is exited within the same solid) is constituted by the periodic lattice of crystalline materials. One of these energy bands contains the energy of any electron within the pure material and this energy bands are separated by gaps i.e ranges of forbidden energies (shown in Figure 3.1).

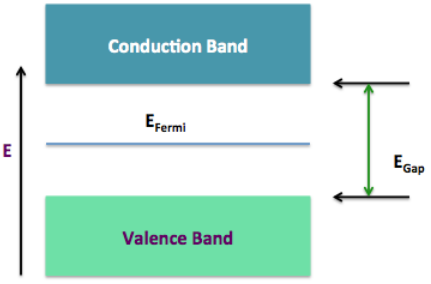

FIGURE 3.1: Band structure of a semiconductor

The lower band is known as the valence band and is populated by outer-shell electrons that are bound to specific lattice sites within the crystal. The next higher-lying band is called the conduction band and represents electrons that are free to migrate through the crystal [50]. These two energy bands (both conduction band and valence band) are separated by the band gap. The size of the band gap determines whether the material is classified as a semiconductors or an insulator. For insulators, the band gap is usually 5 eV and for semiconductor the band gap is about 1 eV.

3.2.2 Charge Carriers

There is an excitation process in atom which elevates an electron from the valence band to the conduction band and leaves a vacancy (a hole) in the valence band. The combination of this two charges is known as the electron-hole pair. The negatively charged electron in the conduction band can be forced to move under the influence of an applied electric field. The positively charged hole, will also tend to move in an electric field, but in the opposite direction of the electron [50]. The motion of these both charges contributes to the observed conductivity of the material. The probability per unit time that an electron-hole pair is thermally generated and can be written as

$$p(T) = C_p T^{3/2} \exp(-\frac{E_g}{2kT}) \tag{3.1}$$

where T is the absolute temperature, E_g is the Band gap energy, k is the Boltzmann constant and C_p is the proportionality constant characteristic of the material

3.3 Types of Semiconductor

There are three different types of semiconductors : (1) Intrinsic semiconductor, (2) n-type semiconductor, (3) p-tpye semiconductor.

3.4 p-n junction Semiconductor Detector

A p-n junction is created in such a way that no current can pass through the junction unless the ionising radiation fall on it (shown in Figure 3.3). The standard method of forming a p-n junction is to change the impurity concentration of one side of the material so that both sides can have opposite configurations, which is known well as doping.

The junction which formed between p and n type semiconductor, represents a discontinuity in the electron density. There is a net diffusion from the higher density side to the lower density side takes place for both electrons and holes. A net negative space charge on the p-type side and a net positive space charge on the n-type side of the junction is built due the effect of the diffusion from each side

of the junction. The assembled space charge creates an electric field which decreases the tendency for further diffusion. At the time of equilibrium, the field is sufficient to prevent additional diffusion across the junction and a steady state charge distribution is established [50]. The region over which the imbalance is established, is known as the depletion region or depletion zone.

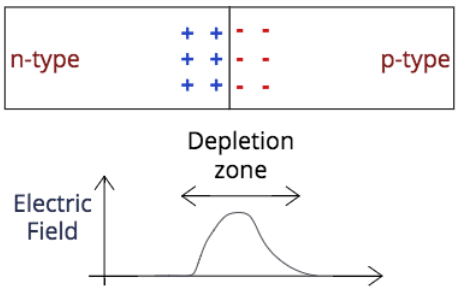

FIGURE 3.2: p-n junction detector

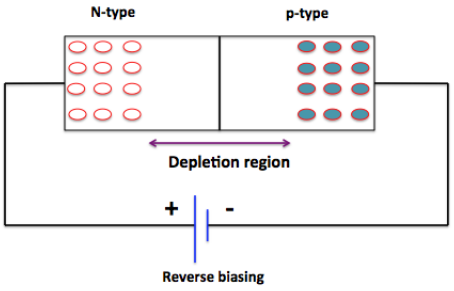

FIGURE 3.3: p-n junction detector

This depletion region or zone will work as a radiation detector (shown in Figure 3.2). The thickness of the depletion region is very small, that is why only a small volume of the crystal acts as a radiation detector, which needs to enlarge. The p-n junction semiconductor detector operates much better as a radiation detector in a reverse condition because this reverse biasing make the depletion layer larger. The performance of the p-n junction semiconductor detector depends on the thickness of the depletion region and which is inversely proportional to the net impurity concentration of the detector material.

The thickness of the depletion layer is given by

$$d = (\frac{2\epsilon_d V}{eN})^{\frac{1}{2}} \tag{3.2}$$

where, V is the reverse bias voltage, N is the net impurity concentration in the bulk semiconductor material, e is the electric charge and ϵ_d is the dielectric constant.

3.5 Configuration of Ge detector

3.5.1 The High Purity Ge (HPGe) Detector Fabrication

The high purity Ge (HPGe) detectors are created by purifying the germanium element heavily and growing it into a crystal. The techniques were first established in the mid 1970s for the production of ultra pure Ge with impurity levels as low as 10^{10} atoms/cm^3 [50]. It has a higher resistivity, which is proportional to the square of the depletion layer's thickness.

Characteristic of HPGe detector:

(1) High atomic number.

(2) Low impurity concentration.

(3) Large depletion depth.
(4) Low ionising energy required to produce an electron-hole pair.
(5) High resolution.

3.5.2 Planar Configuration

It is a representative configuration for a planar HPGe detector fabricated from high-purity p-type (or $\pi - type$) germanium [50] shown in Figure 3.4. Here, the electrical contacts are provided on the two flat surfaces of a Ge disk. There is a n^+ contact and which can be created either by lithium evaporation and diffusion onto one surface of the wafer, or by direct implantation of donor atoms using an accelerator. The detector depletion region is formed by reverse biasing this $n^+ - p$ junction shown in Figure 3.4.

There is a non-injecting contact for a majority charge carriers in the opposite face of the crystal.

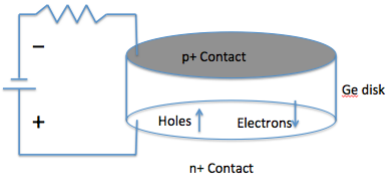

FIGURE 3.4: $n^+ - p$ junction detector (planar configuration)

It may consist of a p^+ contact produced by ion implantation of acceptor atoms or a metal-semiconductor surface barrier that acts as the electrical equivalent [50]. The p-type contacts can be formed by implanting boron and n-type contacts can be formed by implanting phosphorus.

3.5.3 Co-axial Configuration

For the case of cylindrical or co-axial geometry, one electrode is fabricated at the outer cylindrical surface of a long cylindrical Ge crystal [50]. There is another cylindrical contact which is provided by removing the core of the crystal and placing a contact over the inner cylindrical surface. There is a big active volumes can be produced, because the crystal can be created long in the axial direction. Figure 3.5 shows the large volume co-axial HPGe detectors (left one is true coaxial and right one is closed ended coaxial).

Coaxial geometry has a small inner diameter and large-volume detectors which is fabricated using lower capacitance than planar geometry. In a close ended co-axial configuration, the only one part of the central core is removed and the outer electrode is enlarge over one flat end of the cylindrical crystal. To avoid the difficulties in dealing with leakage currents at the front surface of the detectors, the closed ended configuration is chosen over a true coaxial geometry in most of commercial fabricators of HPGe detectors.

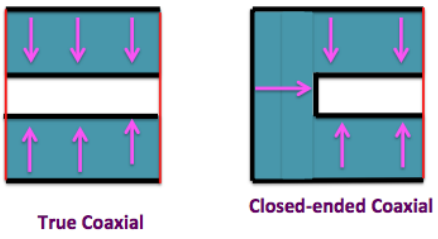

FIGURE 3.5: Large Volume Co-axial HPGe detectors

3.6 Germanium Detector Operational Characteristics

3.6.1 Detector Cryostat and Dewar

Germanium (Ge) has a small band gap (0.7 eV). It is impossible for a Ge detector to operate at room temperature because of large thermally induced leakage currents. To keep excellent energy resolution, Ge detector must need be cooled to reduce the leakage current before starting the operation. Generally, liquid nitrogen is used to reduce the temperature of the Ge detector to 77 K [50]. The temperature is reduced by using an insulated dewar where a reservoir of liquid nitrogen kept in thermal contact with the Ge detector. Low temperature has to be maintained for Ge (Li) detectors to avoid a catastrophic redistribution of the drifted lithium. In HPGe detectors, there is no lithium drifting so they can allow to warm room temperature while using. Ge(Li) detectors are replaced by HPGe detectors due to their operational advantage. Figure 3.6 shows the schematic diagram of a typical Ge detector.

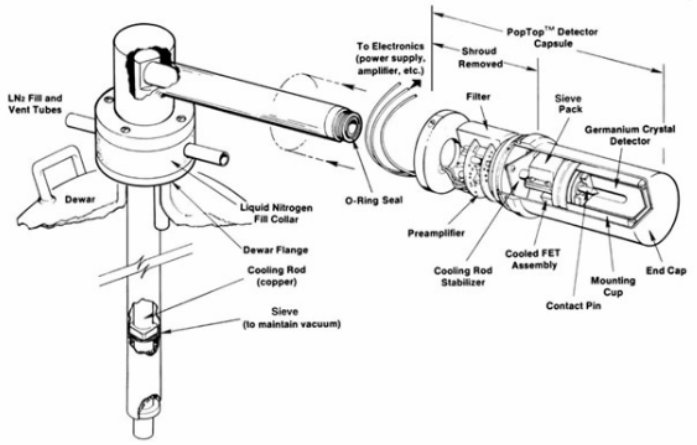

FIGURE 3.6: Ge detector operational characteristics [51]

The detector needs to be put in a vacuum tight cryostat to subdue thermal conductivity between the crystal and the surrounding air. Though HPGe detectors operate at liquid nitrogen temperature, in some cases it may be more convenient to allow this Ge detector's temperature to rise above this nominal 77 K value [50]. There are lots of coolers which are used as a alternative to liquid nitrogen cooling. Mechanical coolers are commercially available that can substitute for liquid nitrogen and that can be

quite effective.

Germanium detectors also are mainly fitted with an interlock that prevents application of high voltage to the detector unless it has achieved a low temperature.

3.7 Interaction of γ Radiation with Detector Crystal

γ ray detection depends on the effects of a γ ray interactions with matter. A γ ray can interact with matter in different ways. The main interaction types of γ rays with matter are : (1) the photo effect both in its photoelectric and photo-nuclear forms (2) Compton scattering and (3) Electron positron pair production. In a small margin, photo-fission, Rayleigh scattering and Thomson scattering are also occurred.

The γ ray can be interacted with the entire atom (as in the photoelectric effect), or with one electron in the atom (as in the Compton effect), or with the atomic nucleus (as in pair production) [49]. The characteristics of these interaction are important in detector design.

3.7.1 Photoelectric Effect

In the photoelectric effect, a photon undergoes an interaction with an detector (absorber) atom which is absorbed the γ rays completely a photo-electron is ejected by the atom from its bound shells (shown in Figure 3.7).

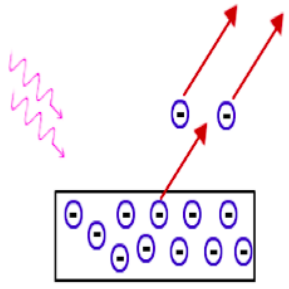

FIGURE 3.7: Photoelectric effect

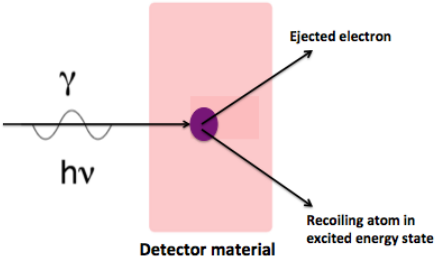

FIGURE 3.8: Photo-electric effect

In the photoelectric effect, the γ ray transfers all of its energy to the recoil electron (shown in Figure 3.8). That is why the recoil electron is ejected from the shell of the atom and hence creates the electron-hole pairs in the detector that generate the output pulse in semiconductor detector. The output pulse produced by the detector is proportional to the energy of the γ ray which made the interaction. This γ ray energy is shared between the kinetic energy of the knocked out electron and the characteristic transition radiation according to the conservation of energy equation as

$$E_\gamma = E_r + E_a + E_B \tag{3.3}$$

where, E_γ is the kinetic energy of the initial gamma γ ray, E_e is the kinetic energy acquired by the knocked out electron, E_a is the kinetic energy of the recoiling atom. E_B is the binding energy of the electron in the atom, equal to the excitation energy of the atom after electron ejection, for K-shell electrons:

$E_B = 16.6(Z-1)^2 eV$

where Z is the atomic number.

The kinetic energy of the recoil atom is of the order of : $(\frac{m_e}{M})E_e$, where, M is the mass of the atom and m_e is the mass of the electron.

As recoil energy, $(\frac{m_e}{M})E_e \approx 10^{-4}$ eV, we can be neglected the recoil energy E_a in equation (3.3), which leads to

$$E_e = E_\gamma - E_B = h\nu - E_B \tag{3.4}$$

Conservation of momentum also applies :

$$\vec{p_\gamma} = \vec{p_e} + \vec{p_a} \tag{3.5}$$

where p_γ is the momentum of γ ray, p_e is the momentum of knock out electron and p_a is the momentum of the recoiling atom.

The photoelectric interaction cross section is inversely proportional to the gamma photon energy and proportional to the atomic number Z.

3.7.2 Compton Effect

The Compton effect is dominant for all energies except the very lowest and very highest energy. It also contributes to the full energy peak by multiple Compton scattering in such a way that the last interaction is a photoelectric one and the preceding Compton interactions take place in the Ge crystal. In large-volume detectors, the probability of observable multiple Compton scattering increases. For the case if the last interaction does not occur by the photoelectric effect or if one of the multiple Compton interactions takes place outside the sensitive volume of the detector, the pulse will definitely contribute to the Compton continuum. Figure 3.9 shows the characteristic of Compton scattering inside detector material.

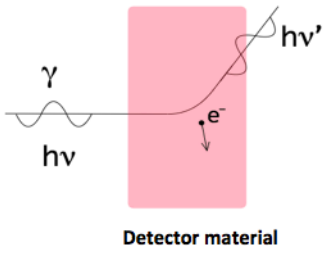

FIGURE 3.9: Compton scattering inside the detector material

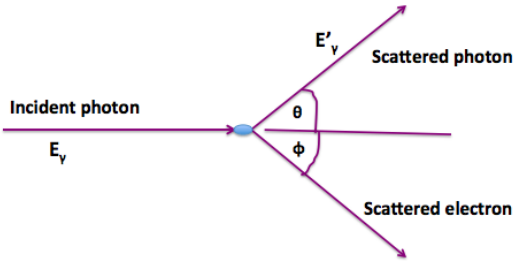

FIGURE 3.10: Geometry of Compton scattering

Consider λ is the wave length of the γ before scattering and $\lambda^{'}$ is the wave length of the photon after scattering and θ is the scattering angle of the gamma photon (shown in Figure 3.10), then we can write the wave length shift as,

$$\Delta\lambda = \lambda^{'} - \lambda = \lambda_0(1 - cos\theta) \tag{3.6}$$

where λ_0 is the Compton wave length of the electron.
It is defined as,

$$\lambda_0 = \frac{h}{m_0 c} \tag{3.7}$$

where m_0 is the electron mass and h is Plank's constant.
The comparison between the energy of incident photon E_γ and the scattered photon E'_γ is

$$E'_\gamma = \frac{E_\gamma}{1 + (\frac{E_\gamma}{mc^2})(1 - cos\theta)} \tag{3.8}$$

where $E_\gamma = h\nu$ and $E^{'}_\gamma = h\nu^{'}$.
The kinetic energy of the scattered electron can be written as

$$T_e = E_\gamma - E'_\gamma = \frac{E^2_\gamma(1 - cos\theta)}{mc^2 + E_\gamma(1 - cos\theta)} \tag{3.9}$$

At θ=180 deg, the kinetic energy goes to its maximum value and minimum value at θ = 0deg and maximum value can be written as

$$T_{e,max} = \frac{2E^2_{\gamma^2}}{mc^2 + 2E_\gamma} \tag{3.10}$$

This energy represents the maximum energy of the Compton tail and therefore determines the position of the Compton edge.

3.7.3 Pair Production

The pair production is a types of process in which the total energy of the γ ray is fully absorbed. In this type of interaction, a γ ray enters into the detector material and creates an electron positron pair. From the law of conservation of mass and energy, it is known that the initial γ ray have to have an energy of at least 1.02 MeV because it takes same amount energy to create both an electron and positron. Figure 3.11 illustrates what happens in the detector in the pair-production process. In Figure 3.11, the e^- will produce a pulse whose magnitude is proportional to the energy of (E_{e^-}).

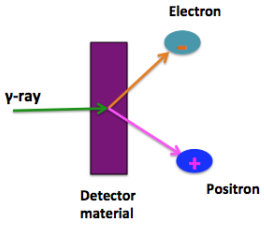

FIGURE 3.11: Pair production through Ge detector

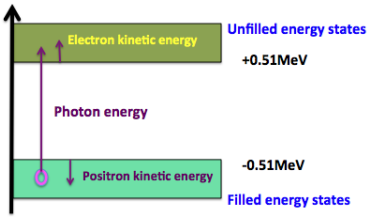

FIGURE 3.12: Pair production

Pair production is almost always followed by the annihilation of the positron e^+, usually leading to emission of the two 0.511 MeV γ rays (shown in Figure 3.12). A single γ is emitted in rare cases where the positron energy is very small so that a neighbouring atom can absorb the available momentum.

3.8 Energy Resolution

The energy resolution of a detector is very important for γ-rays detection experiments. It measures its ability to distinguish γ-rays with close energies. The detector with better energy resolution can successfully separate two adjacent energy peaks and it allows to identify different decays of radionuclides in the γ ray spectrum. The energy resolution of a detector is defined as σ and relative energy resolution can be written as $\frac{\sigma}{E}$. Where σ is the standard deviation parameter of Gaussian equation and E energy of the peak center.

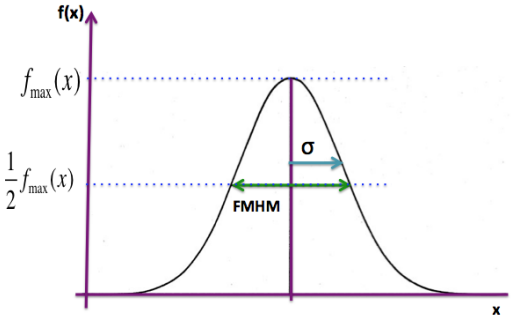

FIGURE 3.13: Sigma of Gaussian

where σ is the standard deviation parameter of a Gaussian (shown in Figure 3.13).
E is the energy of the center or mean of the Gaussian curve.
The Gaussian equation can be written as

$$f(x_i) = \frac{1}{\sqrt{2\pi\sigma}} \exp(-\frac{(x_i - \mu)^2}{2\sigma^2}) \tag{3.11}$$

where σ is related to FWHM (Full Width at Half Maximum) as

$$FWHM = 2\sqrt{2ln2}\sigma = 2.3548\sigma \tag{3.12}$$

3.9 Detection Efficiency

The probability that an emitted γ ray will interact with the detector and produce a count is the efficiency of the detector. High-efficiency detectors produce spectra in less time than low efficiency detectors. In general, large detectors have higher efficiency than smaller detectors, although the shielding properties of the detector material are also important factors. Efficiency, like resolution, can be expressed in absolute or relative terms.

It is convenient to subdivide counting efficiencies into two classes:
(1) Absolute and (2) Intrinsic.

3.9.1 Absolute Efficiency

Absolute efficiencies can be defined as

$$\epsilon_{abs} = \frac{number\ of\ pulses\ recorded}{number\ of\ radiation\ quanta\ emitted\ by\ source} \tag{3.13}$$

and are dependent not only on detector properties but also on the details of the counting geometry (primarily the distance from the source to the detector)

3.9.2 Intrinsic Efficiency

The intrinsic efficiency can be defined as

$$\epsilon_{int} = \frac{number\ of\ pulses\ recorded}{number\ of\ radiation\ quanta\ incident\ on\ detector} \tag{3.14}$$

and no longer includes the solid angle subtended by the detector as an implicit factor. The efficiency, ϵ_{int} depends on the energy of the incident photons:
(i) transmission, (ii) absorption, (iii) full- energy deposition.
The two efficiencies are simply related for isotropic sources by

$$\epsilon_{abs} = \eta \times \epsilon_{int} \tag{3.15}$$

where η is the geometrical efficiency of the detector. The geometrical efficiency depends on the source-detector geometry. It can be written as :

$$\eta = \frac{\Omega}{4\pi} \tag{3.16}$$

where Ω is the solid angle of the detector seen from the actual source position.
Then the relation between intrinsic and absolute efficiency becomes

$$\epsilon_{int} = \frac{\epsilon_{abs}}{\frac{\Omega}{4\pi}} \tag{3.17}$$

Then we can write Eq. 3.16 as

$$\epsilon_{int} = \epsilon_{abs}.(4\pi/\Omega) \tag{3.18}$$

It is much more convenient to tabulate values of intrinsic rather than absolute efficiencies because the geometric dependence is much more milder for the former.

The peak efficiency assume which only those interactions that deposit the full energy of the incident radiation are counted. The total and peak efficiencies can be related by the peak-to-total ratio, r_p

$$r_p = \frac{\epsilon_{peak}}{\epsilon_{total}} \tag{3.19}$$

which is sometimes tabulate separately.

A detector with known efficiency can be used to measure the absolute activity of a radioactive source.

The solid angle is defined by an integral over the detector surface that faces the source [50], of the form

$$\Omega = \int_A \frac{cos\alpha}{r^2} dA \tag{3.20}$$

where r represents the distance between the source and a surface element dA. α is the angle between the normal to the surface element and the source direction (shown in Figure 3.14).
The solid Angle of a circular cross-sectional disk [50] is given by

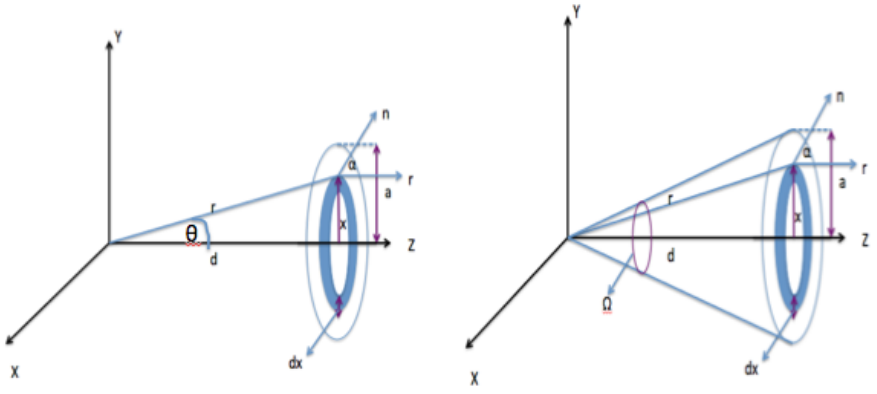

FIGURE 3.14: Solid-angle for a circular disk

Solid angle,

$$\Omega = \int_A \frac{cos\alpha dA}{r^2} = \int_A \frac{\hat{n}.\hat{r}dA}{r^2} \tag{3.21}$$

Here, $cos\alpha = \hat{n}.\hat{r}$.
The normal vector, $\hat{n}$ is given by $\hat{n} = (0\hat{i} + 0\hat{j} + 1\hat{k})$ and radial vector $\hat{r}$ is given by $\hat{r} = (\frac{x}{r}\hat{i} + \frac{y}{r}\hat{j} + \frac{z}{r}\hat{k})$

where $\hat{i}$, $\hat{j}$ and $\hat{k}$ are unit vectors.

$$\begin{aligned} cos\alpha = \hat{n}.\hat{r} &= (0\hat{i} + 0\hat{j} + 1\hat{k}).(\frac{x}{r}\hat{i} + \frac{y}{r}\hat{j} + \frac{z}{r}\hat{k}) \\ &= \frac{z}{r} = cos\theta = \frac{d}{r} \end{aligned} \tag{3.22}$$

Then, the equation (3.21) for the solid angle can be written as,

$$\begin{aligned} \Omega &= \int_A \frac{\hat{n}.\hat{r}dA}{r^2} \\ &= \int_A \frac{(\frac{d}{r})dA}{r^2} = \int_A \frac{ddA}{r^3} \end{aligned} \tag{3.23}$$

The surface element, dA is given for circular disk $dA = 2\pi x dx$ and radial vector, r is given by $r = \sqrt{d^2 + x^2}$

Let, $x^2 = p$, $2xdx = dp$, $x = 0$,then $p = 0$, $x = a$, and, $p = a^2$

Then the solid angle equation become

$$\begin{aligned} \Omega &= \int_0^a \frac{d \times 2\pi x dx}{(d^2 + x^2)^{\frac{3}{2}}} \\ &= 2\pi d \int_0^a \frac{xdx}{(d^2 + x^2)^{\frac{3}{2}}} = \pi d \int_0^a \frac{dp}{(d^2 + p^2)^{\frac{3}{2}}} \end{aligned} \tag{3.24}$$

We know from the integration formula,

$$\int \frac{dx}{(ax + b)^n} = \frac{-1}{a(n-1)} \times \frac{1}{(ax + b)^{n-1}} + c \tag{3.25}$$

By applying this formula in Eq. 3.25, we get

$$\begin{aligned} \Omega &= \pi d[\frac{-1}{1(\frac{3}{2} - 1)(d^2 + p)^{\frac{3}{2}-1}}]_0^{a^2} \\ &= 2\pi d[\frac{-1}{(d^2 + p)^{\frac{1}{2}}}]_0^{a^2} \\ &= 2\pi d[\frac{-1}{(d^2 + a^2)^{\frac{1}{2}}} + \frac{1}{d}] = 2\pi[1 - \frac{d}{\sqrt{d^2 + a^2}}] \end{aligned} \tag{3.26}$$

Ω follows as

$$\Omega = 2\pi(1 - \frac{d}{\sqrt{d^2 + a^2}}) \tag{3.27}$$

where d is the source -detector distance and a is the detector radius. For $d >> a$, the solid angle reduces to the ratio of the detector plane frontal area A visible at the source to square of the distance:

$$\Omega \equiv \frac{A}{d^2} = \frac{\pi a^2}{d^2} \tag{3.28}$$

The solid angle subtended by rectangular surface is given by

$$\Omega = 4sin^{-1}[\frac{ab}{\sqrt{(a^2 + 4d^2)(b^2 + 4d^2)}}] \tag{3.29}$$

Then we can calculate the geometrical efficiency by

$$\eta = \frac{\Omega}{4\pi} \tag{3.30}$$

Chapter 4

Study on the properties of Ge Detector

4.1 Ge Detector Experiment

We carried out an experiment with Ge detector for studying the basic properties of the Ge detector by using the radioactive sources (^{60}Co, ^{22}Na, ^{137}Cs) at Sakuda Laboratory, Okayama University. Figure 4.1 and 4.2 show the experimental set up for Ge detector characteristic experiment.
Properties of the Ge-detector: We have studied three different properties of Ge detector: (1) High voltage experiment (voltage dependency of peaks position). (2) Photo-peak efficiency. (3) Energy resolution.

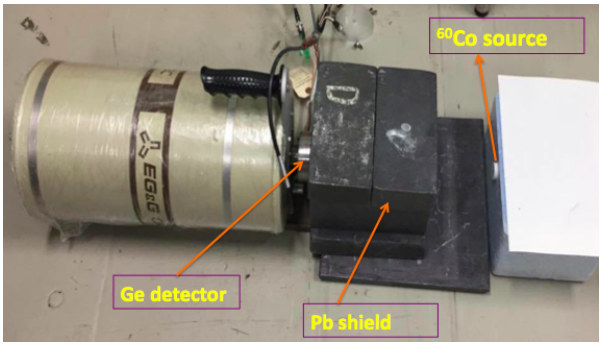

FIGURE 4.1: Experimental set up of Ge detector

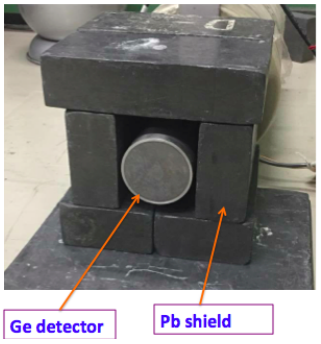

FIGURE 4.2: Experimental set up of Ge detector

4.1.1 Using ^{60}Co Source

The γ source (^{60}Co) was placed $115mm$ away from surface of the Ge detector. The γ rays from the ^{60}Co source was detected at different voltages. The high-voltage experiment were performed using different voltages. We carried the experiment for the voltages of 500 V, 700 V, 900 V, 1100 V, 1300 V and 1500 V. Figure 4.3 shows the comparison of the energy spectrum of ^{60}Co source and the background energy spectrum. Figure 4.4 shows the background subtracted energy spectrum for 1100 V voltage of ^{60}Co source.

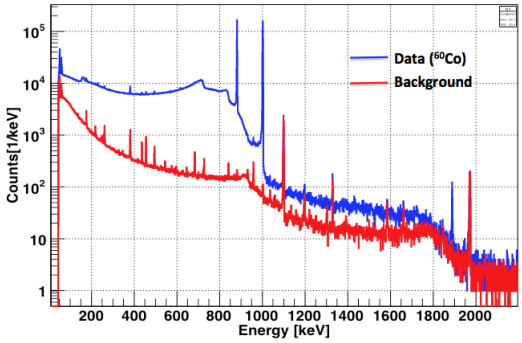

FIGURE 4.3: γ spectrum of ^{60}Co source at 1100V

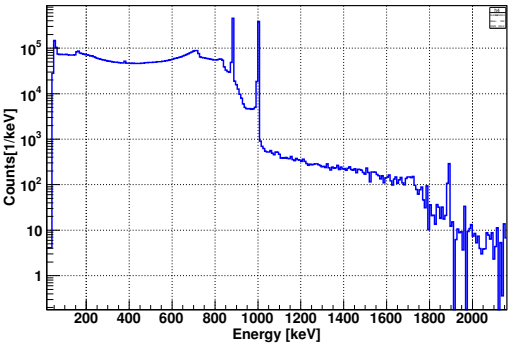

FIGURE 4.4: γ spectrum of ^{60}Co source at 1100V

Then, we calculated the peaks position in channel (ch) for different voltages. Then the peak position (ch) was plotted for different Voltages. Figure 4.5 shows that the variation of the channel (ch) with voltages. We found that the as the voltage increase the peak position (ch) also increase because as we have increased the voltages, the flow of electron-hole also have increased.

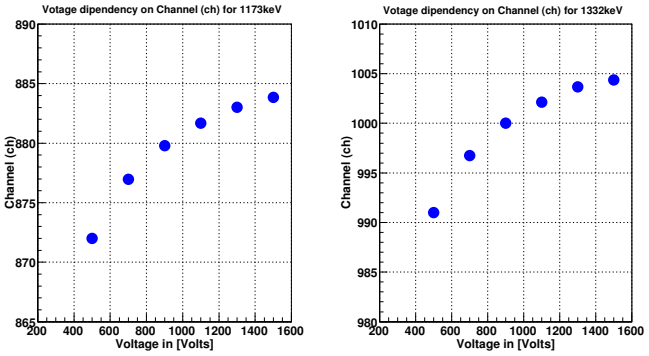

FIGURE 4.5: Variation of channel(ch) with Voltages of Ge detector

Measurement of photo-peak efficiency:

^{60}Co- source emit two γ which are 1173keV and 1332keV. And their coincidence $\gamma$is at 2505 keV. We consider N1, N2 and N3 are the number of events of the respectively energy 1173keV, 1332keV and 2505keV. N1, N2 and N3 can be written as

$$N_1 = \beta T_L \eta \epsilon_1 (1 - C) \tag{4.1}$$

$$N_2 = \beta T_L \eta \epsilon_2 (1 - C) \tag{4.2}$$

$$N_3 = \beta T_L \eta \epsilon_1 \eta \epsilon_2 \tag{4.3}$$

where β is Source activity, T_L is the true measurement time and T_L=r_LT, where T is the running time and r_L is the dead time correction factor, η= acceptance or geometric efficiency, $\eta\epsilon_1$= efficiency of γ_1 (1173keV), $\eta\epsilon_2$= efficiency of γ_2 (1332keV), C=Compton correction

Dead time of this experiment was about 3%. So the correction factor, r_L=0.97.

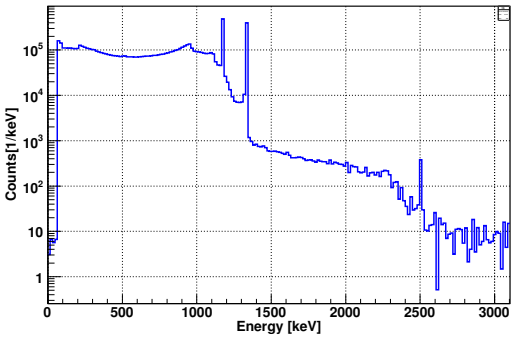

FIGURE 4.6: γ spectrum of ^{60}Co source

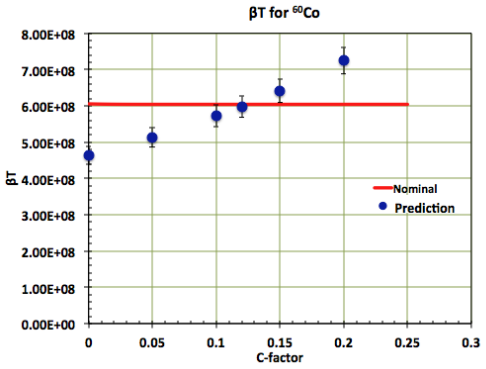

FIGURE 4.7: Measurement of C-value

Let, a=βT, b=$\eta\epsilon_1$, e=$\eta\epsilon_2$, then from χ^2-formula we get,

$$\chi^2 = (\frac{N_1 - ab(1-C)}{\sigma_1})^2 + (\frac{N_2 - ae(1-C)}{\sigma_2})^2 + (\frac{N_3 - abe}{\sigma_3})^2 \tag{4.4}$$

Figure 4.6 shows the γ ray spectrum of ^{60}Co source. We have measured βT value for different C (shown in Figure 4.7) using Eq. 4.4. We found at C=0.12, the predicted and nominal value of βT agrees well and hence we choose that value as C value. The photo-peak efficiencies of γ_1 (1173keV) and γ_2 (1332keV) was calculated by using Eq. 4.4 by putting C=0.12. We obtained photo-peak efficiency $\eta\epsilon_1$=9.05$\pm$0.45E-04 for 1.173 MeV energy γ ray (shown in figure 4.10) and activity, β=2.93$\pm$0.14E+04 Bq (Nominal activity, β=3.10$\pm$0.05E+04 Bq)

4.1.2 Using ^{137}Cs Source

The decay scheme of ^{137}Cs source is given below. The total branching ratio for decaying γ-ray from ^{137}Cs is about 85.1% (shown in Figure 4.8). Figure 4.9 shows the γ spectrum of ^{137}Cs source. The

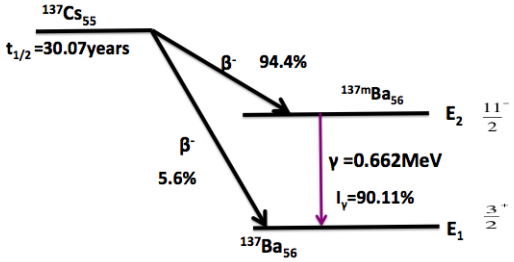

FIGURE 4.8: Decay scheme of ^{137}Cs source

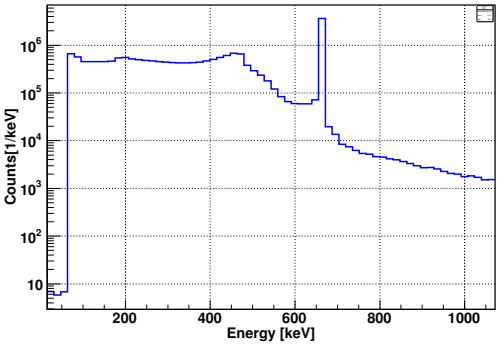

FIGURE 4.9: γ spectrum of ^{137}Cs source

number of events N_i can be written as

$$N_i = 0.851 \times \beta T_L \eta\epsilon \tag{4.5}$$

where, β=activity for ^{137}Cs source, $\eta\epsilon$=photo-peak efficiency, T_L=live time or true measurement time , Live time, $T_L = r_L T$ where, T=is the measurement time, r_L=dead time correction factor=0.94 (as dead time is 6%). Then efficiency can be written as

$$\eta\epsilon = \frac{N_i}{0.851 \times \beta T_L} \tag{4.6}$$

We obtained the photo-peak efficiency $\eta\epsilon$=1.50$\pm$0.005E-03 for 6.62 MeV γ ray (shown in figure 4.10) and activity, β=1.10E+05 Bq (Nominal activity, β=1.63E+05) for MC (Geant4) efficiency, $\eta\epsilon$=1.95E-03.

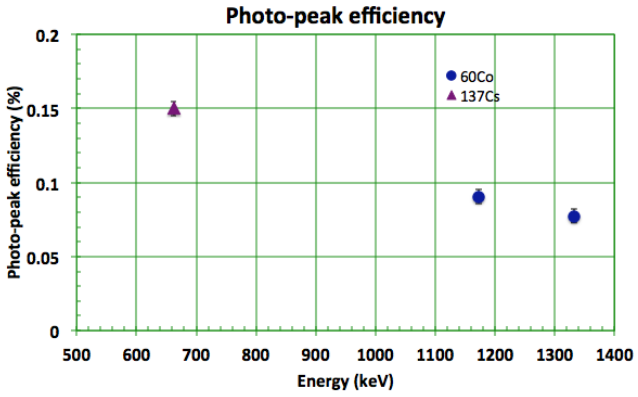

FIGURE 4.10: Comparison of the Efficiency of ^{60}Co and ^{137}Cs

4.2 Geant4 (MC) Simulation for HPGe-Detector

Geant4 (for GEometry ANd Tracking) [52, 53] is a platform for "the simulation of the passage of particles through matter," using Monte Carlo methods. We generated the MC by reproducing the size and shape of the detector appropriately. Figure 4.11 shows the block diagram of Ge-detector.

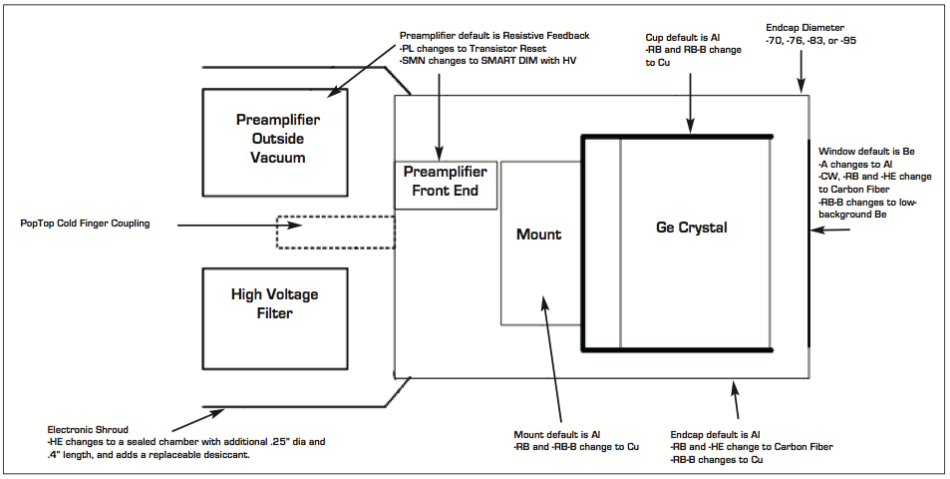

FIGURE 4.11: Block diagram of Ge-detector [51]

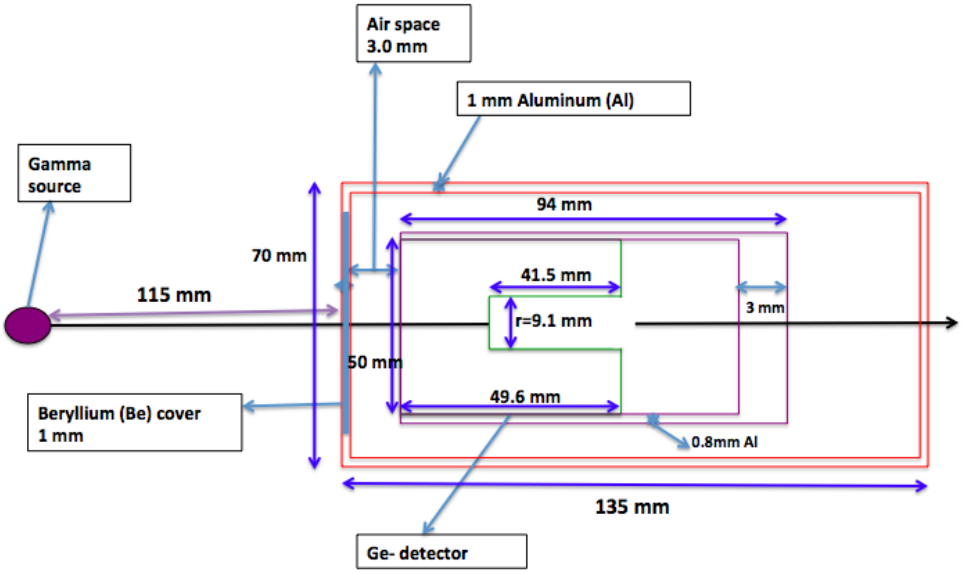

FIGURE 4.12: Block diagram of real size of Ge-detector

Figure 4.12 shows the block diagram of real size of the Ge detector. The detector is cylindrical with co-axial is circular. The length of detector 135mm and diameter is 70mm. The thickness of aluminum cover is 1mm with length 135mm and 70mm diameter. The Ge-detector with 50mm diameter and 49.6mm length inside the air space. Their is 0.5mm Be- cover in front of the Ge detector. In Ge-detector, their is electrode hole right side of the Ge-detector. The hole with 9.1mm diameter and 41.3mm length.

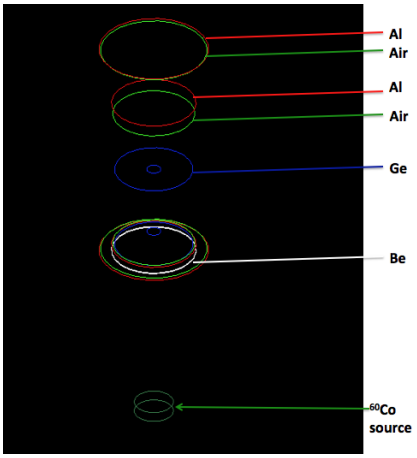

FIGURE 4.13: Block diagram of Ge-detector in Geant4(MC)

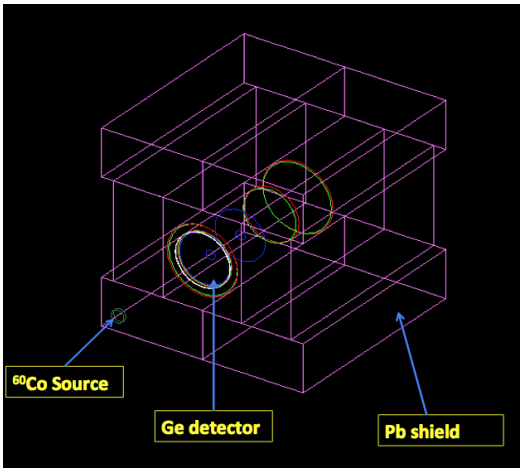

FIGURE 4.14: Ge-detector in Geant4(MC)

The γ source is 115 mm far from the Ge-detector. The uniform γ rays was produced from the beam of different energy. We generated the γ rays with of any energy. Figure 4.13 and Figure 4.14 show that the block diagram of Ge detector in MC(Geant4). We have generated γ rays of any energy. Figure 4.15 shows the energy spectrum of γ ray spectrum for MC(Geant4).

MC detector efficiency

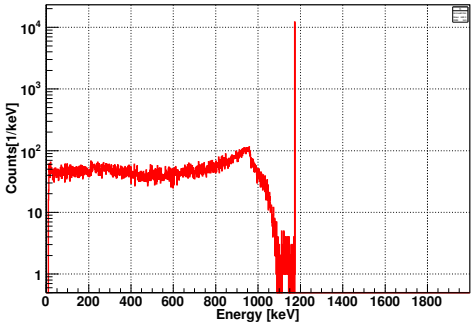

FIGURE 4.15: 1173keV energy spectrum for Geant4(MC)

For each energy γ ray we have total number of γ rays and the number of gamma rays detected by the Ge-detector. The number of detected γ rays by the Ge detector out of the total number of γ rays generated by the γ source is called the detector efficiency.

$$efficiency, \epsilon_{MC} = \frac{N_c}{N_s} \times 100\% \tag{4.7}$$

Where N_c is the number of γ rays detected by the Ge detector.
N_s is the total number of γ rays generated.
The MC (Geant4) photo-peak efficiency for energy 662 keV, 1173keV and 1332keV were measured and compared with the photo-peak efficiency of ^{137}Cs and ^{60}Co data.

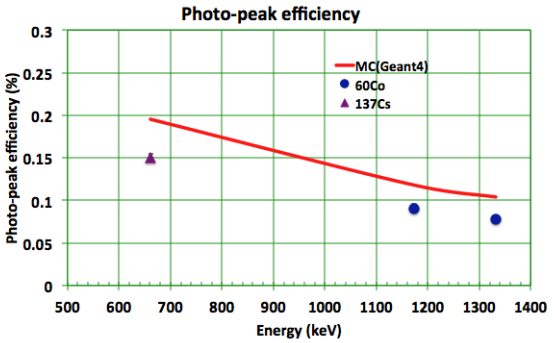

FIGURE 4.16: Comparison of the Efficiency of ^{60}Co,^{22}Na and Geant4(MC)

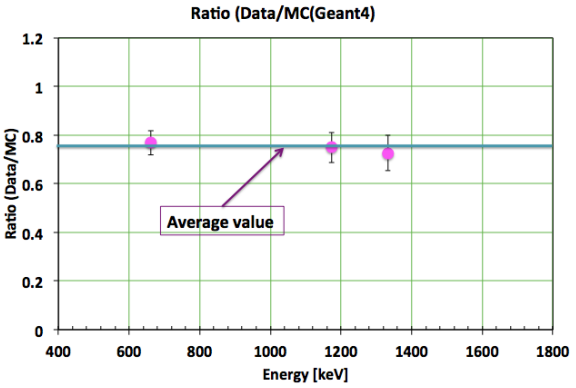

FIGURE 4.17: Ratio (Data/MC) for ^{137}Cs and ^{60}Co

Figure 4.16 shows that the comparison of the photo-peak efficiency of ^{137}Cs and ^{60}Co with the Geant4 (MC) photo-peak efficiency. Our data and MC (Geant4) agrees well. Figure 4.17 shows the ratio between data and MC(Geant4) efficiency for ^{137}Cs and ^{60}Co. The agreement between data and MC(Geant4) is about 75% (shown in Figure 4.17).

4.2.1 Generation of One and Two γ Rays in MC(Geant4)

From the above experiment, we know that we have understood the Ge-detector very well as we have generated the MC (Geant4) [52, 53]. Then we have generated two γ ray sources ^{137}Cs and ^{60}Co using Geant4. Figure 4.18 shows the comparison between data and MC(Geant4) for ^{60}Co. Figure 4.20 shows that the comparison between data and MC(Geant4) for ^{137}Cs. Then the photo-peaks efficiency of MC (Geant4) for ^{137}Cs and ^{60}Co were calculated. Then we have compared this MC(Geant4) photo-peak efficiency with our data. Our data agrees with MC(Geant4) well for both ^{137}Cs and ^{60}Co (shown in Figures 4.19 and 4.21). The agreement between data and MC(Geant4) is about 75%. From this result we can conclude that in reality there is no perfect detector.

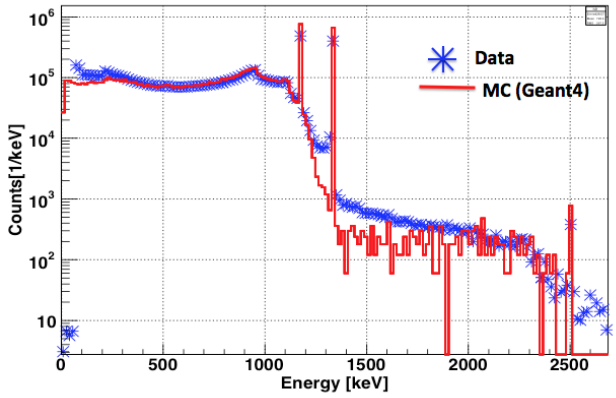

FIGURE 4.18: Comparison of data and MC of ^{60}Co

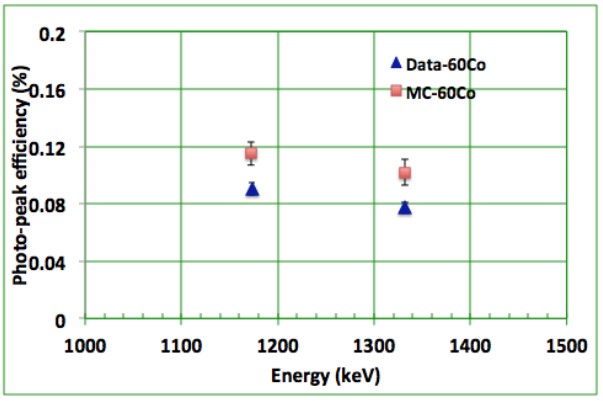

FIGURE 4.19: Comparison efficiency of data and MC of ^{60}Co

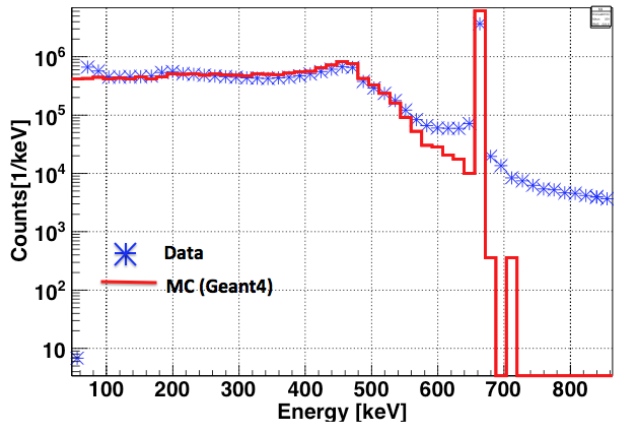

FIGURE 4.20: Comparison of data and MC of ^{137}Cs

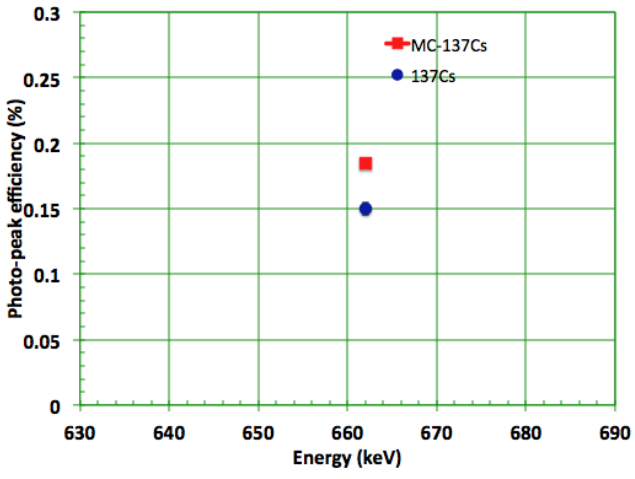

FIGURE 4.21: Comparison efficiency of data and MC of ^{137}Cs

4.2.2 Energy Resolution of Ge Detector

The HPGe detector was used here. The Ge detector has good energy resolution. Hero we have calculated the energy resolution from the ^{22}Na, ^{60}Co and ^{137}Cs γ ray sources.
We know, Energy resolution is σ and relative resolution is $\frac{\sigma}{E}$.

The energy resolution was calculated from the photo-peaks 511keV and 1275keV from ^{22}Na. and 1173keV photo-peaks and 1332keV from ^{60}Co and 662 keV photo-peaks for ^{137}Cs.

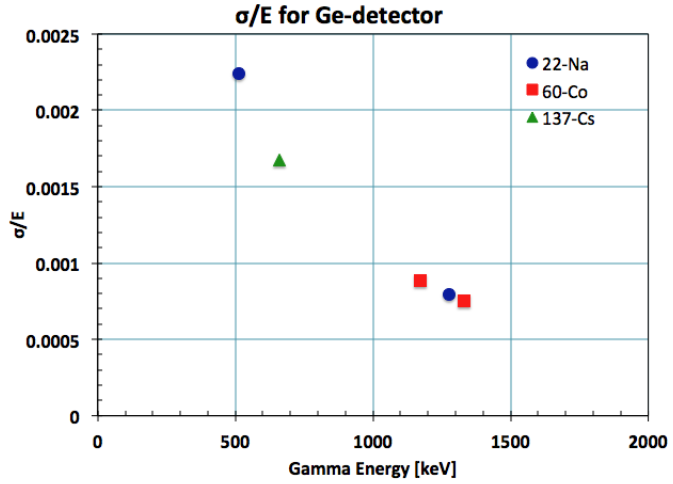

FIGURE 4.22: $\frac{\sigma}{E}$ of ^{22}Na and ^{60}Co

Figure 4.22 shows that the energy resolution for Ge detector. Theory of energy resolution also tells that resolution of the detector depends on energy. From Figure 4.22, we can found that the resolution of the Ge detector is very good as it can differentiate the nearby photo-peaks very well.

Chapter 5

JPARC, MLF and ANNRI

5.1 JPARC

JPARC stands for Japan Proton Accelerator Research Complex [54]. It has a series of world class proton accelerators and experiments facility. All the experimental facilities use high intensity proton beams. It is open to users from all over the world. Figure 5.1 shows the side view of JPARC center.

It is a multi-purpose and multidisciplinary facility. It is unique in the variety of secondary-

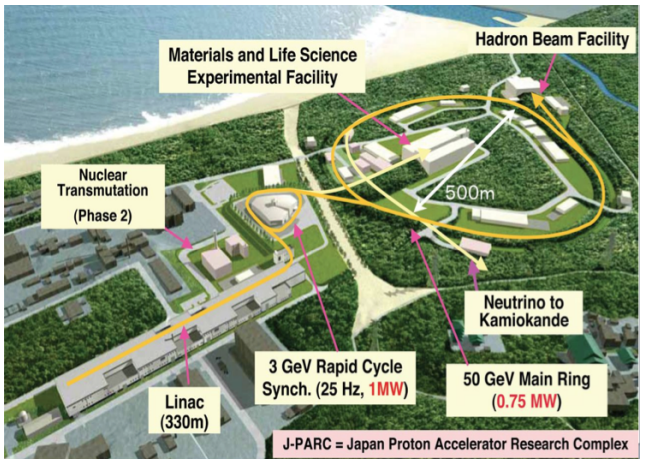

FIGURE 5.1: J-PARC Center [54]

particle beams produced allowed to use across a wide range of scientific fields [55]. Form the collisions between the proton beams and target material with the help of spallation reaction, it can produce neutron, pion, kaon and neutrino beams. The beams can be used various fields in physics including fundamental nuclear particle physics, material and life science and nuclear technology. JPARC has intensity of the secondary particle beam which make it special.

The high intensity makes possible many impossible works and it unfolds the door for new and exciting research facilities. There are three proton accelerators in JPARC. Those are (i) 400 MeV linear

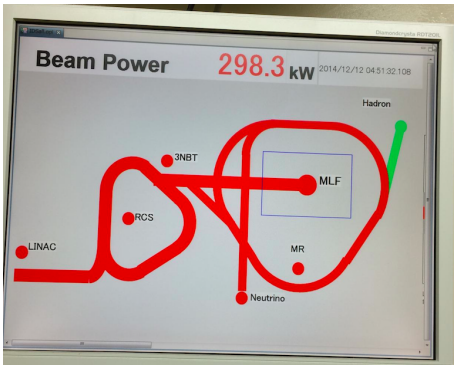

FIGURE 5.2: Beam power of JPARC

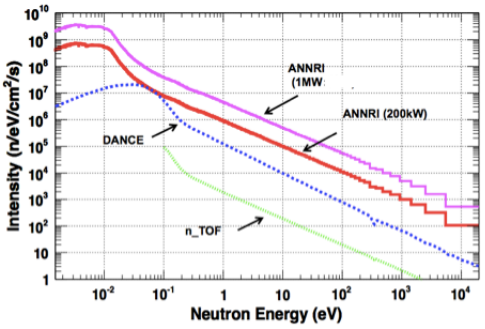

FIGURE 5.3: Comparison of neutron flux [56]

accelerator (ii) 3 GeV rapid-cycling synchrotron (RCS) and (iii) 50 GeV (currently 30 GeV) main ring. The efficient production of the desired secondary particle beam is maximized due the target matter and designs.

JPARC has most the intense pulse neutron in the world. We can compare the neutron flux of JPARC with DANCE, n_TOF (CERN) [55]. Figure 5.2 shows the proton beam power in december, 2014. Figure 5.3 shows that the coparison between the neutron flux of ANNRI, DANCE, n_TOF (CERN) [56]. Over 90% of the proton beams, accelerated in the RCS, are directed to the muon and neutron production targets of the Materials and Life Science Experimental Facility (MLF). The rest of the protons are transported to the main ring (MR) for further acceleration before being extracted in one of two MR extraction ports.

The high energy proton are directed to the Hadron Experimental Facility where a variety of nuclear physics experiments are carried out using k-mesons with the help of slow extraction (SX) ports. The fast extraction protons are guided by superconducting magnetic array towards the pion production target. Neutrinos are generated through pion decay. The neutrinos are sent as part of T2K experiment to Super-Kamiokande.

5.2 Materials and Life Science Experimental Facility(MLF)

JPARC has many facilities. Material and Life Science Facility (MLF)[57] is one of them. It is available to Japanese and foreign users, for both academic research and industrial applications. This facility has 23 neutron beam extraction ports for the pulsed spallation neutron source and it has also four muon extraction channels for the muon target [55]. Japan Atomic Energy Agency (JAEA) and Hight Energy Accelerator Organization known as KEK are the parent organizations of JPARC. They construct the instruments for conducting experiments using the neutron and the muon beams. Instruments may also be constructed by a third party organization with the approval of the Neutron/Muon Instrument Review Committee. At MLF, the third party organizations are responsible for the management and maintain and maintain their beamline instruments. Figure 5.4 shows the schematic view of MLF facilities and Figure 5.5 shows the neutron beam line of MLF.

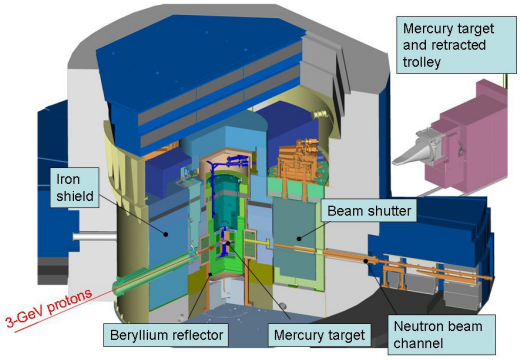

FIGURE 5.4: Schematic view of MLF facilities [58]

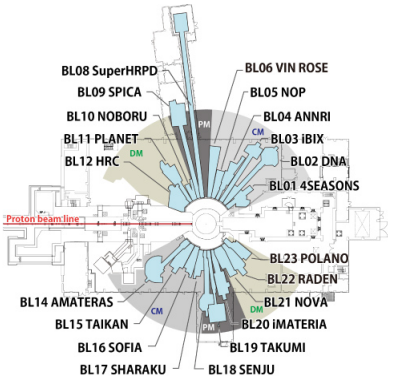

FIGURE 5.5: Neutron beam line of MLF [55]

5.3 ANNRI(Accurate Neutron-Nucleus Reaction Measurement Instrument)

ANNRI stands for Accurate Neutron-Nucleus Reaction Measurement Instruments. It is an instrument built to measure the neutron-capture cross-sections with high-intensity pulsed neutrons from the No. 04 beam port in the MLF [59, 60]. In MLF facility, the proton beam pulses are supplied by the 3-GeV Rapid-Cycling Synchrotron of JPARC [55]. This proton beams are usually supplied at a repetition

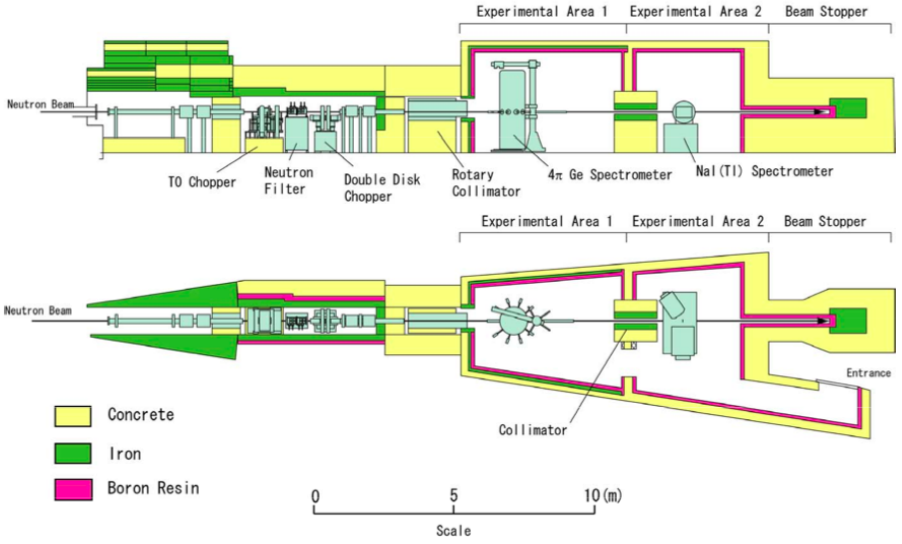

FIGURE 5.6: A side view of ANNRI instrument [56]

rate of 25 Hz and in the double-bunch mode, in which the pulsed protons consist of two bunches, each with a width of 100 ns, at intervals of 600 ns [61] (shown in Figure 5.7). Figure 5.6 shows the diagram of a side view of ANNRI instruments

ANNRI usually uses neutrons from a coupled moderator (140-mm diameter and 120-mm height) which provides the most intense neutron beam among the moderators at the Japan Spallation Neutron Source (JSNS) [61]. The neutron beam goes to the sample position through the collimator and a beam duct. There are two sample positions in the ANNRI, one of them is used for measurements of γ-rays

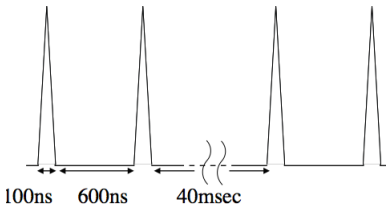

FIGURE 5.7: Double -bunch mode

with the array of large Ge detectors. This sample position is located 21.5 m from the center of the moderator. The neutron beams can be collimated by a collimator with diameters of 3, 7, 15, and 22 mm.

Figure 5.8 shows the ANNRI spectrometer overview. The array of Ge detectors is consited of

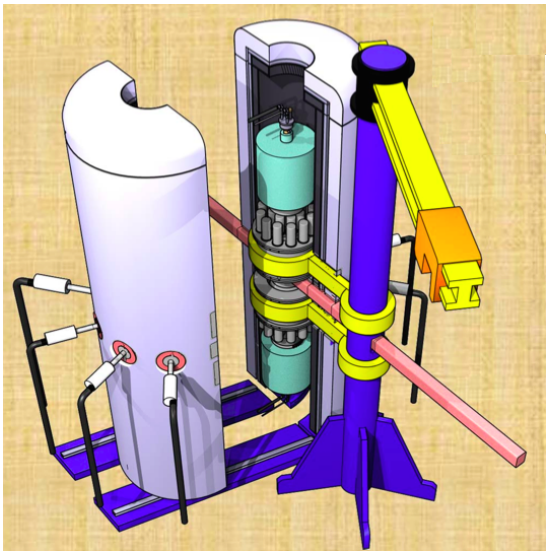

FIGURE 5.8: ANNRI spectrometer overview [62]

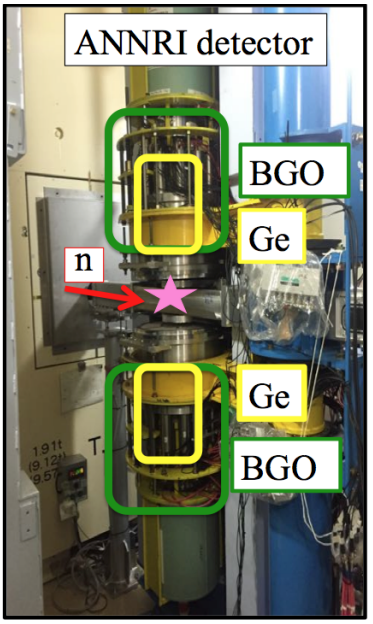

FIGURE 5.9: ANNRI spectrometer

two cluster-Ge detectors, eight coaxial-Ge detectors and anti-coincidence shields (BGO) around each Ge detector as seen in Figure 5.9. Each cluster-Ge detector consists of seven Ge crystals [63]. The positions of the cluster-Ge detectors were arranged so that the distance between the front surface of each detector and the center of the sample position was 125 mm. The proton beam bombards the Hg target in the MLF resulting the pulsed neutrons produced through the spallation reaction are supplied as the neutron source for each beam line. There is a moderator made of H-rich material for thermalizeing the neutron energy. Table 5.1 shows the specification of Ge spectrometer.

TABLE 5.1: Specification of all solid angle Ge spectrometer

Detection efficiency of the entire detector	2.20 % (at E_γ=1.3 MEV)
Energy resolution of γ-rays	9.18 keV (FWHM at E_γ=1.3 MEV)
Constitution of whole detector	Upper and Lower cluster of Ge detectors and 8 co-axial Ge detectors
Configuration of cluster of Ge detector	7 Ge crystals
Compton suppress	BGO scintillator

5.3.1 Block-Diagram of ANNRI Detector

We have made a block diagram to explain the upper cluster and beam line of the ANNRI detector. The shape and size of a single Ge detector is shown in the block diagram below. All the units shown in Figure 5.10 and Figure 5.11 are in mm.

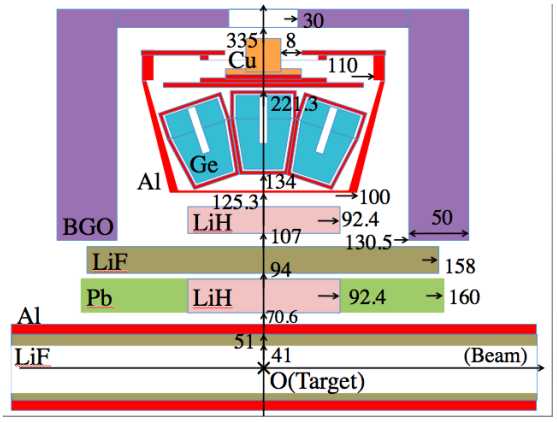

FIGURE 5.10: Block diagram of ANNRI detector (Units are in mm)

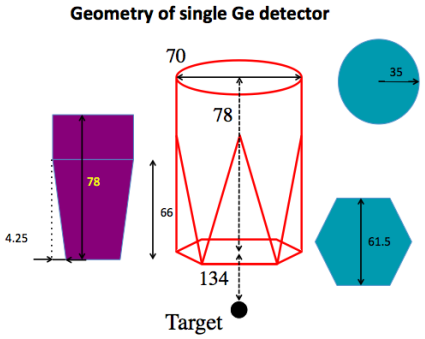

FIGURE 5.11: Block diagram of single Ge detector of ANNRI (Unit are in mm)

Figure 5.12 shows the block diagram of the target holder and all the unit shown here are in mm. Figure 5.13 shows the upper cluster of ANNRI detector where the numbers 1-7 indicate the number of the crystal.

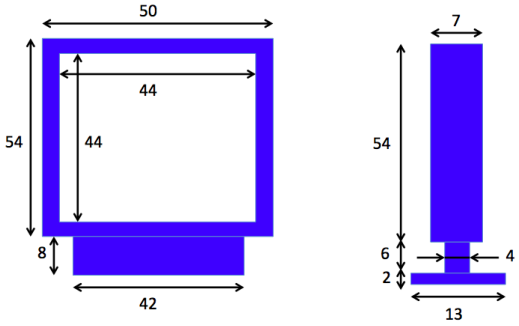

FIGURE 5.12: Block diagram of target holder (Unit are in mm)

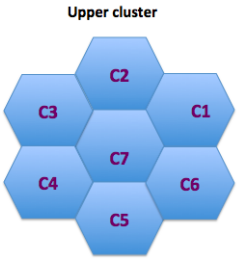

FIGURE 5.13: Upper cluster of ANNRI detector

5.3.2 Angle Between the Ge Detector

The co-ordinates of the center of all the Ge detectors were calculated. Then, the unit vectors of all the detectors passing through the center were calculated. Suppose, the radial vector from (0,0,0) position(target position consider to be at center (0 mm, 0 mm, 0 mm)) to center of crystal, C1(53.25 mm, 30.75 mm, 134 mm) be $\vec{r_1}$ and can be written as

$$\vec{r_1} = 53.25\hat{i} + 30.75\hat{j} + 134\hat{k} \tag{5.1}$$

Then, the unit vector of C1 can be written as $\hat{n_1} = 0.3612\hat{i} + 0.2086\hat{j} + 0.9088\hat{k}$. Similarly the unit vector of C7(0 mm, 0 mm, 134 mm) is $\hat{n_7} = 1\hat{k}$.

Then, the angle between C1 and C7 detector is given by

$$cos\theta_{17} = \hat{n_1}.\hat{n_7} = 0.9088 \tag{5.2}$$

where θ_{17} is the angle between the detector 1 and detector 2. Then angle we get, $\theta_{17} = 24.67\,\mathrm{deg} \approx 24.7\,\mathrm{deg}$.

Similarly, the angle between all the pair of detectors were calculated.

Figure 5.14 shows the block diagram of ANNRI detector (both the cluster) with beam direction. The

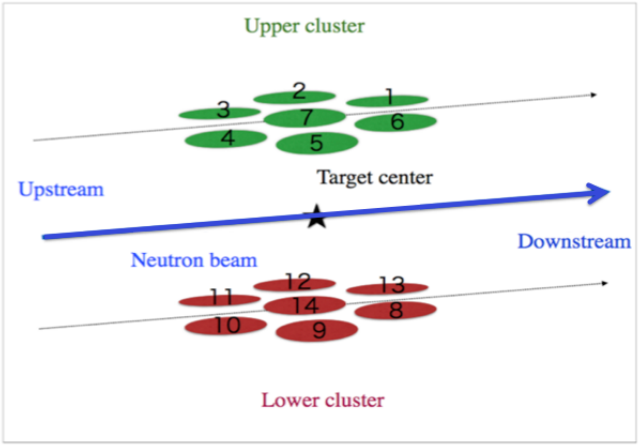

FIGURE 5.14: Upper and lower cluster of ANNRI

co-ordinates of all 14 Ge crystals are given below:

C1(x,y,z)=(53.25, 30.75, 134)

C2(x,y,z)=(0.0, 61.5, 134)

C3(x,y,z)=(-53.25, 30.75, 134)

C4(x,y,z)=(-53.25, -30,134)

C5(x,y,z)=(0.0, -61.5, 134)

C6(x,y,z)=(53.25, -30.75, 134)

C7(x,y,z)=(0.0, 0.0, 134)

C8(x,y,z)=(53.25,-30.75,-134)

C9(x,y,z)=(0.0, -61.5, -134)

C10(x,y,z)=(-53.25, -30.75, -134)

C11(x,y,z)=(-53.25, 30.75, -134)

C12(x,y,z)=(0.0, 61.75, -134)

C13(x,y,z)=(53.25, 30.75,-134)

C14(x,y,z)=(0.0, 0.0, -134)

All the units are in mm.

The angle for all the pairs between all the detectors are calculated and listed in Appendix A.5.

Chapter 6

Experimental Techniques and Data Processing

6.1 Experimental Techniques of ANNRI detector

The experiment (2014B0124) was conducted in December, 2014, using ANNRI detector at the beamline No.4 (BL04) in JPARC-MLF. Another experiment was carried out in December, 2015 without neutron beam for position dependency calculation. In this chapter, we have described the experimental conditions of the neutron beam and the detector, which are specific to this experiment.

6.1.1 Samples

In this experiment, enriched gadolinium oxide ($^{155,157}Gd_2O_3$) was used as a target. Natural gadolinium consists of six stable isotopes, ^{154}Gd (2.18%), ^{155}Gd (14.8%), ^{156}Gd (20.5%), ^{157}Gd (15.7%), ^{158}Gd (24.8%) and ^{160}Gd (21.9%) and one radioisotope ^{152}Gd (0.2%) with half-life of $1.1\times10^4 y$. Since Gd has a large thermal neutron capture cross-section, γ rays are emitted at high rate during the experiment. So, the measurements were carried out with two types of collimators, 15 mmϕ and 6 mmϕ.

The ^{155}Gd sample for γ-ray measurements contained 100 mg of gadolinium oxide ($^{155}Gd_2O_3$) powder. Table 6.1 shows that the isotopic composition of ^{155}Gd target.

TABLE 6.1: Isotopic composition of the targets

Matter	Isotopic composition (%)						
Isotope	^{152}Gd	^{154}Gd	^{155}Gd	^{156}Gd	^{157}Gd	^{158}Gd	^{160}Gd
^{155}Gd	<0.02	0.50	91.90($\pm$0.3)	5.87	0.81	0.65	0.27

Chemical admixtures of $^{155}Gd_2O_3$ are given below

TABLE 6.2: Chemical admixtures of the targets.

	Chemical admixtures (ppm)									
Element	K	Na	Ca	Mg	Fe	Al	Si	Ni	Cu	Pb
Content (ppm)	<30	<30	< 40	<5	<40	<10	<90	<50	<5	60
Element	Sn	Dy	Sm	Yb	Nd	Er	Eu	Cr		
Content (ppm)	<10	100	< 1500	200	<150	<50	<50	<10		

The ^{157}Gd sample contained 100 mg of Gadolinium oxide ($^{157}Gd_2O_3$) powder. Table 6.3 shows that the isotopic composition of ^{157}Gd target.

TABLE 6.3: Isotopic composition of the targets

Matter	Isotopic composition (%)						
Isotope	^{152}Gd	^{154}Gd	^{155}Gd	^{156}Gd	^{157}Gd	^{158}Gd	^{160}Gd
^{157}Gd	<0.01	0.05	0.30	1.63	88.4(±0.2)	9.02	0.60

Chemical admixtures of $^{157}Gd_2O_3$ are given below

TABLE 6.4: Chemical admixtures of the targets.

	Chemical admixtures (%)									
Element	K	Na	Ca	Mg	Fe	Al	Si	Cr	Ni	Cu
Content (%)	0.005	0.015	< 0.004	<0.0005	<0.004	<0.001	<0.005	<0.003	0.007	<0.0005
Element	Pb	Sn	Er	Eu	Sm	Nd	Dy	Tb		
Content (%)	0.011	<0.003	0.044	0.008	0.042	<0.01	0.024	0.05		

Table 6.2 and Table 6.4 show the chemical admixtures for ^{155}Gd and ^{157}Gd respectively. These values were measured by ISOFLEX [64], the supplier of concentrated Gd. The concentrate of Gd contains some impurities and other isotopes, but it can be ignored because of their having very small thermal neutron capture cross-section compared with ^{155}Gd and ^{157}Gd.

Calibration source:

We have used ^{22}Na,^{60}Co , ^{137}Cs, ^{152}Eu and NaCl as a calibration source.
The activity of the radioactive sources are shown in the Table 6.5.

TABLE 6.5: Radioactive activity of the radioactive calibration sources

Radioactive source	^{22}Na	^{60}Co	^{137}Cs	^{152}Eu
Half life	30.07 y	5.271 y	13.542 y	2.602 y
Creation date	2009/01/23	2009/01/23	2006/09/27	2011/02/14
Initial activity	8.50 $\times 10^3$ Bq	10.50 $\times 10^3$ Bq	3.77 $\times 10^3$ Bq	845 $\times 10^3$ Bq

γ rays emitted from the thermal neutron capture ^{35}Cl(n,γ) reaction have been investigated well for both energy and intensity. We used NaCl as a target for ^{35}Cl(n,γ) reaction. In a single crystal of

NaCl, the material composition ratios are ^{23}Na:^{35}Cl:^{37}Cl=100:76:24. Furthermore, the thermal neutron capture cross-section of ^{23}Na and ^{37}Cl is 0.53 barns and 0.43 barns, while the thermal neutron capture cross-section of ^{35}Cl is 44 barns. Therefore, when thermal neutrons incident on NaCl, ^{35}Cl reacts with a probability of about 98%. That is why, a single crystal of natural NaCl can be regarded as a ^{35}Cl. The characteristic of calibration sources are shown in Table 6.6

TABLE 6.6: Characteristics of the radioactive calibration sources

Sample	Characteristics
^{137}Cs	Emit one γ ray of 0.662 MeV
^{60}Co	Emits two γ-ray of 1.17 MeV and 1.33 MeV
^{22}Na	Two γ-rays of 0.511 MeV and one γ-ray of 1.275 MeV are emitted.
^{152}Eu	Emits multiple γ-rays from 0.1 to 2 MeV
NaCl	Emits multiple γ-rays from 1 to 8 MeV

6.1.2 Measurement Condition

In the measurements, we have used two cluster-Ge detectors and used just one coaxial-Ge detector. The total measuring time with the ANNRI was about 48 h for the ^{157}Gd sample and about 44 h for the ^{155}Gd sample. For the background estimation, γ-ray measurements with an empty target holder only for about 5.5 h. Table 6.7 shows that the total measuring time of all the samples.

TABLE 6.7: Data information

Data sample	Measuring time	Number of Events
^{155}Gd (Enriched)	48 hours	1.71×10^{9}
^{157}Gd (Enriched)	44 hours	1.81×10^{9}
NaCl	4 hours	1.3×10^{8}
^{22}Na	5 minutes	1.5×10^{7}
^{60}Co	18 hours	8.8×10^{7}
^{137}Cs	30 minutes	2.1×10^{6}
^{152}Eu	7 hours	2.3×10^{7}
Empty(only target holder)	5.5 hours	1.3×10^{7}

For position dependency, the measurements were also done using two cluster detector. We have taken our measurements for different source position for about 15 minutes. We've taken data for center (0,0,0), upper side (2.5mm and 5mm from center), lower side (2.5mm and 5mm from the center), left side (2.5mm and 5mm from the center), right side (2.5mm and 5mm from the center), upstream (7.2mm from center) and downstream (7.2mm from center).

6.1.3 Data Acquisition System

Data Acquisition System (DAQ) have to handle many signals from Ge and BGO detectors at high event rate. The DAQ is required to have high time resolution and high speed. At the same time, the DAQ

is also required to have reasonable energy resolution at wide range for analyses of discrete gamma rays and to effectively apply energy gates on them. Figure 6.1 shows the block diagram of data acquisition system.

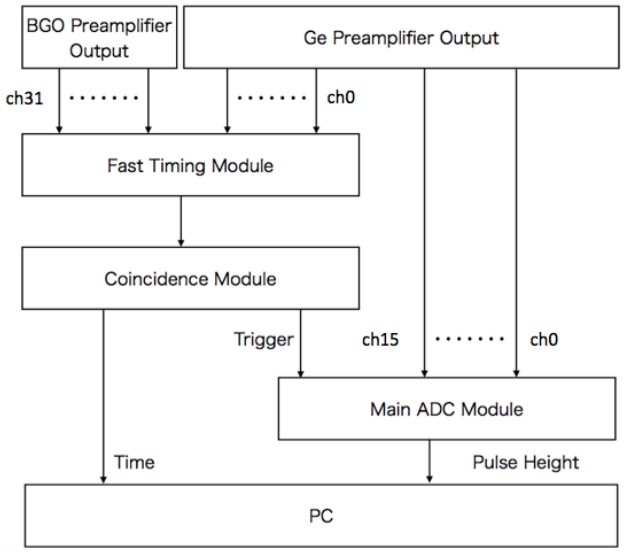

FIGURE 6.1: Data acquisition system

The data acquisition system is triggered only when at least one of the 14 Ge crystals has a pulse height greater than 100 keV and no surrounding BGO counters whose energy are greater than 100 keV are hit. For each trigger, the time-of-flight (T) of a neutron over the distance (L = 21.5 m) between the spallation target (of the neutron source) and the first hit Ge crystal, and the pulse amplitude and the time interval between the trigger time (T) and each crystal (14 in total) are stored in the disk. The system consists of Main ADC modules, Fast Timing modules and a Coincidence module (shown in Figure 6.2). The preamplifier outputs of the Ge detectors are directly put into the Main ADC modules and the Fast Timing Modules. The outputs of BGO anti-Compton detectors are only put into the Fast Timing Modules.

The Fast Timing Module discriminates detector signals and send them to the Coincidence module. The Coincidence Module checks anti-coincidence of these signals and generates a trigger signal to the Main ADC Modules. On the Main ADC modules, when a trigger signal comes, the pulse height is analyzed by fitting or filtering digitized data. All modules are 9U VME boards and can be mounted in a 19 inches VME sub-rack.

6.1.3.1 Fast Timing Module

Fast timing module has 32 input channel (32ch). On the Fast Timing module, input signals (both Ge detector and BGO) are shaped with a differentiation circuit, a pole-zero cancellation circuit, and amplification circuits. The shaped input signals become LVDS output signals with a Constant- Fraction Discriminator (CFD). The output LVDS signals of CFDs are input to the Coincidence Module.

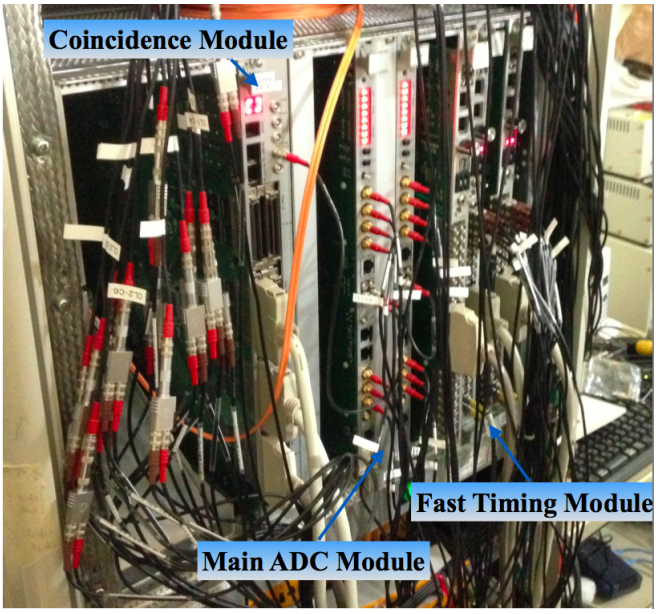

FIGURE 6.2: Data acquisition system

6.1.3.2 Coincidence Module

On the Coincidence Module, Field Programmable Gate Array (FPGA) compares the preset coincidence condition to trigger patterns. If the coincidence pattern met the trigger patterns, the Coincidence Module sends a trigger signal to the Main ADC modules. Because the program of the FPGA (Field Programmable Array) can be uploaded via VME-bus, the coincident condition can be freely changed to suit trigger conditions. Trigger time constantly give 200ch which we should transfer ch to ns (nano sec). (1ch =10ns). Then the formula for transformation ch to ns is $(T_i - 200) \times 10ns$. Coincidence module can record time difference. Time difference can be written as T_i. T_i be the time difference between the trigger time and signal time of each Ge crystal. Coincidence module can also record TOF. In TOF (Time of Flight) experiments, the Coincidence Module also measure and stores the delay time of the event from the start signal of neutron emission. We can measure the time with a resolution of 5 ns ranging up to 84 ms.

6.1.3.3 Main ADC Module

The Main ADC Module has 16 input channels and each channel has analog circuits for differentiation, pole-zero cancellation, integrating, amplification and offset adjustment. For the formation of the wave form it has analog circuit, Fast Flash ADC (14bit, 125MSPS), High-power Digital Signal Processor (DSP: 8000 MIPS). ADC convert analog signal to digital. and the digitized data is stored in First In First Out memory (FIFO). When a trigger signal from the Coincidence Module comes, the FIFO sends the digitized data to a Digital Signal Processor (DSP). The pulse height is calculated by using the DSP and the calculated value is sent to another DSP for control via McBSP lines connected through a CPLD. The control DSP bundled 100 sets o f the data from the 16 channels, and put into a Dual Port Memory. The bundled data is read out from the Dual Port Memory with a PC.

6.1.4 Data Acquisition

In the detector, there is a dead time in which time the detector can not measure energy for data processing. In order to evaluate this dead time, the pseudo signal of the random pulser is directly input to the pre-amplifier of each crystal. The wave height of this signal is extremely high equivalent to 10 MeV as energy, and it is not a problem in the Gd (n,γ) experiment with a Q value of about 8 MeV. Since this random pulser knows the release number within the measurement time, the actual measurement time measured for each crystal can be obtained from the detection number.

$$Actual\ Measurement\ Time = \frac{Number\ of\ random\ pulsers\ detected}{Number\ of\ random\ pulsers\ released} \times Measurement\ time \tag{6.1}$$

From the above, the data to be acquired is summarized below. Since only Ge cluster detector was used in this experiment, crystal number i = 1 to 14. Neutron beads targeted to concentrated Gd in this setup. Random pulser: Obtain the actual measurement time of each crystal from the difference between the number of releases and the number of detections. The data acquisition information are shown in Table 6.8.

TABLE 6.8: Data Acquisition Information

Name	Explanation	Use
TOF	Flight time	for neutron energy
H_i	Each Ge crystal measure wave height of the signal	γ-ray energy
T_i	Time difference between the trigger time and signal time of each Ge crystal	Synchronization for each Ge crystal

6.1.5 Event Choice in Data Acquisition

For event selection conditions, γ-rays were observed with at least one Ge crystal in the Coincidence Module, with the threshold at the Fast Timing Module being 100 keV, demanding that no γ rays be observed by BGO. A trigger signal is sent to the Main ADC Module only for events that satisfy this condition.

The Main ADC Module makes a judgement when two or more events overlap when calculating energy. It is judged from the peak position from the trigger signal and the slope before the signal comes. When it is judged that the waveforms overlap, the energy information H_i is not output and it is an event having only the time difference information T_i of each Ge crystal. This event is called a Pile-up event and it is destroyed. However, since gamma rays released in one neutron capture reaction are sufficiently smaller than the time resolution of 50 ns of the detector, they are not distinguished by Pile-up processing.

In addition, the time difference from the trigger signal of each Ge crystal is recorded within 500 ns from the trigger signal. Therefore, in the event delayed by 500 ns or more, the time difference information T_i of each Ge crystal is not output and it is an event having only the energy information H_i. Because this event is a non-simultaneous event discard it. Events were selected by these processes, and the next event selection was made.

6.1.6 Raw Data Analysis

Raw data from ANNRI detector were analysed by three different ways: (1) Event selection (2) Energy calibration (3) Background subtraction.

6.1.6.1 Event Selection

In order to analyze experimental data, selection of events is required. Thermal neutron events were selected by TOF analysis and analyzed for each number of γ rays using multiplicity analysis. In this section, we describe each event selection method.

TOF Analysis

Thermal neutron events were selected by Time of Flight method. Neutron energy, E_n can be written as

$$E_n = \frac{1}{2} m_n v^2 \tag{6.2}$$

where E_n is the neutron energy, L is the length of flight and m_n is the mass of the neutron. v can be written in terms of TOF as $v = \frac{L}{TOF}$, then Eq. 6.2 can be written as $E_n = \frac{m_n}{2}(\frac{L}{TOF})^2$ and TOF can be written as $TOF = \sqrt{\frac{mL}{2E}}$.

Here , the flight length L=21.5m and neutron mass, m_n=939$[MeV/c^2]$. For neutron energy E_n=4meV,

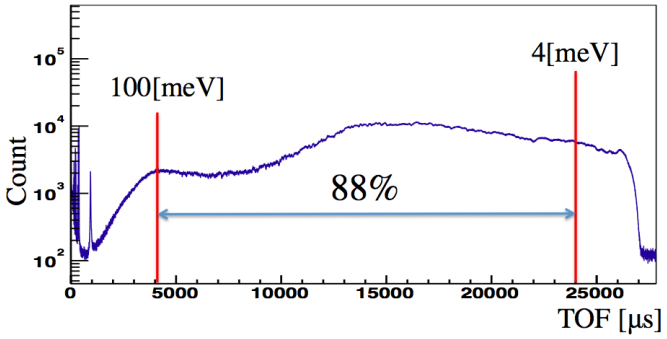

FIGURE 6.3: TOF cut spectrum for ^{157}Gd

TOF=24550 μs and for neutron E_n=100 meV , the TOF =4910μs . This includes about 88% of data. Background in thermal region is negligible $\approx 1\%$ (about 5000μs) shown in Figure 6.3.

Figure 6.4 shows the neutron energy distribution for ^{155,157}Gd. Event was selected within the thermal region 4 meV to 100 meV which is indicated by blue shade and 25 meV is the thermal neutron energy which is indicate by red line.

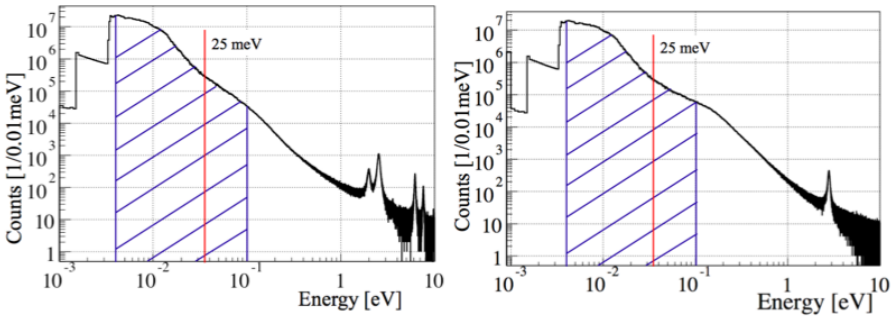

FIGURE 6.4: Neutron energy distribution for ^{155,157}Gd . Left: ^{155}Gd target and right: ^{157}Gd

Multiplicity Analysis

Since the ANNRI detector consists of seven Ge crystals both at the top and at the bottom, the number of γ rays emitted from the target can be measured by the pattern of the crystal reacted with γ rays. At that time, the energy threshold for each crystal was 110 keV. In other words, the pattern of crystals recording γ-ray energy exceeding 110 keV within one event is selected. At that time, spread of γ ray due to Compton scattering must be taken into consideration. First, when nearby crystals simultaneously detect γ rays, there is a possibility that it is a multiple Compton phenomenon by one γ ray. Let this multiplicity be (Multiplicity, M) = 1. At the same time, the number of crystals that detected γ rays is counted as the detected number (Hit Crystal, H). That is, M is the crystal group and H is the number of crystals, all cases are divided into cases. In the future, each classification is expressed like (M, H) in a sequence. Figure 6.5 shows an example of multiplicity up to (M, H) = (3, 3).

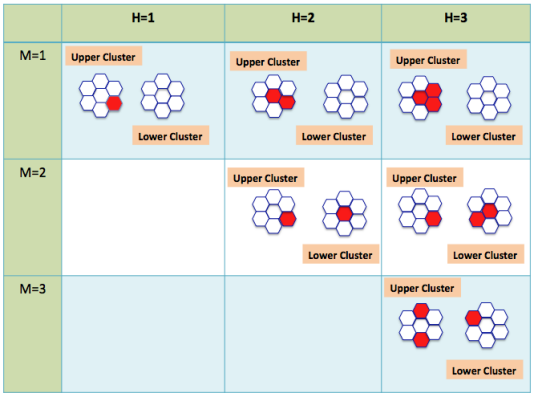

FIGURE 6.5: An example of multiplicity up to (M, H) = (3, 3). A red Ge crystal indicates a crystal in which rays are detected.

The event selection so far is summarized in Figure 6.6. Remove the Pile-up event from the raw data obtained from the Main ADC. From that point, data using neutron beams selects only thermal neutron events by TOF analysis. After that, cases were classified by Multiplicity, Hit Crystal by multiplicity analysis.

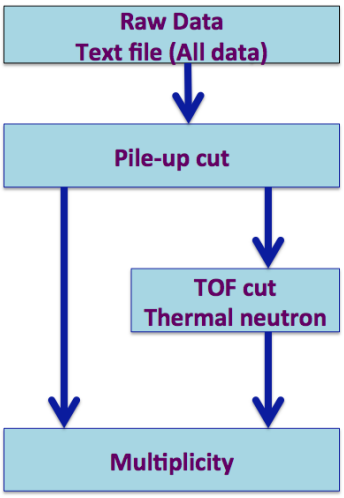

FIGURE 6.6: Block diagram of event selection

6.1.7 Energy Calibration

Energy calibration was performed using the well known γ-ray energies emitted from γ -ray source ^{22}Na, ^{60}Co, ^{137}Cs, ^{152}Eu and the neutron capture of chlorine in the NaCl sample for each Ge crystal. Energy was calibrated by below equation

$$E = a \times ch + b \tag{6.3}$$

where ch is the channel, a is the linear scale (keV/channel) or slopes, b is the intercept and E is the energy. The respective energies for the calibration sources shown in Table 6.9 .

The value obtained from the ANNRI detector is a channel value which is a digital value of a

TABLE 6.9: Calibration sources information

Source	Peak energy [keV]	I_g[%]
^{22}Na	511	90.30
	1274.58	99.94
^{60}Co	1173.24	99.85
	1332.51	99.99
^{137}Cs	661.66	85.1
^{152}Eu	344.28	26.5
	778.9	12.94
	964.08	14.61
	1408	21.01

wave height directly proportional to the energy of the γ ray. Therefore, it is necessary to convert from the ch value to the energy unit [keV]. Since the radiation source emits γ rays with a certain energy, when looking at the wave height distribution, the photoelectric absorption peak appears in the ch value corresponding to that energy. Based on this ch value, it is transformed into energy with a linear function ([keV] = a [ch] + b). The energy calibration function also changes depending on each Ge crystal and measurement date and time. Therefore, energy calibration was performed for each Run in each Ge crystal.

One example before and after energy calibration is shown. Figure 6.7 shows that the energy spectrum of ^{157}Gd is 6750. Figure shows that the Peak corresponding to 6750 keV of ^{157}Gd before and after energy calibration. Before energy calibration, about 15 channels of deviation can be seen between the data of the first day and the data of the last day. After energy calibration, it is calibrated within 2 keV.

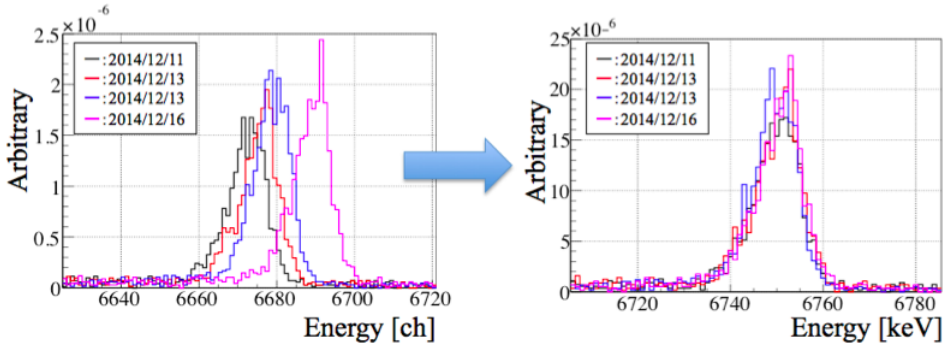

FIGURE 6.7: Energy calibration spectrum of 6750 peaks for ^{157}Gd

6.1.8 Background Subtraction

We have collected data using empty target (target holder only) to study the effects of background from the beam pipe. Figure 6.8 shows the γ ray spectrum for data of ^{157}Gd(n,γ) and background data. The background is very less (about 0.12% of main spectrum). The effect is negligible.

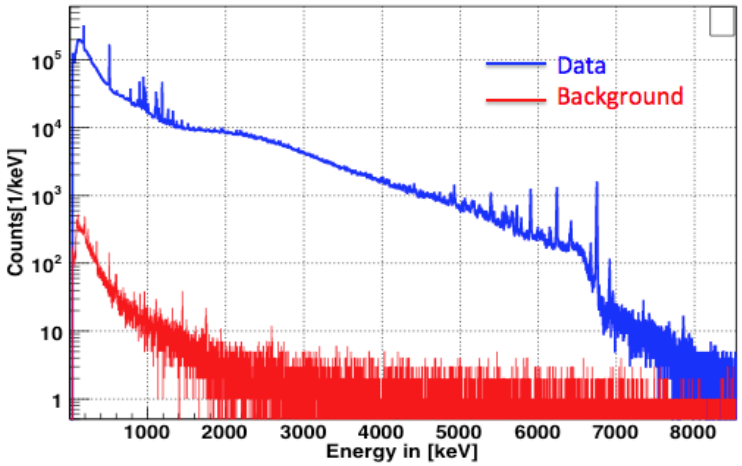

FIGURE 6.8: Energy spectrum for ^{157}Gd(n,γ) (Blue line) and energy spectrum for empty target (Red line)

Chapter 7

Analysis and Results

7.1 Efficiency Calculation

7.1.1 Absolute photo-Peak Efficiency Calculation

Absolute peak efficiency (ϵ_{abs}) is defined as

$$\epsilon_{abs} = \frac{N_p(E)}{N_F(E)} \tag{7.1}$$

where N_p(E) is the number of counts in the full energy peaks and N_F(E) is the number of photons with energy E emitted by the source. Absolute efficiency depends on the source-detector geometry and on the energy.

Absolute efficiency can be written in terms of intrinsic efficiency and geometric acceptance as

$$\epsilon_{abs} = \epsilon\eta \tag{7.2}$$

where ϵ is an intrinsic efficiency and η is the geometric acceptance.

Intrinsic efficiency is the ratio of the number of counts in full energy peak by the number of impinging or hitting photons. ϵ depends on the energy of the incident photons.

The geometrical acceptance, is the ratio of photons emitting the detector and the number of photons emitted by the source. Geometrical acceptance can be written as

$$\eta = \frac{\Omega}{4\pi} \tag{7.3}$$

where Ω is the solid angle the detector with respect to the source point.
η depends only on the source-detector geometry.

We performed our experiment using ANNRI detector at MLF, JPARC. The details of ANNRI

were explained in chapter 5. Figure 7.1 show that the clusters of Ge detector. Here, number 1 to 14 represents the crystal number. We have measured the photo-peak efficiency for all 14 crystals. The absolute photo-peak efficiencies were measured using ^{60}Co, ^{137}Cs and ^{152}Eu sources and relative efficiencies were measured from prompt γ rays of ^{35}Cl(n,γ) reaction.

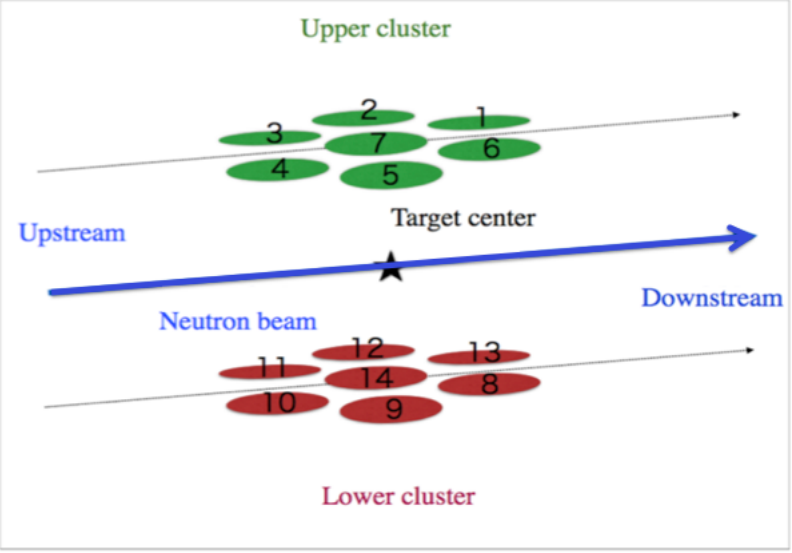

FIGURE 7.1: Cluster of ANRRI Ge Detector

7.1.2 Using ^{60}Co Source

We have analyzed M=1 and H=1 and M=2 and H=2 for coincidence method. The gamma decay scheme of ^{60}Co are as follow:

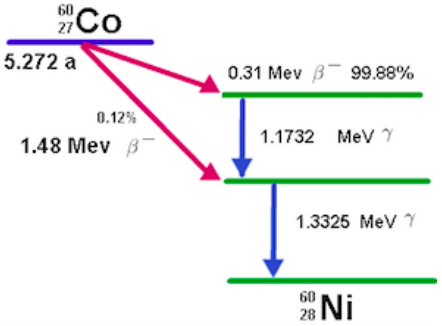

FIGURE 7.2: ^{60}Co Gamma ray decay Scheme

When a ^{60}Co nucleus decays via β-emission, it goes to one of the 2 excited ^{60}Ni states shown in Figure 7.2. About 99.88% of the time the nucleus will decay by emitting a 0.31 MeV β-particle (electron), then a 1.173 MeV γ-photon followed by a 1.332 MeV at which point, it has become ^{60}Ni.

The lifetime of the intermediate 1.332 MeV state is so short about 0.7ps, that due to the physics of the emission process, their directions are often correlated with each other. This is due to the spin of the nucleus being having an effect on the angular distribution of the emitted photons per transition.

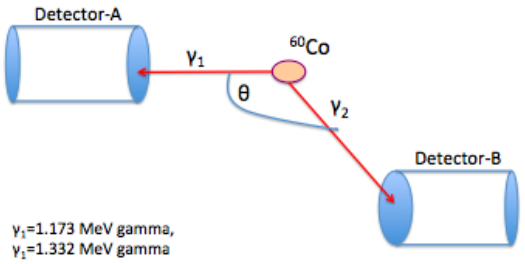

FIGURE 7.3: Angular correlation of two gamma of ^{60}Co

The relative probability that a photon will be emitted at an angle θ with respect to a previously emitted photon is denoted W(θ) and depends both on the angular momenta of the states involved in the transitions and on the multiple order of the emitted radiation.

$$W(\theta) = 1 + A_{22}P_2(cos\theta) + A_{44}P_4(cos\theta) \tag{7.4}$$

Where P_n represent the Legendre polynomial and A_{22} and A_{44} are the co-efficient of the polynomial. Where A_{22}=0.1020 and A_{44}=0.0091
If we consider cosθ=z, then the equation become

$$W(z) = 1 + 0.1020P_2(z) + 0.0091P_4(z) \tag{7.5}$$

where the polynomials are

$$P_2 = \frac{1}{2}(3z^2 - 1) \tag{7.6}$$

$$P_4 = \frac{1}{8}(35z^4 - 30z^2 + 3) \tag{7.7}$$

By putting this value we get

$$W(z) = 0.0398z^4 + 0.119z^2 + 0.952 \tag{7.8}$$

Here, $W(\theta)$ gives the ratio of the likelihood of detecting a photon at an angle θ. The angle between each crystals with other (shown in chapter 5) were calculated. As we have angle, θ (angle between two detector shown in Figure 7.3), then we get z by using $z = cos\theta$.

The γ ray spectrum of ^{60}Co was analyzed from the experimental data of ^{60}Co source by using root for all 14 crystals. Figure 7.4 shows that the γ spectrum of ^{60}Co for C7 (C7 is the crystal at the center position of the upper cluster) for M=1, H=1. The number of events of different peaks are calculated .

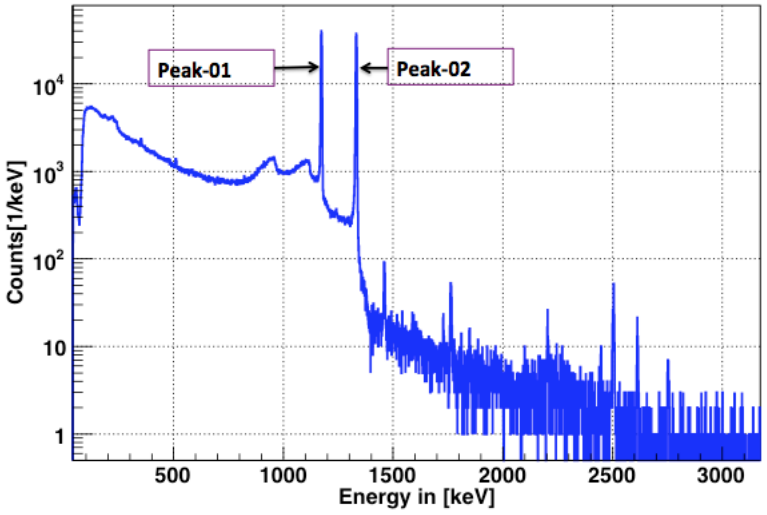

FIGURE 7.4: γ spectrum of ^{60}Co for C7 detectors

The peak-1 is at 1173keV and peak-2 is at 1332 keV (shown in Figure 7.4). The Number of events of peaks-1(1173keV) and peaks-2(1332keV) were calculated for all 14 crystals.

7.1.2.1 Coincidence Method

We know, ^{60}Co emits two γ rays. There are many different ways by which these two γ rays can be detected by the Ge-detector. Consider the case when two γ rays goes two different crystals. Consider two different crystal A and B. If N_1,N_2 are the number of events of corresponding γ rays of energy 1.173

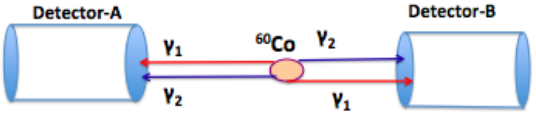

FIGURE 7.5: Two Ge detector

MeV, 1.332MeV and N_3 and N_4 is the number of events of their coincidence of ^{60}Co . Then we get

$$N_1^A = \beta T \eta_1^A \epsilon_1^A (1 - C) \tag{7.9}$$

$$N_2^A = \beta T \eta_2^A \epsilon_2^A (1 - C) \tag{7.10}$$

$$N_1^B = \beta T \eta_1^B \epsilon_1^B (1 - C) \tag{7.11}$$

$$N_2^B = \beta T \eta_2^B \epsilon_2^B (1 - C) \tag{7.12}$$

$$N_3 = \beta T \eta_1^A \epsilon_1^A \eta_2^B \epsilon_2^B W(\theta_{AB}) \tag{7.13}$$

$$N_4 = \beta T \eta_2^A \epsilon_2^A \eta_1^B \epsilon_1^B W(\theta_{AB}) \tag{7.14}$$

Where in N_1^A ("1" represent the γ-rays number and "A" represents the detector number) is the number of events of γ_1 of Detector -A. Where N_3 is the number of events of the coincidence when γ_1 hit detector A and γ_2 hit in the detector-B and N_4 is the number of events of the coincidence when γ_1 hit detector B and γ_2 hit in the detector-A. where η_1, η_2 = Geometrical acceptance , ϵ_1, ϵ_2= Intrinsic photo-peak efficiency , $\eta\epsilon$=Absolute photo-peak efficiency. β is the activity of the radioactive source ^{60}Co, T is the measurement time, and C is the correction for veto counter trigger, in our calculation we used $C = 0.20$ (explained in Appendix A.1). The angle, θ_{AB} of each pairs and then calculated the $z = cos\theta_{AB}$. For each pairs, we have different angle and different z and that will give W(z) of different pairs.

Calculation of N_3 and N_4 by Coincidence method

To calculate N_3 and N_4, the number of events for overlap of the two gamma rays or for coincidence method, we need to draw two dimensional histogram.

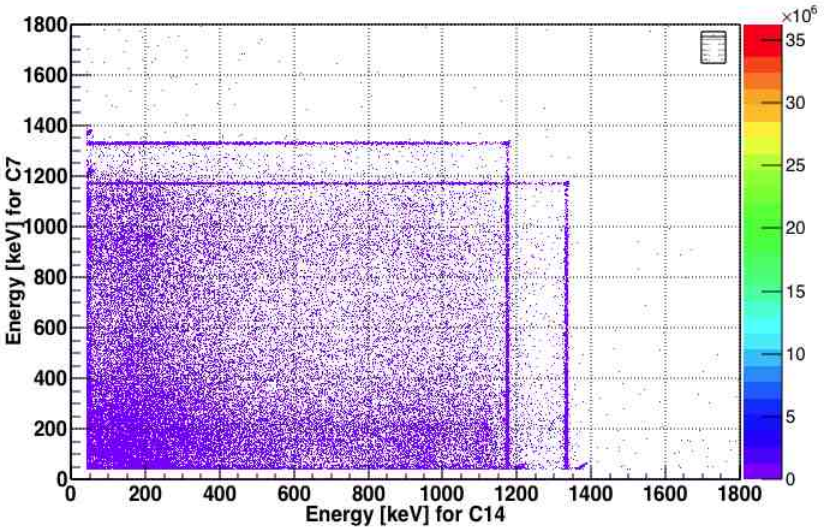

FIGURE 7.6: 2D histogram for C7 and C14

Figure 7.6 shows that the 2D histogram of ^{60}Co for two pair of detectors C7 and C14. N_3: When γ_1 hit C7 and γ_2 hit other C14 crystal. N_4: When γ_2 hit C7 and γ_1 hit other C14 crystals. The coincidence number of events N_3 and N_4 was calculated. Similarly, the coincidence events of N_3 and N_4 for all the combination were calculated.

7.1.2.2 Correcting Dead Time

In experiment, Ge detector has dead time in counting γ rays. So, we need to correct the dead time from the ratio of random pulse number generated and number actually recorded in the experiment. DAQ system recorded the number of events of both the random timing pulses and the pulses originated from γ rays. A scaler circuit was counted the number of random timing pulses at the same time. The

dead time was corrected by using the following equation

$$r_L = \frac{N_{Pul}}{P(t)} \tag{7.15}$$

where t be the flight time, r_L be the dead time correction factor. N_{Pul} is the number of random timing pulses per energy spectrum bin calculated from the scaler counts. P(t) is the TOF- dependent counts of the random timing pulses .

The dead time corrected number of events of each detector and their pairs or number of their coincidence are given as,

$$N_1^A = \beta T r_L^A \eta^A \epsilon_1^A (1 - C) \tag{7.16}$$

$$N_2^A = \beta T r_L^A \eta^A \epsilon_2^A (1 - C) \tag{7.17}$$

$$N_1^B = \beta T r_L^B \eta^B \epsilon_1^B (1 - C) \tag{7.18}$$

$$N_2^B = \beta T r_L^B \eta^B \epsilon_2^B (1 - C) \tag{7.19}$$

$$N_3 = \beta T r_L^{AB} \eta^A \epsilon_1^A \eta^B \epsilon_2^B W(\theta_{AB}) \tag{7.20}$$

$$N_4 = \beta T r_L^{AB} \eta^A \epsilon_2^A \eta^B \epsilon_1^B W(\theta_{AB}) \tag{7.21}$$

Where, r_L^A is the dead time correction factor for detector A , r_L^B is the dead time correction factor for detector B and r_L^{AB} is the dead time correction factor for their pairs.

Let us consider, $a = \beta T$, $b = \eta^A \epsilon_1^A$, $c = \eta^A \epsilon_2^A$, $d = \eta^B \epsilon_1^B$, $e = \eta^B \epsilon_2^B$, $f = W(z)$, $r_L^A = h$, $r_L^B = i$, $r_L^{AB} = j$ Then we can write the equation of N_1, N_2, N_3 and N_4 as,

$$N_1^A = abh(1 - C) \tag{7.22}$$

$$N_2^A = ach(1 - C) \tag{7.23}$$

$$N_1^B = adi(1 - C) \tag{7.24}$$

$$N_2^B = aei(1 - C) \tag{7.25}$$

$$N_3 = abefj \tag{7.26}$$

$$N_4 = acdfj \tag{7.27}$$

The formula for χ^2-method is given below.

$$\chi^2 = (\frac{N_1^A - abh(1-C)}{\sigma_1})^2 + (\frac{N_2^A - ach(1-C)}{\sigma_2})^2 (\frac{N_1^B - adi(1-C)}{\sigma_3})^2 + (\frac{N_2^B - aei(1-C)}{\sigma_4})^2 + (\frac{N_3 - abefj}{\sigma_5})^2 + (\frac{N_4 - acdfj}{\sigma_6})^2 \tag{7.28}$$

Where σ_1, σ_2, σ_3, σ_4, σ_5 and σ_6 are the statistical errors of N_1^A ,N_2^A, N_1^B,N_2^B,N_3 and N_4 respectively.

Then, the efficiencies were calculated from χ^2-formula using MINUIT program by making minimum χ^2 value. The efficiency of γ_1 and γ_2 were measured for all 49 pairs of detectors. By taking average we got the efficiency of γ_1 and γ_2 for all 14 crustal (shown in Figure 7.7).

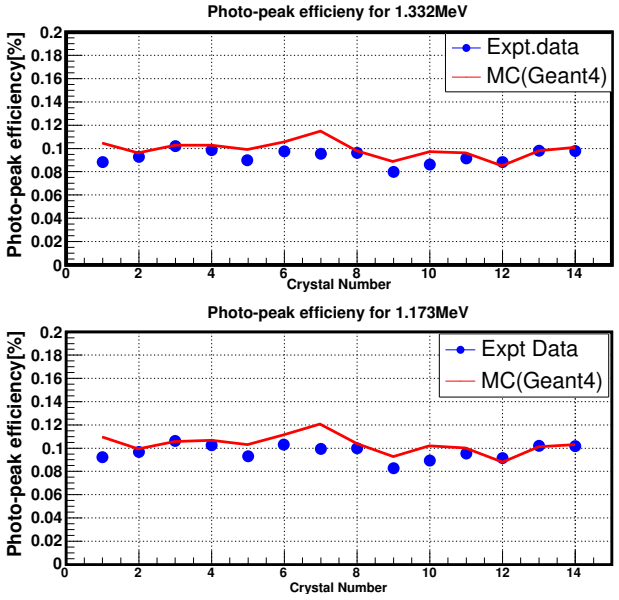

FIGURE 7.7: Comparison of photo-peak efficiency of calculation and MC(Geant4)

Figure 7.7 shows the comparison of the photo-peak efficiency of ^{60}Co data and MC (Geant4). The agreement between data and MC (Geant4) is about 95%. We also predicted the activity of ^{60}Co source from χ^2 formula (Eq. 7.28). The predicted activity is in good agreement with the nominal activity of the radiation source. Figure 7.8 shows the comparison between the predicted activity and nominal activity for all 14 crystals. For a single crystal, say C7, we obtained the photo-peak efficiency, $\eta\epsilon = 1.00 \pm 0.05 \times 10^{-3}$ and activity, β=4.82$\pm$0.23 kBq while nominal activity, β=4.85 kBq.

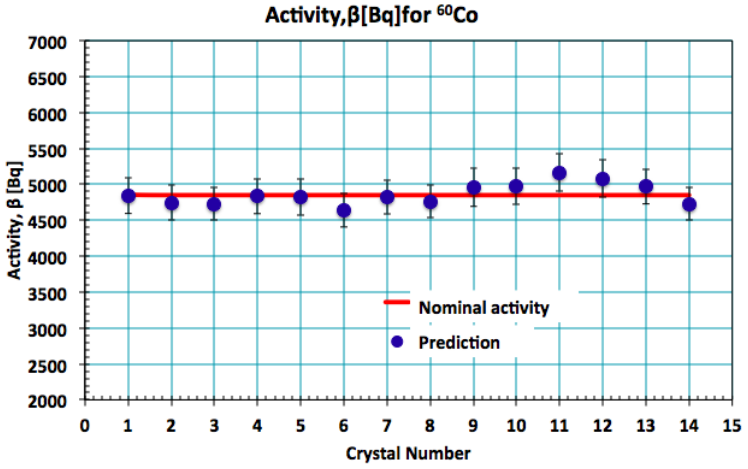

FIGURE 7.8: Comparison of activity of prediction and nominal value

7.1.3 Photo-Peak Efficiency Calculation Using ^{137}Cs

The decay of ^{137}Cs has two paths. ^{137}Cs goes to ^{137m}Ba by β^- is about 94.4% and directly goes ^{137}Ba by β^- which is about 5.6% (shown in Figure 7.9).

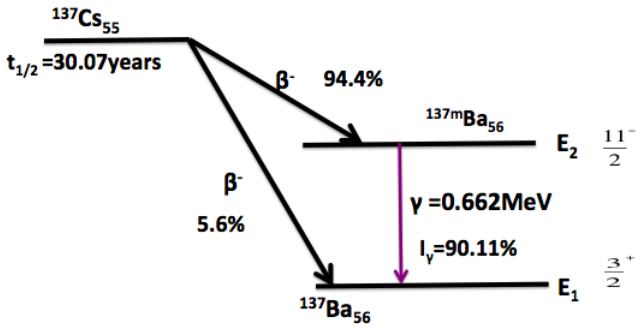

FIGURE 7.9: Decay scheme of ^{137}Cs source

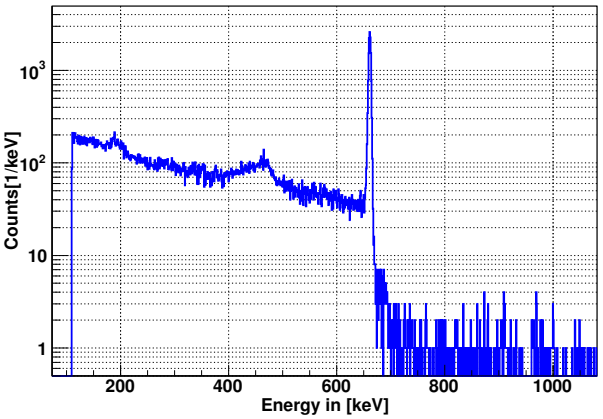

FIGURE 7.10: γ spectrum of ^{137}Cs

$$^{137}_{55}Cs \rightarrow ^{137m}_{56}Ba + \beta^- + \bar{\nu}_e \tag{7.29}$$

Then ^{137m}Ba decay γ-ray of energy 0.662MeV to go ^{137}Ba by about 90.11% and ^{137m}Ba goes about 9.89% by internal conversion.

$$^{137m}_{55}Cs \rightarrow ^{137}_{56}Ba + \gamma \tag{7.30}$$

The total branching ratio for decaying γ-ray from ^{137}Cs is about 85.1%

Figure 7.10 shows the experimental γ spectrum for ^{137}Cs. The number of events N_i can be written as

$$N_i = 0.851 \times \beta T_L \eta\epsilon \tag{7.31}$$

where, β is the activity for ^{137}Cs source, $\eta\epsilon$ is the photo-peak efficiency, T_L is the live time , Live time, $T_L = r_L T$ where, T is the measurement time, r_L is the dead time correction factor (from Eq. 7.15). Then efficiency can be written as

$$\eta\epsilon = \frac{N_i}{0.851 \times \beta T_L} \tag{7.32}$$

The efficiency was calculated from Eq. 7.29 for all 14 crystals. Then, the photo-peak efficiency for ^{137}Cs was compared with MC(Geant4) efficiency .

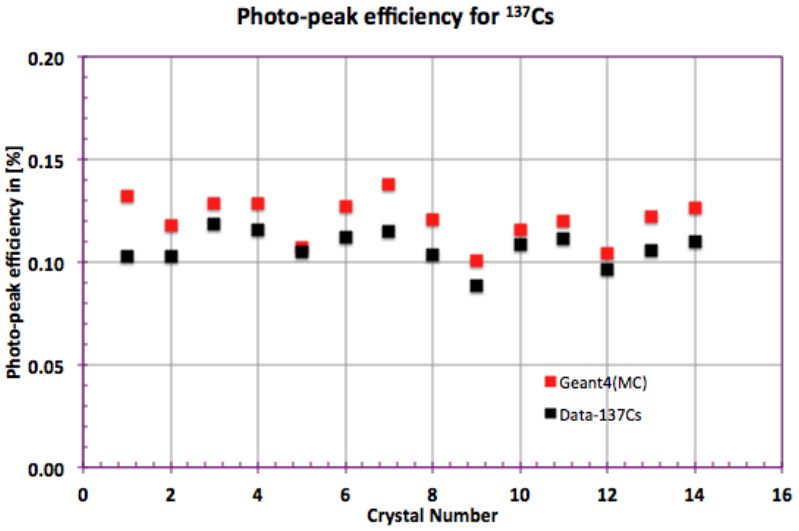

FIGURE 7.11: Photo-peak efficiency for ^{137}Cs

Figure 7.11 shows the comparison of the photo-peak efficiencies between data and MC(Geant4) for ^{137}Cs. The agreement between data and MC(Geant4) efficiency is about 90%. The activity, β is predicted from the below equation

$$\beta = \frac{N_i}{0.851 \times \eta\epsilon T_L} \tag{7.33}$$

where photo-peak efficiency, $\eta\epsilon$ is measured from MC(Geant4). Figure 7.12 shows the comparison between predicted activity and the nominal activity of ^{137}Cs. For single crystal such as C12, we ob-

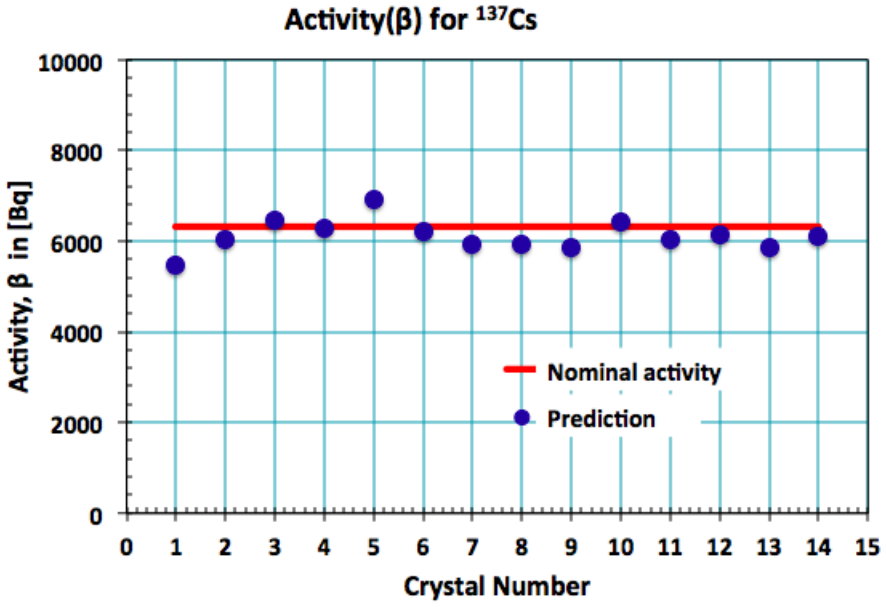

FIGURE 7.12: activity for ^{137}Cs

tained activity of ^{137}Cs , $\beta = 6.14 \pm 0.08$ kBq (nominal activity for ^{137}Cs, β=6.32 kBq) for photo-peak efficiency,$\eta\epsilon = 1.15 \times 10^{-3}$.

The agreement between the data and MC(Geant4) for ^{60}Co is about 95% and the agreement between data and MC(Geant4) for ^{137}Cs is about 90%. The overall agreement between our data and MC(Geant4) is about 92% estimated form both ^{60}Co and ^{137}Cs. So, we have about 8% discrepancy between data and MC(Geant4) (shown in Figure 7.13).

From the studies of ^{137}Cs and ^{60}Co, we have found that MC(Geant4) efficiency are always larger than

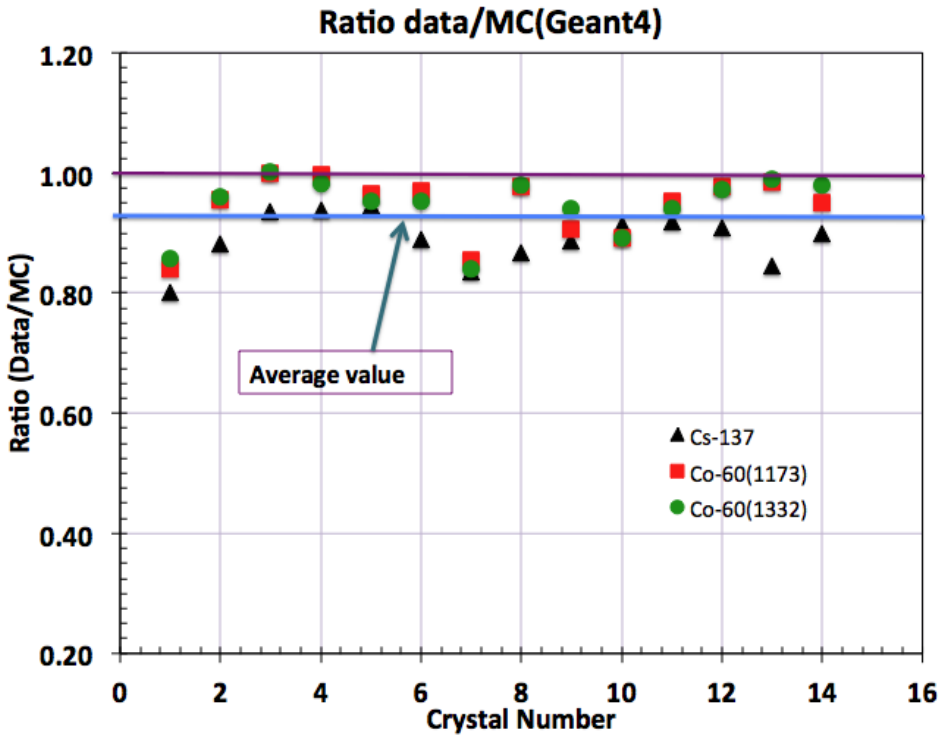

FIGURE 7.13: Comparison of the ratio (data/MC) for ^{60}Co and ^{137}Cs

data. MC(Geant4) simulation for single γ is always over estimated . So, we need a correction factor in MC(Geant4) efficiency. The correction factor F is 0.92.

7.1.3.1 Using ^{152}Eu

^{152}Eu disintegrates in three different ways. It disintegrates 72.1% by electron capture ($^{152}_{63}Eu + e^- \rightarrow ^{152}_{62}Sm^* + \nu_e$), about 0.027% for β^+ or positron emission ($^{152}_{63}Eu \rightarrow ^{152}_{62}Sm^* + e^+ + \nu_e$) and about 27.9% by β^- emission ($^{152}_{63}Eu \rightarrow ^{152}_{64}Gd^* + e^- + \overline{\nu_e}$).

Schematic diagram of γ emission of $^{152}_{63}Eu$:

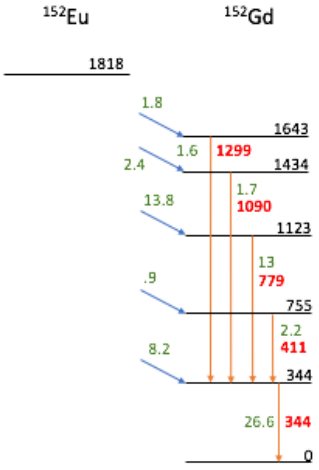

FIGURE 7.14: γ spectrum of ^{152}Eu for β^-

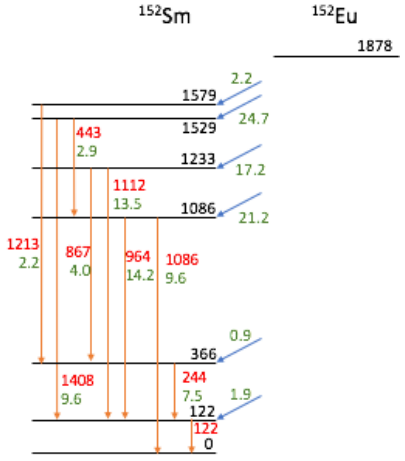

FIGURE 7.15: γ spectrum of the electron capture of ^{152}Eu

In Figures 7.14 and 7.15, the numbers in green colors represent events per 100 disintegrations, the number in black colors represent the energy level in keV, the numbers in red color represent the energy of transition (γ -ray energy) in keV and blue arrows represent the branch i.e % from the upper level.

Figure 7.16 shows that the experimental γ ray spectrum of ^{152}Eu source. There are a few prominant γ rays coming out from ^{152}Eu. Among them 4 γ rays have large branching ratios and they are 344 keV, 779 keV, 1112 keV and 1408 keV. Table 7.1 shows the decay scheme of ^{152}Eu the number of γ rays and their branching ratios.

TABLE 7.1: Decay scheme of ^{152}Eu source

Selected γ rays	Simultaneous γ ray	Branching ratio (%)	Relative branching ratio (%)
344 keV	single or 779 keV	26.6	79.3 (30.8+48.5)
779 keV	344 keV	12.9	99.2
1112 keV	121.8 keV	13.4	97
1408 keV	121.8 keV	20.9	>99.5

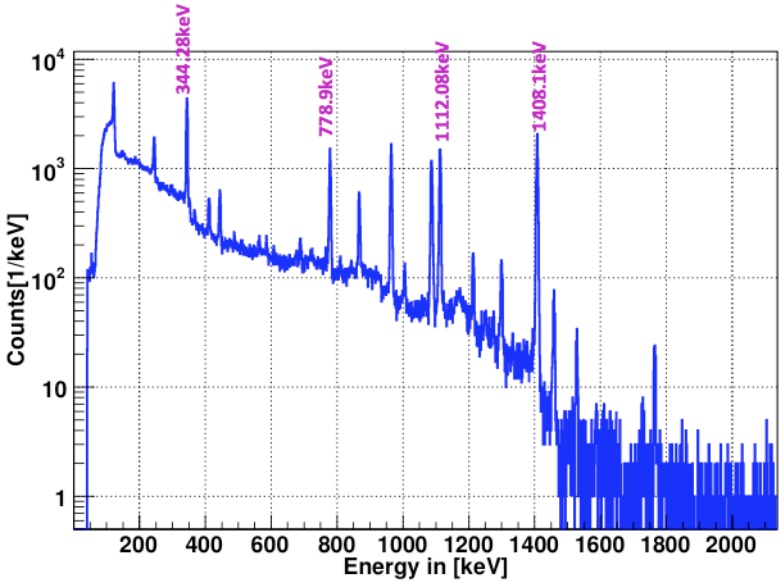

FIGURE 7.16: Gamma spectrum of ^{152}Eu

Photo-peak efficiency calculation:

The number of events emitted from the source can be written as

$$N_\gamma = b_\gamma \beta T_L \eta \epsilon \tag{7.34}$$

where b_γ is total branching ratio of that energy level, T_L is the live time $T_L = r_L T$, T is the measurement time and r_L is the dead time correction factor (from Eq. 7.15).
Photo-peak efficiency can be written as

$$\eta\epsilon = \frac{N_\gamma}{b_\gamma \beta T_L} \tag{7.35}$$

γ ray source ^{152}Eu emit multiple γ rays and γ ray emitted simultaneously. So, a correction of number of count needed to compute the photo-peak efficiency. Then the corrected efficiency can be written as

$$\eta\epsilon_{corr} = C_\gamma^{norm} \frac{N_\gamma}{b_\gamma \beta T_L} \tag{7.36}$$

where C_γ^{norm} is the normalization factor introduced for multiple simultaneous γ rays and which can be written as $C_\gamma^{norm} = \frac{\eta\epsilon_{single}^{MC}}{\eta\epsilon_{double}^{MC}}$. where $\eta\epsilon_{single}^{MC}$ is the MC(Geant4) peak efficiency for single γ and $\eta\epsilon_{double}^{MC}$ is the MC(Geant4) peak efficiency for double γ ray. Using Eq. 7.36 we have calculated the photo-peak efficiency of γ rays of ^{152}Eu source. Figure 7.17 shows that the photo-peak efficiency of γ rays from ^{152}Eu source for crystal number C11. Similarly, we have calculated the photo-peak efficiency of γ rays from ^{152}Eu source for all 14 crystals. Some detector need case re-normalization for target case.

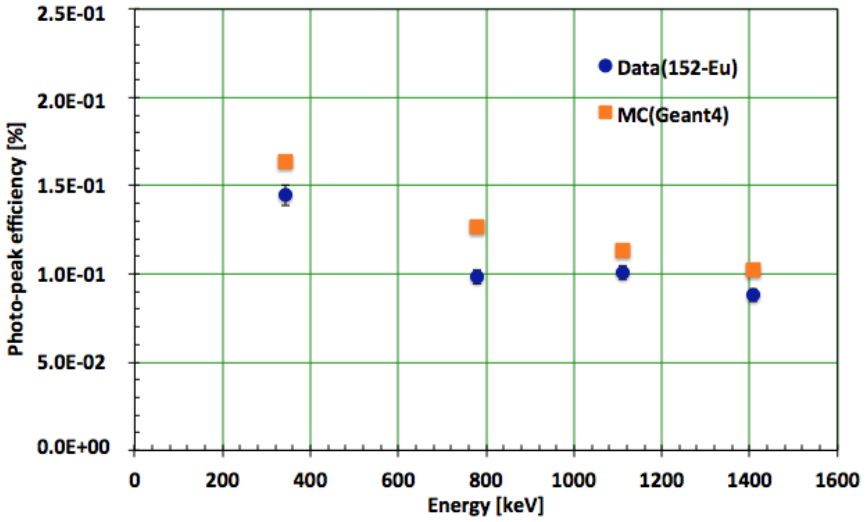

FIGURE 7.17: Photo-peak efficiency of ^{152}Eu for C11 crystal

Case re-normalization:

The target case of the ^{152}Eu source is coated with a layer of Duralumin (Al(93%+Cu(4%)+etc(<1%)). This case some time causes in γ ray propagation through this this layer of the material. It was found that some crystals (C2, C5, C7,C9, C12 and C14) received about 2% less γ rays in average. These additional correction were made into efficiencies for those crystals.

7.1.4 Relative Efficiency Calculation

We have measured the relative efficiencies of the γ rays from the thermal neutron capture on ^{35}Cl i.e ^{35}Cl(n,γ) reaction. The reaction can be written as

$$n_{th} + ^{35}Cl \rightarrow ^{36}Cl^{*} \rightarrow ^{36}Cl + \gamma,\ 8.5MeV \tag{7.37}$$

We have analysed the γ spectrum of ^{35}Cl(n,γ) reaction. Figure 7.18 shows that the experimental data of γ spectrum for ^{35}Cl(n,γ reaction.

There are few γ rays are coming out from ^{36}Cl. Among them some are most dominant. The most dominant γ rays emitting from ^{36}Cl are 5517 keV, 7414 keV, 7790 keV and 8578 keV. The relative branching ratios and relative intensities of those γ ray given below. Table 7.2 shows the dominant decay path of γ rays from ^{36}Cl and their branching and relative intensities.

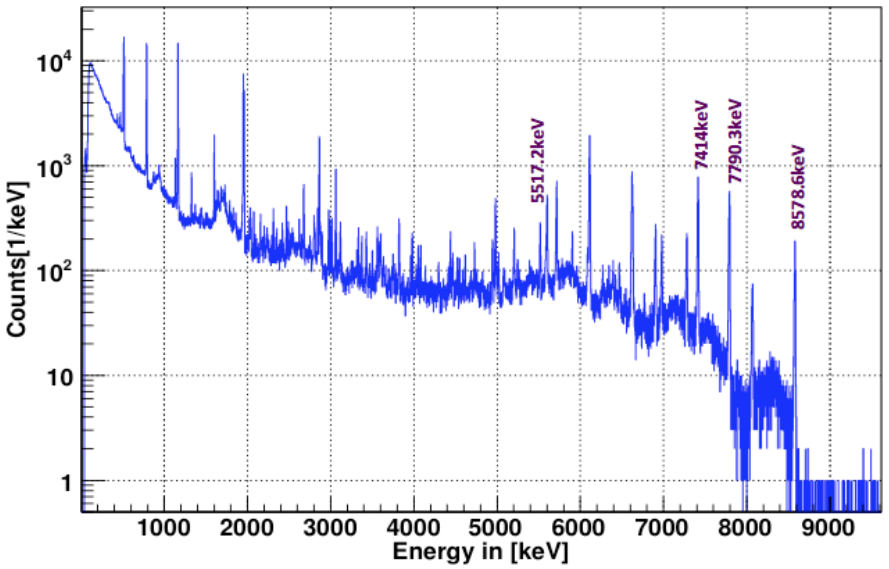

FIGURE 7.18: γ spectrum of ^{35}Cl(n,γ) for C11 crystal

Figures 7.19, 7.20, 7.21 and 7.22 show that the dominant decay scheme of the γ ray decay path for ^{36}Cl. The number in green colors represent events per 100 disintegration, the number in black colors represent the energy level in keV, the numbers in red color represent the energy of transition in keV, blue arrows represent the branch i.e % from the upper level and the red arrows represent the γ-ray emission.

TABLE 7.2: Dominant decay path of γ from ^{36}Cl

studied γ rays	simultaneous γ rays	Relative Intensity (%)	Realtive branching (%)
5517 keV	3061 keV	17.5	~93
7414 keV	1164 keV	100	>99.5
7790 keV	788 keV	85.4	>99.5
8578 keV	single γ	33.1	100

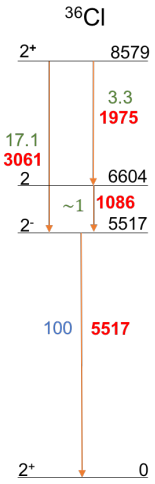

FIGURE 7.19: 5517 keV decay scheme of ^{36}Cl

FIGURE 7.20: 7414 keV decay scheme of ^{36}Cl

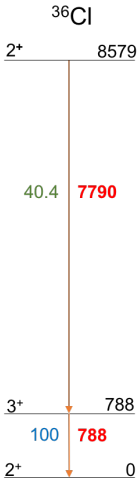

FIGURE 7.21: 7790 keV decay scheme of ^{36}Cl

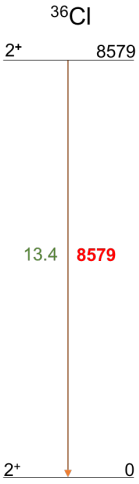

FIGURE 7.22: 8578 keV decay scheme of ^{36}Cl

To calculate the relative efficiency we need a reference point. A specific γ ray (γ_0) is set to have nominal efficiency and which can be got from the MC(Geant4) simulation. Then, the relative efficiency is calculated using relative branching ratios from the formula:

$$\eta\epsilon^{\gamma,i}_{norm} = \frac{N^i_\gamma C^{norm,i}_\gamma}{b_\gamma(\frac{N_{\gamma 0 i} C^{norm,i}_{\gamma 0}}{b_{\gamma 0}\eta\epsilon^i_{\gamma 0,norm}})} \tag{7.38}$$

where $C^{norm,i}_\gamma = \eta\epsilon^{MC}_{single}/\eta\epsilon^{MC}_{double}$ is the normalising factor introduced for multiple simultaneous γ-rays and the factor $\frac{N_{\gamma 0 i} C^i_{\gamma 0}}{b_{\gamma 0}\eta\epsilon^i_{\gamma 0,norm}}$ can be interpreted as a calculation of the total number of events assuming that detector i is perfect. Then, we have calculated the relative photo-peak efficiency for γ rays from ^{35}Cl(n,γ) reaction using Eq. 7.38.

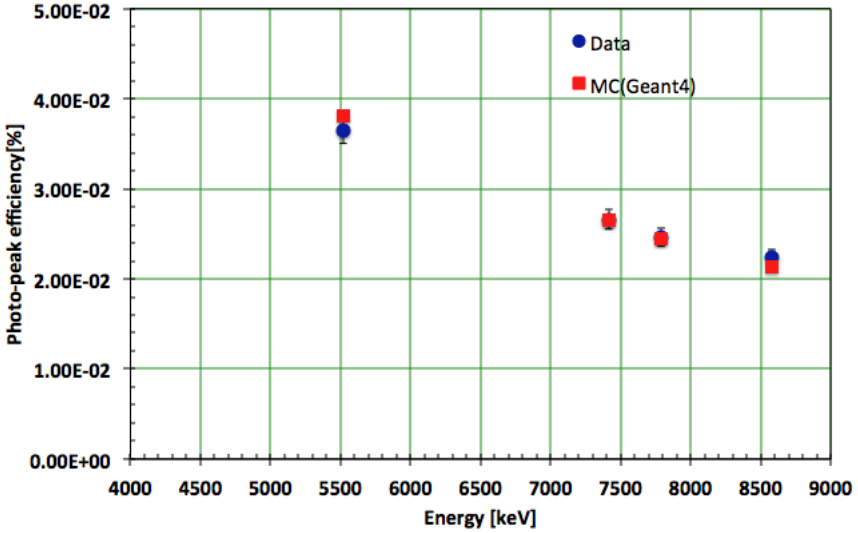

FIGURE 7.23: Photo-peak efficiency of ^{35}Cl(n,γ) for C11 crystal

Figure 7.23 shows the photo-peak efficiency of γ rays from ^{35}Cl(n,γ) reaction for C11 detector. We have found a good agreement between data and MC(Geant4). Similarly, we have calculated the photo-peak efficiency of γ rays from ^{35}Cl(n,γ) reaction for all 13 detectors.

7.2 Geant4 Monte Carlo (MC) Simulation

7.2.1 Geant4

Geant4 (for GEometry ANd Tracking)[52, 53] is a platform for ”the simulation of the passage of particles through matter,” using Monte Carlo methods. It is the successor of the GEANT series of software toolkits developed by CERN, and the first to use object oriented programming (in C++). Its development, maintenance and user support are taken care by the international Geant4 Collaboration. Application areas include high energy physics and nuclear experiments, medical, accelerator and space physics studies. The software is used by a number of research projects around the world. Geant4 [52, 53] includes facilities for handling geometry, tracking, detector response, run management, visualization and user interface.

7.2.2 Geant4 Simulation for ANNRI

We have successfully made the geometry of ANNRI using Geant4 version 9.6.p 04 including all the Physics condition inside it. A detailed description of the geometry of the array and environment with respect to their dimensions, materials and shapes, as well as the particle generator, is required by the GEANT4 toolkit to simulate the history of each particle from its generation to the deposition of its energy in the array. (In Figure 7.24 and 7.25, BGO=Bismuth Germanium Oxide, Al=Aluminium, Ge=Germanium, LiH=Lithium hydride, Pb=Lead and B=Boron).

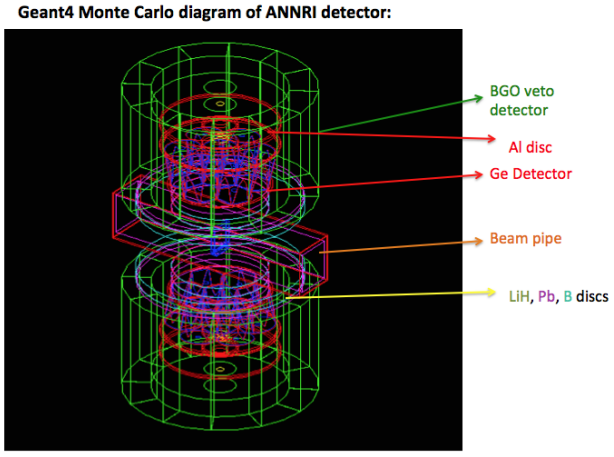

FIGURE 7.24: Geometry (wire-frame) of ANNRI detector in Geant4

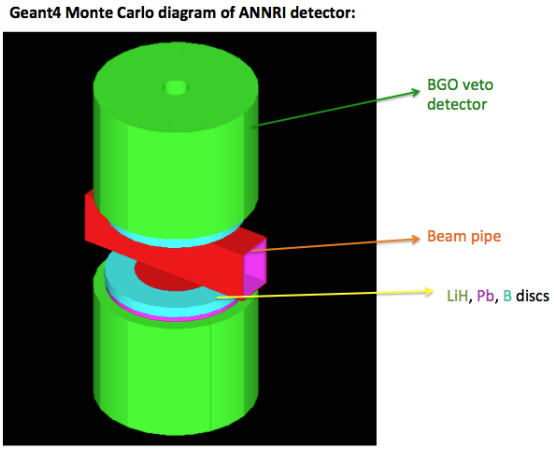

FIGURE 7.25: Block diagram of ANNRI detector

7.2.2.1 Detection of the Event by MC (Geant4)

We have generated γ-rays of energy 100keV to 9000keV. We have generated γ rays for three

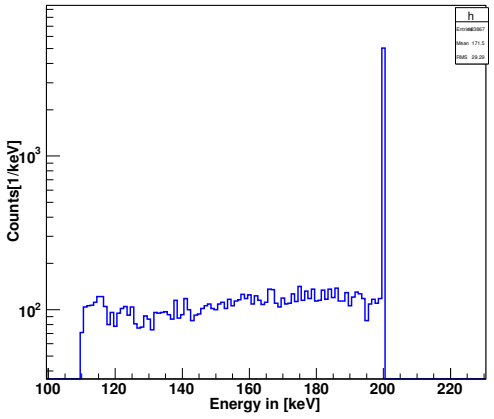

FIGURE 7.26: MC γ energy spectrum fro 200 keV

different target case. (1) Acrylic case (for ^{60}Co, ^{22}Na and ^{137}Cs source. (2) Duralumin (for ^{152}Eu source. (3) None (no target case for ^{35}Cl, ^{155}Gd and ^{157}Gd). Figure 7.26 shows the energy spectrum of 200 keV γ for acrylic case.

7.2.2.2 MC Detection Efficiency

The number of detected gamma rays by the Ge detector out of the total number of gamma rays generated by the MC(Geant4) is called the detection efficiency.

$$\epsilon_{MC(Geant4)} = \frac{N_c}{N_s} \times 100\% \tag{7.39}$$

Where N_c=is the number of gamma rays detected by the Ge detector. N_s= is the total number of gamma rays generated by MC (Geant4)

Figure 7.27 shows that the MC efficiency for C7 crystal for acrylic case. Similarly, We have

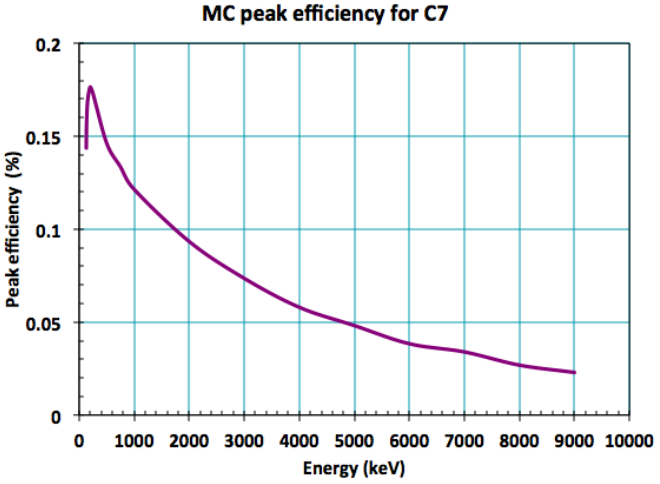

FIGURE 7.27: MC efficiency for acryl target case of C7

calculated the efficiency for all 14 Ge crystals.

7.2.2.3 Generation of 1γ, 2γ and 3γ in MC(Geant4)

By using MC (Geant4)simulation, we can generate single γ for different energies and 2 γ and 3 γ rays together. We have generated single γ ray of 662keV for ^{137}Cs source. Figure 7.28 shows that the MC(Geant4) γ spectrum for ^{137}Cs. We have generated 2γ of energy 1173keV and 1332keV for ^{60}Co source. We have generated 3γ for ^{22}Na source (2 γ of 511keV and one γ of 1275keV). Figure 7.29 and Figure 7.30 show that the MC(Geant4) γ spectrum for ^{60}Co and ^{22}Na respectively.

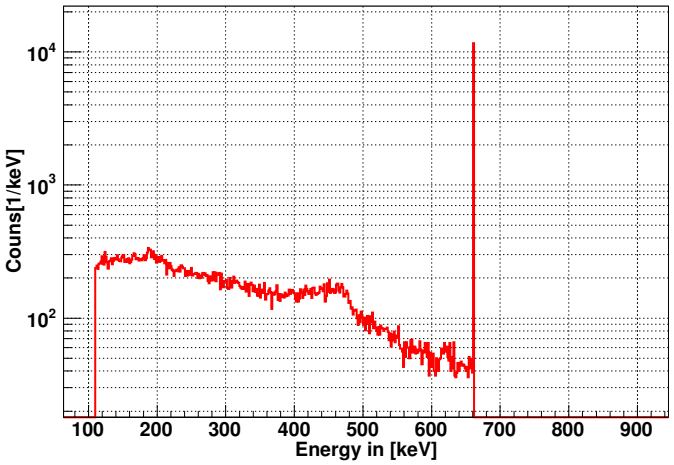

FIGURE 7.28: MC of ^{137}Cs source

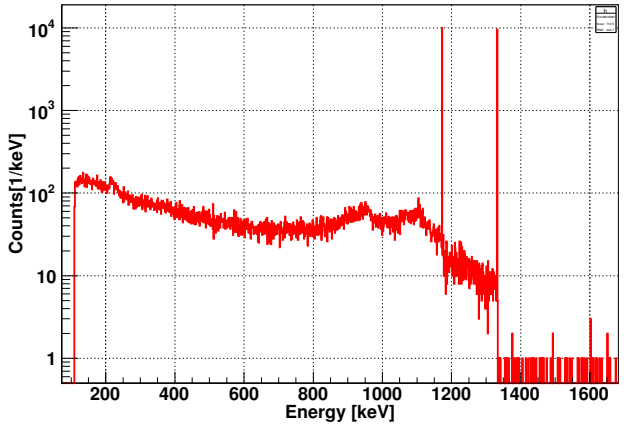

FIGURE 7.29: MC of ^{60}Co source

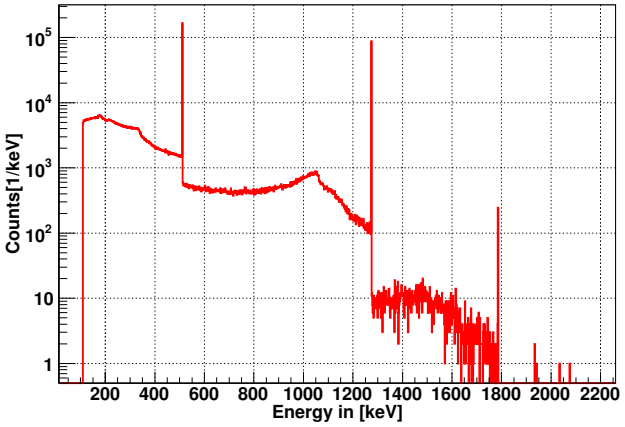

FIGURE 7.30: MC of ^{22}Na source

7.2.2.4 Comparison Between Data and MC

Then we have compared the experimental data with data generated from MC(Geant4) simulation. Figure 7.31 shows that the comparison between the energy spectrum of data and MC for ^{137}Cs source. The efficiency was calculated by using below equation

$$\eta\epsilon = \frac{N_i}{0.851 \times \beta T} \tag{7.40}$$

Figure 7.32 shows that the comparison between the photo-peak efficiency of 662 keV γ ray of data and MC for ^{137}Cs. The agreement between the photo-peak efficiency is good and it is about 90%.

Figure 7.33 shows that the comparison between the energy spectrum of data and MC for ^{60}Co. Photo-peak efficiencies were calculated by using the coincidence method similar to data analysis. In MC (Geant4) data, there is no dead time so we do not need the dead time correction factor. Here, γ rays were generated uniformly hence we don't need any angular correlation term. From Eq. 7.33, we can write the χ^2 formula for MC as

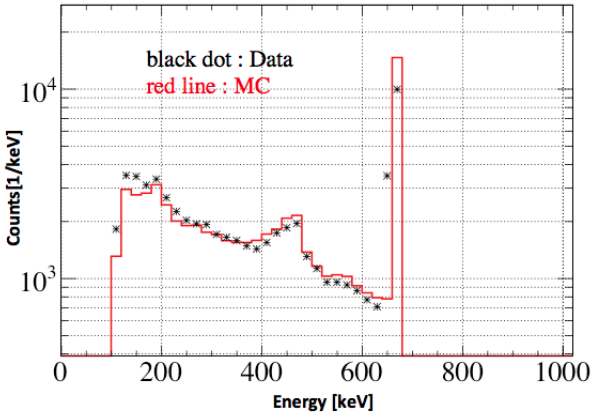

FIGURE 7.31: Comparison of data and MC of ^{137}Cs source

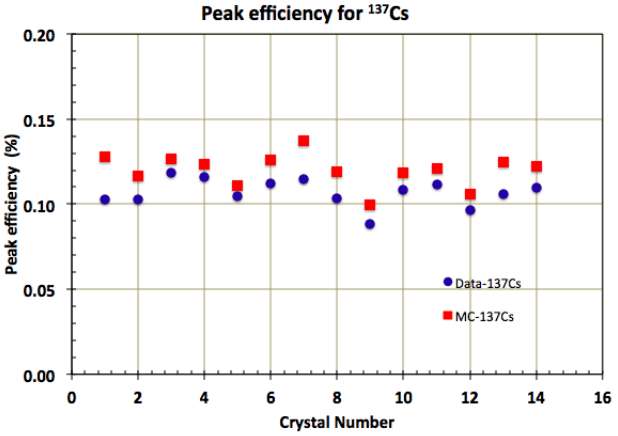

FIGURE 7.32: Photo-peak efficiency for ^{137}Cs

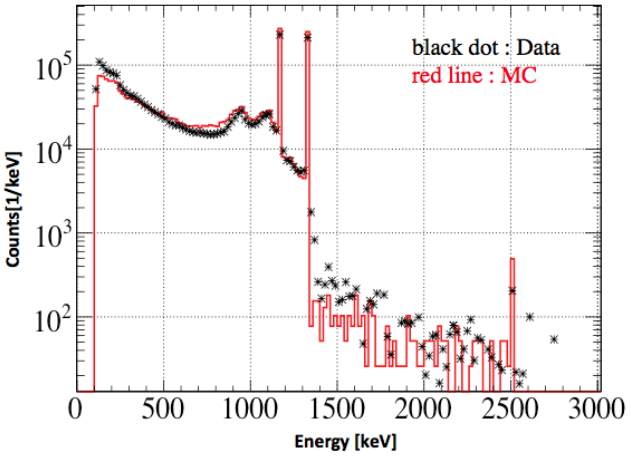

FIGURE 7.33: Comparison of data and MC for ^{60}Co source

$$\chi^2 = (\frac{N_1^A - ab(1-C)}{\sigma_1})^2 + (\frac{N_2^A - ac(1-C)}{\sigma_2})^2(\frac{N_1^B - ad(1-C)}{\sigma_3})^2 + (\frac{N_2^B - ae(1-C)}{\sigma_4})^2 + (\frac{N_3 - abe}{\sigma_5})^2 + (\frac{N_4 - acd}{\sigma_6})^2 \tag{7.41}$$

We have calculated the absolute efficiency of MC(Geant4) for ^{60}Co using coincidence method with the help of the Eq. 7.41. Here the correction for veto counter trigger, C=0.22 (see Appendix A.1.1) . We have calculated the efficiencies for all the pairs and got the final value of efficiency by taking average value. Figure 7.34 and Figure 7.35 show the comparison between the photo-peak efficiencies between the data and MC for ^{60}Co. The agreement between the data and MC is very good and the agreement is about 95%. From the studies of MC(Geant4) data of ^{137}Cs and ^{60}Co we can find the overall agreement between our data and MC(Geant4) is about 92%.

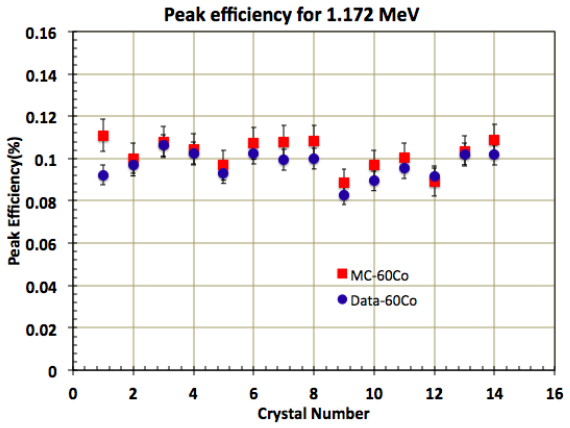

FIGURE 7.34: Photo-peak efficiency for ^{60}Co

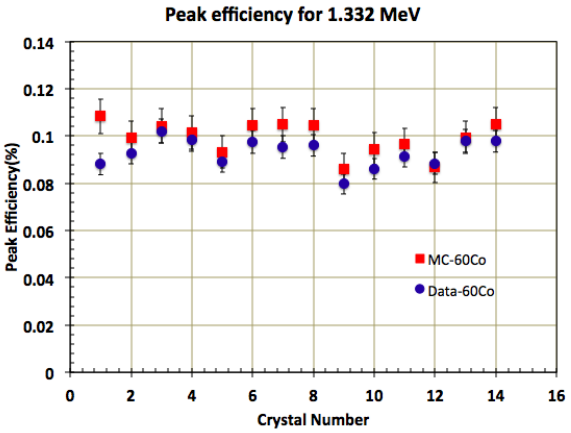

FIGURE 7.35: Photo-peak efficiency for ^{60}Co

Figure 7.36 shows the comparison of energy spectrum between the data and MC for ^{22}Na. From

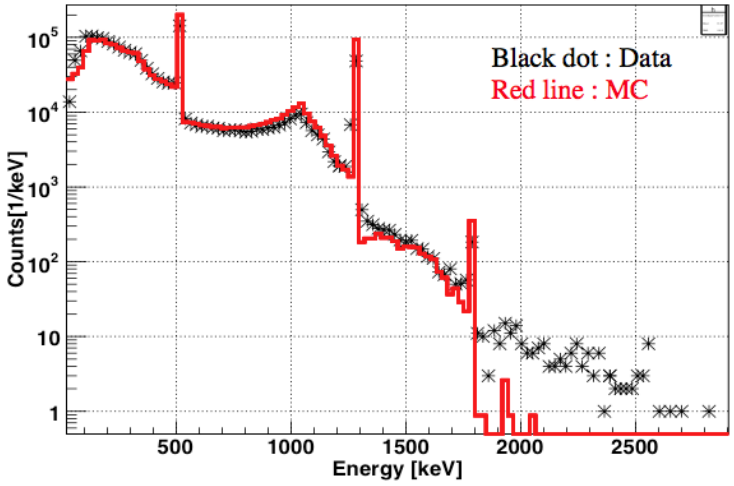

FIGURE 7.36: Comparison of data and MC for ^{22}Na source

the comparison between data and Mc(Geant4) of ^{137}Cs, ^{60}Co and ^{22}Na, we found that our data and MC(Geant4) are in good agreement in both photo-peak and Compton region (shown in Figures 7.31, 7.33 and 7.36).

7.2.3 Corrected Detection Efficiency

From the studies of ^{137}Cs and ^{60}Co, we found that MC(Geant4) values are always larger than data (MC(Geant4) values are over estimated). We have determined the overall correction factor for MC(Geant4) single γ rays. The MC(Geant4) detection efficiency (Figure 7.27) can be corrected with the help of correction factor as

$$\epsilon_{corr} = F * \epsilon_{MC} \tag{7.42}$$

where F is the correction factor (F=0.92), ϵ_{corr} is the corrected detection efficiency and ϵ_{MC} is the detection efficiency for MC(Geant4).

Figure 7.37 shows the comparison between the corrected detection efficiency with the MC(Geant4)

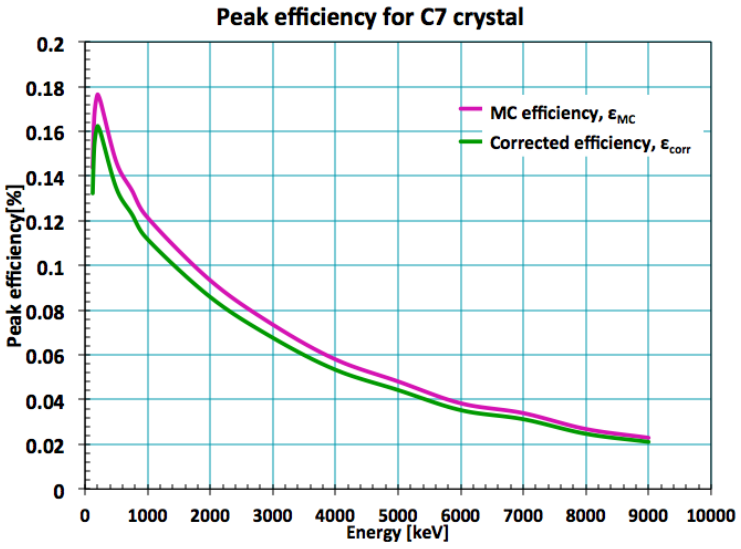

FIGURE 7.37: Comparison between the MC(Geant4) efficiency and the corrected efficiency

detection efficiency for C7 crystal. Similarly, we have corrected the detection efficiency of other 13 crystals. We have used this corrected detection efficiency for relative intensity calculation for discrete γ rays.

7.2.4 Comparison between the photo-peak efficiency of data and MC(Geant4)

We have compared the efficiency of data and MC(Geant4) simulation for all 14 detectors. Figure 7.38 shows that the ratio of data to MC(Geant4) efficiency detector to detector. Where points were weighted average for all γ rays. And red and black error bars are maximum and standard deviation respectively. Figure 7.39 shows that the ratio of data to MC(Geant4) efficiency γ-ray by γ-ray. Where points were weighted average for all 14 detectors and where color and black error bars are maximum and standard deviation respectively.

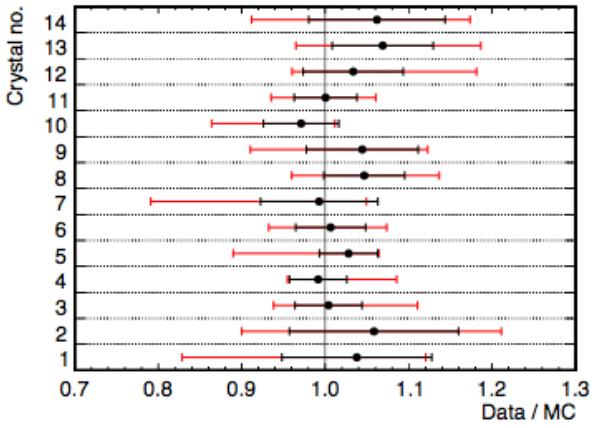

FIGURE 7.38: Ratio of data to MC(Geant4) efficiency detector to detector

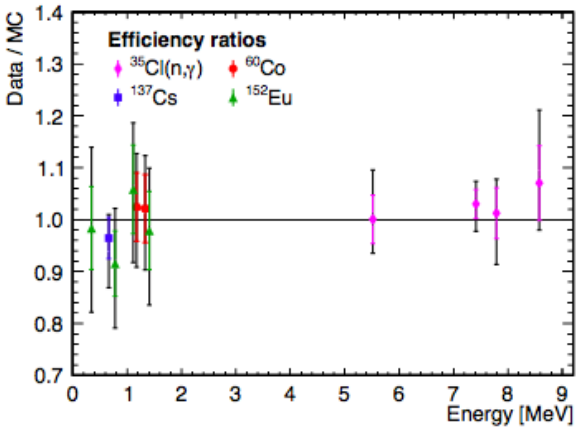

FIGURE 7.39: Ratio of data to MC(Geant4) efficiency γ ray by γ ray

Then we have compared the photo-peak efficiency of data (absolute photo-peak efficiency from ^{60}Co, ^{137}Cs and ^{152}Eu and relative efficiency from ^{35}Cl(n,γ) reaction. From figure 7.38, we can see that the MC(Geant4) value are always larger than data for C1 and C7 crystal. Figure 7.40 shows that the comparison between data and MC(Geant4) for C11 crystal. The comparison between the absolute

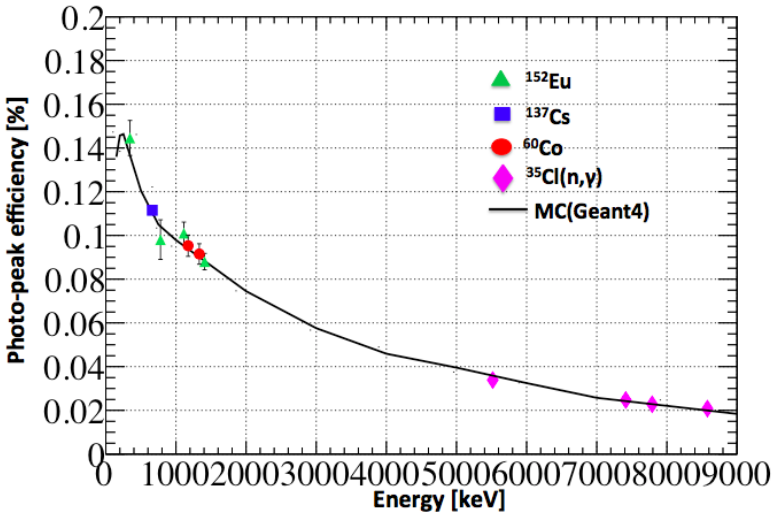

FIGURE 7.40: Photo-peak efficiency for for C11

photo-peak efficiency, relative photo-peak efficiency and MC(Geant4) photo-peak efficiency for all 14

crystals were plotted in Appendix A.2. We therefore confidently claim that we have understood the photo-peak efficiency form 0.1 to 9 MeV within 10% uncertainty and which is equal to the estimated systematic errors of the detector.

7.3 Energy Resolution of Ge Detector of ANNRI

The energy resolution of a detector is very important for γ-rays detection experiments. It measures its ability to distinguish γ-rays with close energies. The energy resolution of the detector can be defined as σ. where σ is the standard deviation or the width of Gaussian parameter (shown in Figure 7.41). E is the energy of the center or mean of the Gaussian peak. The relative resolution can be written as $\frac{\sigma}{E}$ We have calculated the sigma of any peaks by using fitting with Gaussian equation in Eq. 3.12. We

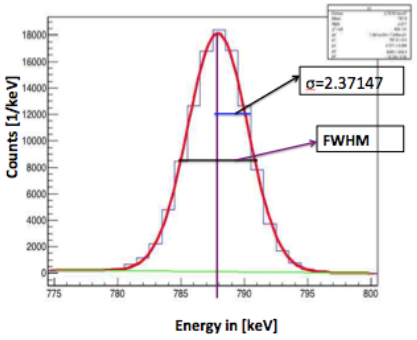

FIGURE 7.41: Gaussian fitting of a γ ray peak of ^{35}Cl(n,γ) for C7

have calculated the σ from all the photo-peaks peaks of ^{35}Cl(n,γ), ^{152}Eu and ^{157}Gd(n,γ). We observed that data ($\frac{\sigma}{E}$) are well fit as $\frac{\sigma}{E} = \frac{a}{E} + b$ shown in Figure 7.42 (where a=1.784 and b=0.00405). The resolution at 1.3MeV for C7 crystal is 2.25KeV.

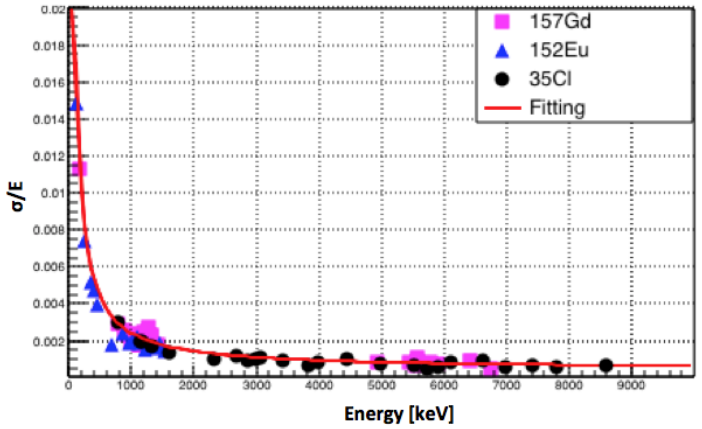

FIGURE 7.42: Resolution for C7 crystal

Then we have calculated the resolution of all 14 detectors. The resolution of all 14 crystal shown in Appendix A.3.

7.4 Position Dependency

We performed the experiment on thermal neutron capture with enriched Gd in 2014. The enriched Gd target was made of Gd_2O_3 powder, so it was very difficult to determine the exact position of the target. To confine the MC(Geant4) simulation properly, we need to know the geometry of the detector and the whole environment of ANNRI precisely including the exact position of the target. To determine the exact position of the target, we carried out another experiment in 2015 which used the γ sources ^{22}Na and ^{60}Co in absence of neutron beam. In this experiment, we took data at different positions.

We consider the beam direction in Y-axis. The upstream of the beam is in the negative (-) Y-axis

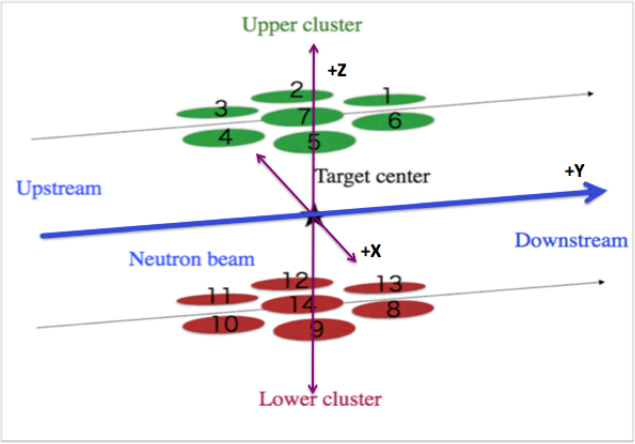

FIGURE 7.43: Configuration of the ANNRI germanium detectors

and the downstream of the beam is in the positive (+) Y-axis (shown in Figure 7.43). We consider the upside as the (+) Z-axis and the downside as the negative (-) Z-axis. We consider left side from the beam direction as the negative (-) X-axis and the right side of the beam direction as positive (+) X-axis (Figure 7.43 and 7.44).

We changed the target position from left to right side by two different position 2.5mm and 5mm

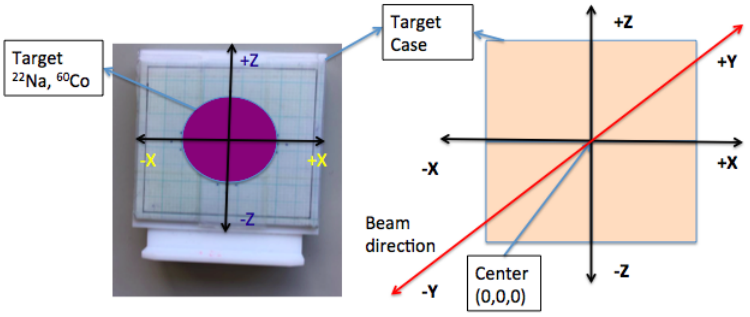

FIGURE 7.44: Positioning of the target case

and from upside to downside have changed by 2.5mm and 5mm and we changed upstream and downstream by 5mm. Our aim was to measure the count rate for different positions and compare them with the count rate in the center position.

Determination of the Count Rate

Let us consider that the number of events of any γ ray peak is N for any source. Moreover, there are two types of pulser. We get the random timing pulser or machine pulser during the experiment time and another pulser can be found from the pulser count of the energy spectrum. We can write the dead time correction factor from Eq. 7.15 as

$$r_L = \frac{N_{Pul}}{P(t)} \tag{7.43}$$

The live time, true measurement time, is

$$T_L = T_R \times r_L \tag{7.44}$$

For the count rate finally as follows

$$R_c = \frac{N}{T_L} \tag{7.45}$$

7.4.1 Using ^{22}Na Source

The ^{22}Na source emits three γ rays. Two of them are back to back with 511 keV energy each and other one has 1275 keV energy. Figure 7.45 shows the γ-ray energy spectrum of ^{22}Na source for different positions.

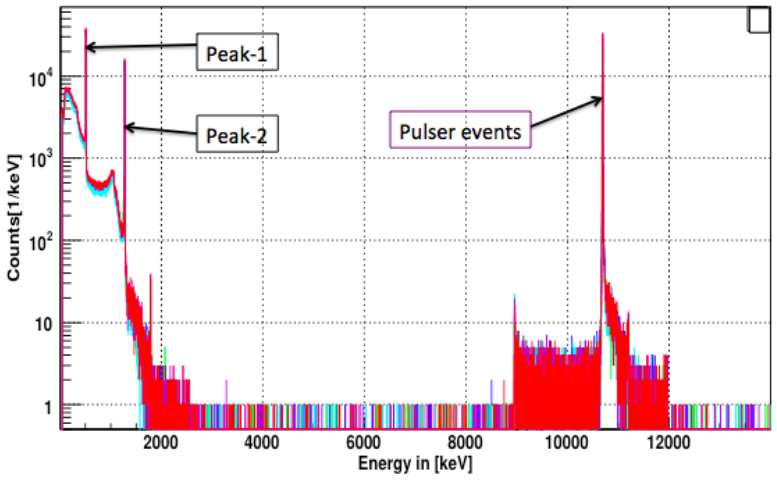

FIGURE 7.45: Energy spectrum of ^{22}Na for different source position

The number of events in peak-1 (511keV) and peak-2 (1275 keV) were calculated for different positions of all 14 crystals. Then we calculated the number of pulser for all the position including center for all crystal. Figure 7.46 shows the pulser events for C7 for different source positions.

We have the machine pulser (random timing pulser) during the experiment, $P(t)$=485486. With this number, we calculated the dead time correction factor, r_L by using Eq. 7.43. Our run time is, $T_R = 643$ s. We calculated the live time with Eq. 7.44. The count rate was calculated by using Eq. 7.45. This procedure was repeated for all different positions and for all 14 counters. Figure 7.47 summarises

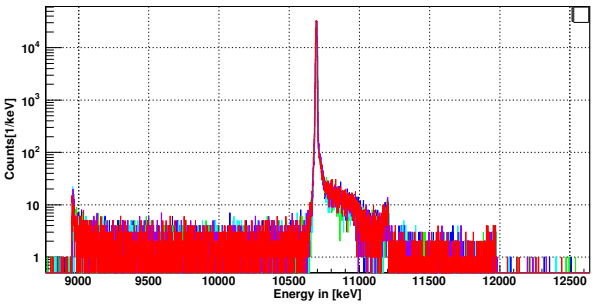

FIGURE 7.46: Pulser counts of C7 for ^{22}Na source at all positions

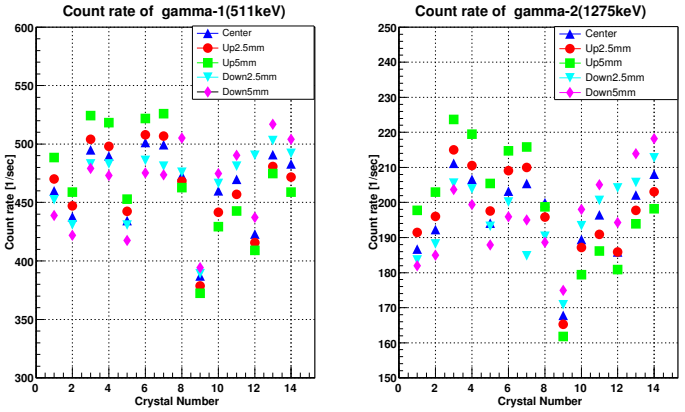

FIGURE 7.47: Summarises of the count rates for ^{22}Na source at different positions Z-axis

the count rates for all 14 crystals at the different positions along the up and down direction. As an example, Figure 7.48 shows more clearly the change in count rate for different source positions in up-down for crystal C1.

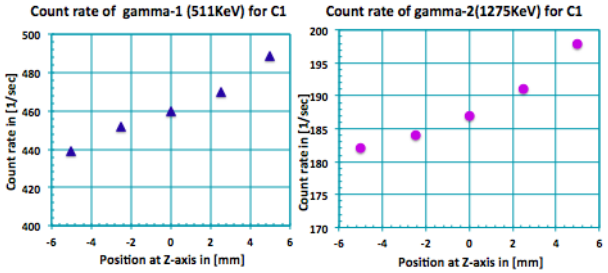

FIGURE 7.48: Count rate of crystal C1 for ^{22}Na source at different positions relative to the center

Figure 7.47 and 7.48 show that the changes in count rate for the upper crystals are almost proportional to the source position change. Similarly, the count rate for the lower crystals is inversely proportional to the target distance.

Figure 7.49 shows the summary of count rates for different position in left-right side direction including the center position for all 14 crystals. From Figure 7.49 we determine the variation of the count rate with change of the source position along the X-axis (Left-Right side).

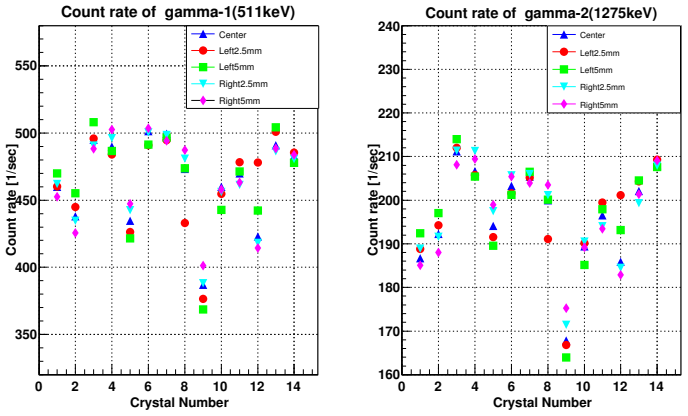

FIGURE 7.49: Summarises of the count rates for ^{22}Na source at different positions along X-axis

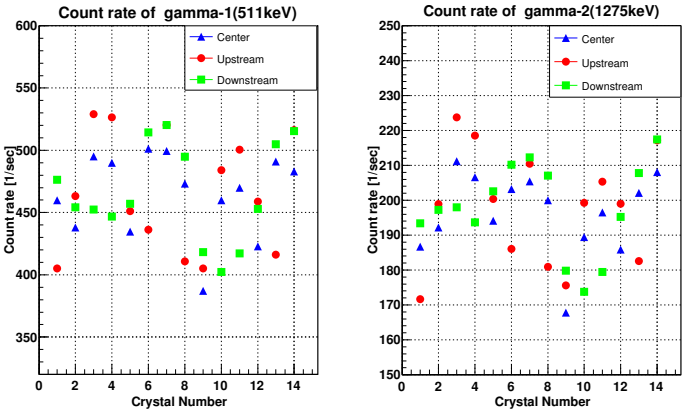

FIGURE 7.50: Summarises of the count rates for ^{22}Na source at different positions along Y-axis

Figure 7.50 shows the summary of count rates for different position in upstream-downstream direction including the center position for all 14 crystals. From Figure 7.50 we determine the variation of the count rate with change of the source position along the Y-axis (Upstream-Downstream).

Figure 7.51 shows that the variation of count with respect to target position in all three axis for

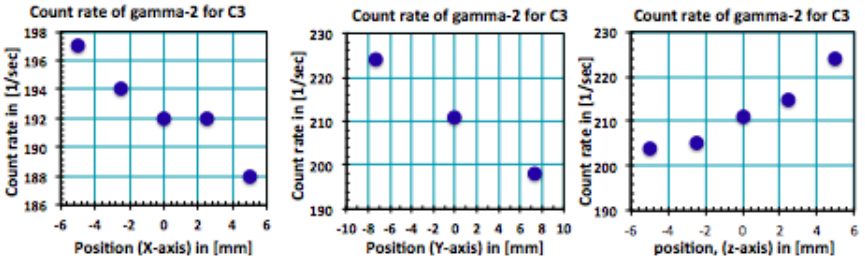

FIGURE 7.51: Count rate of crystal C3 for ^{22}Na source at different positions (X,Y and Z)

C3. By using this count rate variation we can calculate the accurate target position.

7.5 Target position calculation

We have experimental data i.e number of γ ray events corresponding to different peaks both for ^{35}Cl and ^{157}Gd for all the 14 Ge crystals (ANNRI detector). We have also Monte Carlo (MC) simulated efficiencies where the target is assumed to be at center. Once we plot experimental data and Monte Carlo generated values, we see quite discrepancy in values (see Figure 7.52). This points out that the assumed position is not the center position.

In 2015, another experiment was conducted in which γ ray events were measured (using ^{22}Na and ^{60}Co as source) at different positions giving us insight into the position dependency of the count rate for all the 14 crystals. We have calculated the normalized efficiency by using the experimental data of ^{35}Cl of 1165keV and experimental data ^{157}Gd and then compared the MC(Genat4) efficiency of 1MeV γ rays. This is the normalized efficiency of 1165keV γ rays of ^{35}Cl for C_1 and have done the same thing to calculate the normalized efficiency for other 13 crystals. Similarly, the normalized efficiency of 780keV and 1187keV γ rays of all 14 crystal has calculated . Then we have generated the 1MeV γ ray from MC(Geant4) simulation and calculated the efficiency and then compared with experimental data. Gaussian Probability Distribution is given by

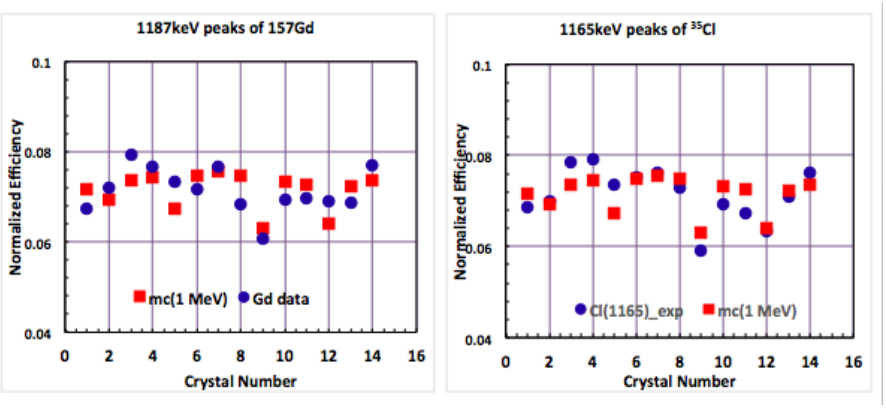

FIGURE 7.52: Normalized efficiency of ^{157}Gd and ^{35}Cl

$$f(x_i) = \frac{1}{\sqrt{2\pi\sigma}} \exp(-\frac{(x_i - \mu)^2}{2\sigma^2}) \tag{7.46}$$

In our case we define χ^2 squared distribution as

$$\chi^2 = \sum_{i=1}^{14} \left(\frac{y_i - y_i^{mc}.C_{ij}.r}{\sigma} \right)^2 + \left(\frac{r-1}{\sigma'} \right)^2 \tag{7.47}$$

where y_i is the experimental value,

y_i^{mc} is the monte carlo value,

C_{ij} is the 3-D Correction Factor,

r is the common normalization factor,

σ' = 0.02 (See Appendix A.4 and A.4.1)

σ = 0.00143 (See Appendix A.4 and A.4.1)

3-D Correction Factor

C_{ij} is three dimensional correction factor which is to be determined from position versus count rate plots. This factor stores the information about the variation of count rates with different coordinates. It has the following form

$$C_{ij} = 1 + a_i.x + b_i.y + c_i.z \tag{7.48}$$

where a_i, b_i, c_i are to determined form respective position deviation plots.
From 2015 experiment we have got the count rate versus position plots. We obtain a_i, b_i, c_i in the following manner. Let us demonstrate it using C3 (crystal 3) deviation plots (shown in Figure 7.51). And fitting of χ^2 of Figure 7.51 we get Figure 7.53, Figure 7.54 and Figure 7.55

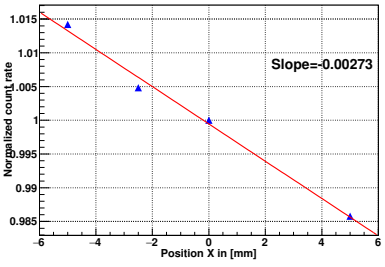

FIGURE 7.53: Fitting for ^{22}Na using χ^2

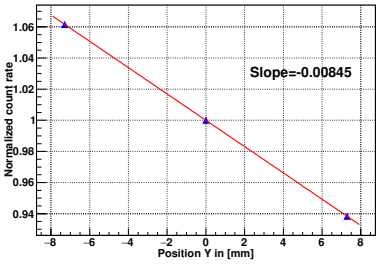

FIGURE 7.54: Fitting for ^{22}Na using χ^2

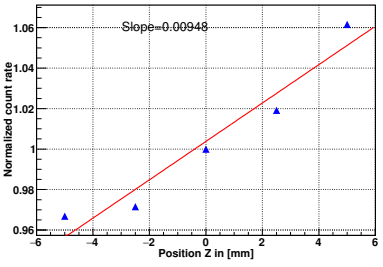

FIGURE 7.55: Fitting for ^{22}Na using χ^2

And for C7 and C14 of γ_1 and γ_2 has two types of factor (b_i^- and b_i^+) (shown in Figure 7.56).

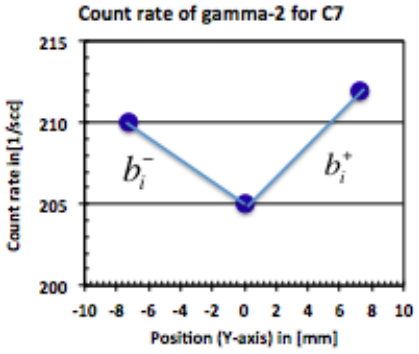

FIGURE 7.56: Fitting for ^{22}Na using χ^2 (for C7 and C14)

Normalizing the count rate with respect to center value i.e. at zero and finding the slope; we get a_i, b_i, c_i (Figures 7.53, 7.54 and 7.55)i.e deviation in count rates as the position varies along x axis, y axis and z axis respectively for crystal 3. We have repeated same procedure for the rest of the 13 crystals.

In the case of upstream-downstream data i.e. y axis plots we do not observe the linear trend for the crystal number 2, 5, 7, 8, 9 and 14 (see Figure 7.43). Count rate is low at zero position because of the teflon holder. Here, we work out with two parameters b_i^+ and b_i^- instead of just b_i; b_i^+ is positive slope and should be used for $y > 0$ and b_i^- is negative slope and should be used for $y < 0$. Once we have y_i,

y_i^{mc} , a_i, b_i^+ and b_i^- and c_i (shown in Table 7.3), then we can make a program that will run for all the possible values of x, y and z and vary r from 0.95 to 1.05. The coordinates which will give the minimum vale of χ^2 will be our desired centre position.

Compilation of the program we got the following coordinates at **r=0.99** which have minimum value of

TABLE 7.3: The correction factors, a_i, b_i and c_i for all 14 Ge detectors

Crystal No.	y_{imc}	a_i	b_i^-	b_i^+	c_i
1	0.071568177	-0.0035886	0.0077023	0.0077023	0.0083476
2	0.069268797	-0.0048137	-0.005	0.0035	0.009168
3	0.073522649	-0.0027314	-0.0084506	-0.0084506	0.0094784
4	0.074499885	0.0019726	-0.0082833	-0.0082833	0.009088
5	0.067314325	0.0051429	-0.0042	0.0063	0.008048
6	0.074787307	0.001992	0.008727	0.008727	0.0092622
7	0.075534606	0.0	-0.0033	0.0047	0.0133012
8	0.074787307	-0.00562	-0.0096	0.0066	-0.0064512
9	0.063002989	0.0063429	-0.0065	0.009798	-0.0076515
10	0.073292711	0.0019726	-0.0090535	-0.0090535	-0.00934
11	0.072602897	-0.0026263	-0.0091015	-0.0091015	-0.009812
12	0.063922741	0.002	0.0089166	0.0089166	-0.0092
13	0.072315475	-0.0020537	0.0085117	0.0085117	-0.0096
14	0.073580133	0.0	-0.0059	0.0059	-0.009616

χ^2:

Cl(1165) **(3,-1.5,3.25)** χ^2 **= 51.287**

Gd(1187) **(5.25,-2.25,2.75)** χ^2 **= 94.266**

Gd(780) **(5,-1.75,4)** χ^2 **= 87.946**

But still the value of χ^2 is very large. Using these coordinates we can find the corrected value of efficiency i.e. $y_i^{mc}.C_{ij}$. After plotting the experimental values and the corrected values of efficiency, we observe that each crystal has a definite trend of deviation (corrected values from the experimental values) for all the above three cases (Figure 7.57). There is a new parameter (d_i) that arises due to the fact that all the crystals have slightly different absolute efficiency (This is a real effect).

In order to get the values of d_i, we work out the ratio of experimental to corrected values of efficiencies

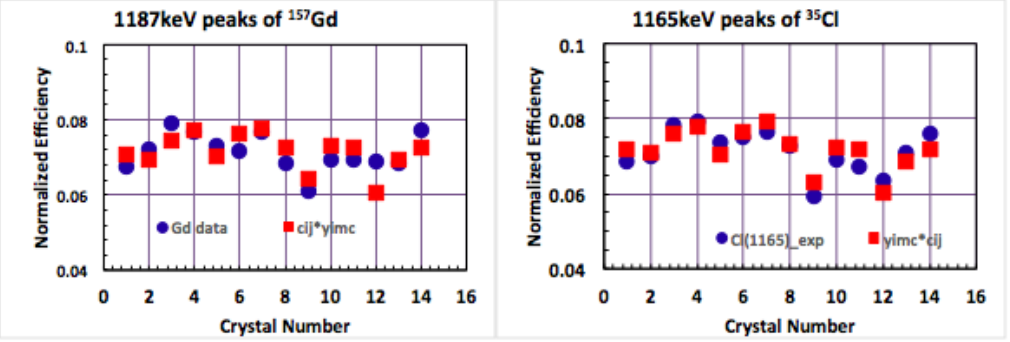

FIGURE 7.57: Normalized efficiency of ^{35}Cl and ^{157}Gd

for each crystal and for all the three cases and get an average. This average term give the value of d_i (listed in Table 7.4).

TABLE 7.4: Absolute efficiency correction factor, di factor for all 14 Ge detectors for different targets

Crystal No.	Cl(1165)	Gd(1186)	Gd(780)	Average(d_i)
1	0.950799507	0.932290101	0.949695187	0.944261598
2	0.991567502	1.013788258	0.992015167	0.999123643
3	1.036976549	1.05626436	1.032944408	1.042061773
4	1.020072694	0.992088044	1.007465037	1.006541925
5	1.048166462	1.03204232	1.030073367	1.036760716
6	0.980183302	0.940220809	0.967678275	0.962694129
7	0.967679393	0.98129623	0.955496488	0.96815737
8	1.001852604	0.955632093	1.020398239	0.992627645
9	0.937422978	0.92682761	0.932739437	0.932330008
10	0.956563398	0.950570862	0.961820891	0.956318384
11	0.939487025	0.955248451	0.945059592	0.946598356
12	1.043928961	1.16354172	1.065057939	1.090842873
13	1.02619027	0.994872653	1.041109792	1.020724238
14	1.05832025	1.060070838	1.068839609	1.062410232

Now, our definition of χ^2 should change.

$$\chi^2 = \sum_{i=1}^{14} \left(\frac{y_i - y_i^{mc}.C_{ij}.d_i.r}{\sigma} \right)^2 + \left(\frac{r+1}{\sigma'} \right)^2 \tag{7.49}$$

where d_i is absolute efficiency Correction factor. Here degree of freedom is 14.

Again compiling the program, we get slightly different coordinates but substantial decrease in the value of χ^2 at **r = 1.0**.

Cl(1165) **(3,-1.5,3.5)** χ^2 **= 9.720**

Gd(1187) **(5.25,-2.25,3)** χ^2 **= 13.445**

Gd(780) **(5,-1.75,4.25)** χ^2 **= 45.699**

Cl(788) **(2,-1.25,3.5)** χ^2 **= 20.523**

Cl(1601) **(4.25,-1.75,3.25)** χ^2 **= 15.578**

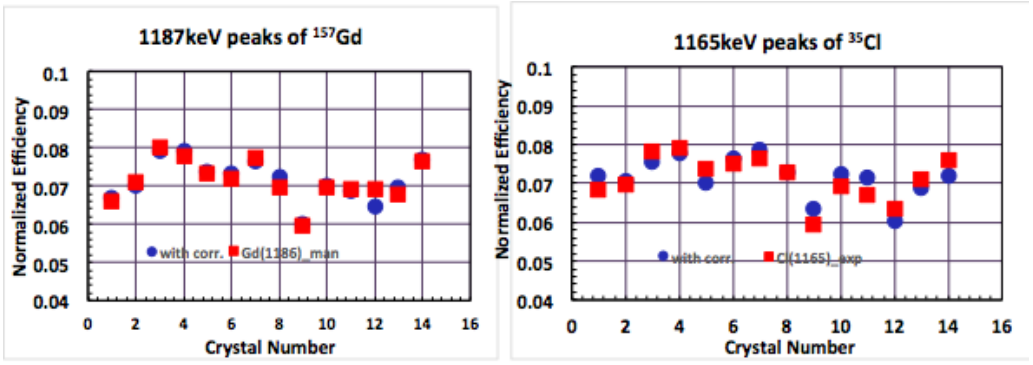

FIGURE 7.58: Normalized efficiency of ^{157}Gd and ^{35}Cl

Figure 7.58 shows the comparison between data and corrected MC for ^{157}Gd and ^{35}Cl. By adding d_i factor, we get very good agreement between data and MC for minimum χ^2. Hence, we get target position by taking average of position for different elements (Cl and Gd) and different peaks.

Error Analysis:

To evaluate the error in each coordinate,(assume Cl(1165) case) plot χ^2 versus x , we get minimum at 3. Draw a line at $\chi^2_{min} + 1$ i.e. at χ^2=10.720; x values corresponding to the point of intersection of line and χ^2 curve give us the error in x (Figure 7.59).

.

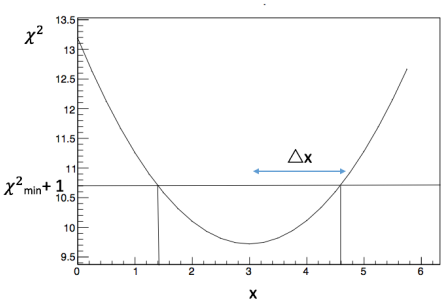

FIGURE 7.59: Error in x Cl(1165)

Similarly we can evaluate the error in y and z.

We can repeat the same procedure to get errors for all the above cases. Figure 7.60 shows that the target position (X,Y,Z) for Gd and Cl for different peaks with errors.

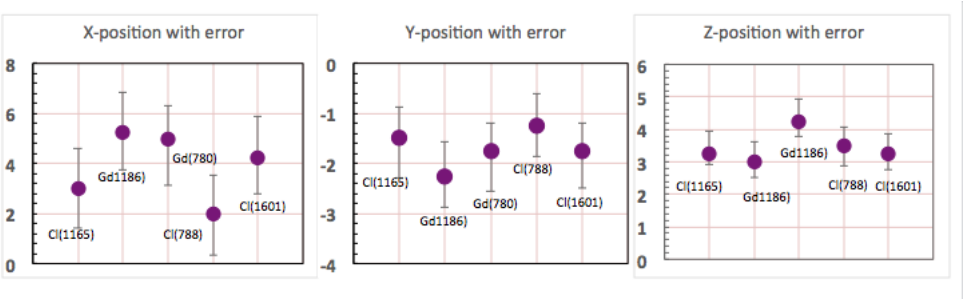

FIGURE 7.60: Position with Errors

Hence we get the center position of the target by averaging the above positions. Hence we get the final position to be (**3.9 ±1.6, -1.7 ± 0.61, 3.5±0.62**) for Gd and NaCl target. Similarly, We got the position for ^{60}Co (**2.375±1.83, 1.75±0.55, 3.875±0.92**)

Chapter 8

Analysis of Discrete Peaks in the γ Rays Spectrum

8.1 γ Rays Spectrum of Thermal Neutron Capture

The incident thermal neutron is captured by the target nucleus in a neutron capture reaction and formed a compound nucleus (CN) with excitation energy. The excitation energy can be explained with the sum of the neutron separation energy and the kinetic energy of the neutron: $E^* = S_n + E_n$ (shown in Figure 8.1). It is well known that the excited CN goes to its ground state by emitting γ ray very shortly (after about $10^{-18} sec$). A number of intermediate states can be formed by the γ-rays from the highly excited compound states. Figure 8.1 shows that the CN (compound nucleus) decays into intermediate

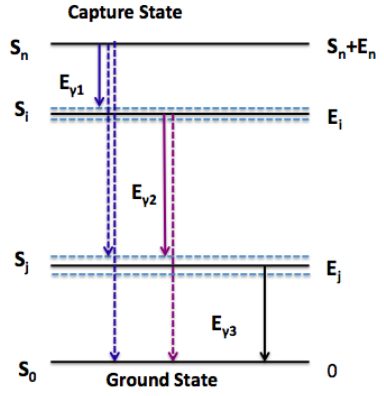

FIGURE 8.1: γ-ray transition from capture CN

energy states S_i by emitting a γ ray with energy $E_{\gamma 1} = (S_n + E_n) - E_i$. The second γ -ray is emitted by transition between the energy states S_i and S_j and the third γ -ray is emitted by energy state S_j to S_0 or ground state are also shown in Figure 8.1.

The resonance nucleus can be transited by decaying γ-rays in two ways. One is continuum and another is discrete (shown in Figure 8.2).

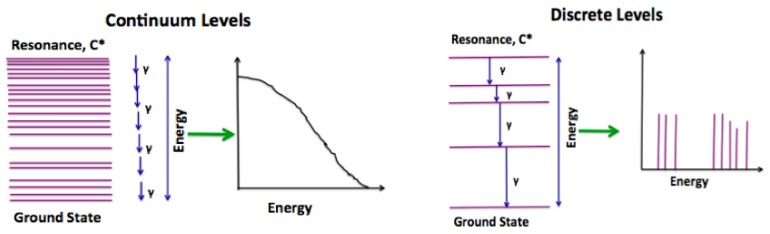

FIGURE 8.2: Continuum and Discrete γ-ray transition from capture CN

8.1.1 Relative Intensity of γ Rays

The intensity of the γ rays is directly proportional to the peak area or number of signals and inversely proportional to the efficiency. i.e,

$$N_{Corr}(i) = \frac{N_{sig}}{\epsilon_{corr}} \tag{8.1}$$

where , N_{sig} is the number of signals. ϵ_{corr} is the corrected detection efficiency.
The corrected detection efficiency can be written as ϵ_{corr}=0.92ϵ_{MC}. where ϵ_{MC} be the photo-peak efficiency from MC(Geant4).
N_{sig} can be written as $N_{sig} = N_{raw} - N_{BG}$, where N_{raw} is the number of raw events of the peaks and N is the background events. N_{raw} was evaluated by the summation of counts in the energy interval

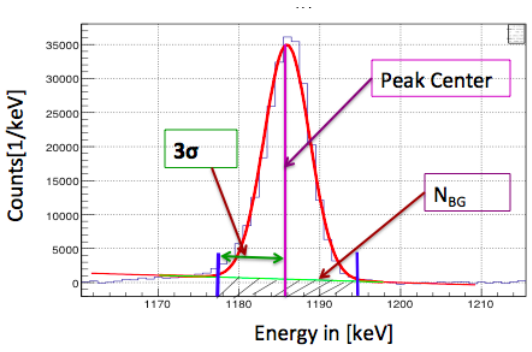

FIGURE 8.3: Photo-peak events estimation

$[E_c - 3\times\sigma, E_c + 3\times\sigma]$, where E_c is the energy of the peak center and σ is the standard deviation of the γ-ray peak. The σ was calculated from the Gaussian fitting. The Gaussian equation can be shown at Eq. 3.12.
Then relative intensity can be written as

$$I_R = (\frac{N_{Corr}(i)}{N_{Corr}(1)}) \times 100\% \tag{8.2}$$

Where $N_{Corr}(1)$ be the number of corrected events of any peaks by which we have normalized the intensity.

8.1.1.1 For Discrete γ-Rays From ^{152}Eu

^{152}Eu disintegrates in three different ways. It disintegrates 72.1% by electron capture , about 0.027% for β^+ or positron emission and about 27.9% by β^- emission.
For electron-capture:

$$^{152}_{63}Eu + e^- \rightarrow ^{152}_{62}Sm^* + \nu_e \tag{8.3}$$

$$^{152}_{62}Sm^* \rightarrow ^{152}_{62}Sm + \gamma \tag{8.4}$$

For Positron emission:

$$^{152}_{63}Eu \rightarrow ^{152}_{62}Sm^* + e^+ + \nu_e \tag{8.5}$$

$$^{152}_{62}Sm^* \rightarrow ^{152}_{62}Sm + \gamma \tag{8.6}$$

This positron can make pair production by colliding with electron.

$$e^+ + e^- \rightarrow 2\gamma\ (511\ keV) \tag{8.7}$$

For β^- decay:

$$^{152}_{63}Eu \rightarrow ^{152}_{64}Gd^* + e^- + \overline{\nu_e} \tag{8.8}$$

$$^{152}_{64}Gd^* \rightarrow ^{152}_{64}Gd + \gamma \tag{8.9}$$

Figure 8.4 shows that the γ ray energy spectrum for ^{152}Eu source. Most of the γ ray photo-peaks are full energy peaks. We calculated the discrete γ photo-peaks only. The γ rays of interest are 121.78, 244.69, 344.28, 367.18, 411.12, 443.96, 488.68, 563.99, 586.26, 678.62, 688.67, 778.9, 867.38, 964.06, 1005.27, 1085.84, 1112.08, 1212.95, 1408.01 and 1528.1 keV.

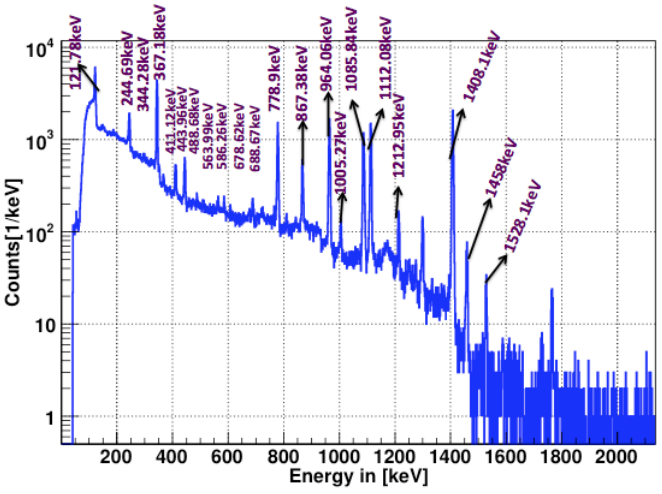

FIGURE 8.4: γ spectrum for ^{152}Eu

The peak area of all the photo-peaks were calculated. The number of signals or peaks area were corrected by photo-peak efficiency. Then the relative intensities of those discrete γ rays was calculated by using the Eq. 8.2. The relative intensities were normalized by the 121.78 keV γ-ray peaks for ^{152}Eu.

Table 8.1 shows that the comparison of relative intensities of discrete γ rays between our data and the values published by Table of Radioactive Isotope [65]. The uncertainties in the Table 8.1 are due to statistical only.

TABLE 8.1: Relative Intensity of γ-rays from ^{152}Eu

Peak Energy (keV)	Relative Intensity ,I_R (%)	
	Our data	Table of Radioactive Isotope [65]
121.78	107.30±1.27	107.30±13.04
244.69	26.14±0.0.76	28.47±1.5
344.28	91.01±0.89	99.49±1.5
367.18	3.83±0.34	3.23±1.5
411.12	8.35±0.33	8.39±1.5
443.96	11.56±0.46	10.59±1.5
488.68	1.98±0.27	1.57±1.5
563.99	1.96±0.32	1.84±1.5
586.26	1.61±0.28	1.72±1.5
678.62	1.65±0.26	1.77±1.5
688.67	3.28±0.29	3.22±1.5
778.9	44.04±0.65	48.58±1.5
867.38	16.04±0.47	15.94±1.5
964.06	54.49±0.65	54.83±1.5
1005.27	3.06±0.31	2.43±1.5
1085.84	43.80±0.65	38.32±1.5
1112.08	52.07±0.65	51.21±1.5
1212.95	5.49±0.29	5.33±1.5
1408.01	76.78±0.77	78.86±1.5
1458	2.64±0.17	1.88±1.5
1528.1	1.09±0.11	1.05±1.5

Then we calculated the ratio of the relative intensities between our data and the values of the table of radioactive isotope shown in Figure 8.5. Our data and the Table of Radioactive Isotope agree about 95%.

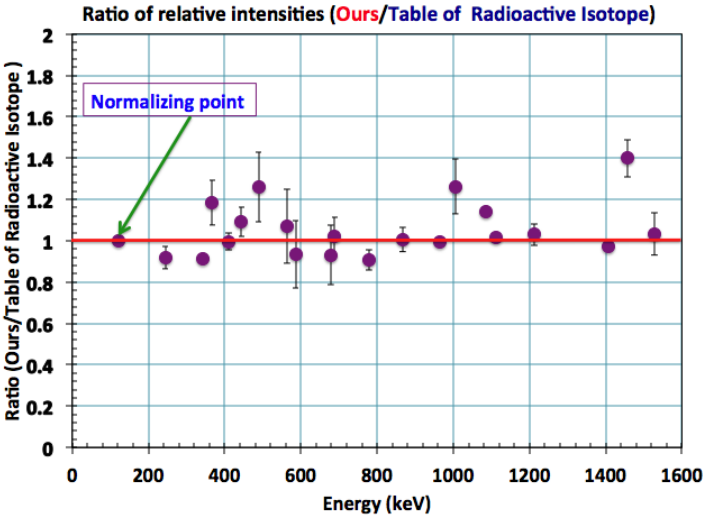

FIGURE 8.5: Ratio between the data and table of isotope values for ^{152}Eu

8.1.1.2 For Discrete γ-Rays From ^{35}Cl(n,γ)

Figure 8.6 shows that the γ ray energy spectrum for ^{35}Cl(n, γ) reaction. Most of the γ ray peaks are full energy peaks. We calculated the prompt γ ray peaks only. The γ rays of interest are 786.3+788.4, 1162.7+1164.9+1171.0, 1327.4, 1601, 1951.1+1959.4, 2676, 2863, 2975, 3061, 3428, 3981, 4440, 4979, 6617, 5715, 5902.7+5913.3, 6110, 6619.6+6627.9+6642.0, 6977, 7414, 7790, and 8578 keV. The relative intensities of those prompt γ rays was calculated by using the Eq. 8.2 The relative intensities were normalized by the 7414 keV γ-ray peaks for ^{35}Cl(n, γ) reaction. Table 8.2 shows that the comparison of relative intensities of prompt γ rays between our data and the values published by NNDC (CapGam) [44] and the values published in Shibata et.al [12]. The ratio (Ours/Table value) has calculated shown in Figure 8.7 and which shows the good agreement between our data and table values. The uncertainties in the Table 8.2 are due to statistical only.

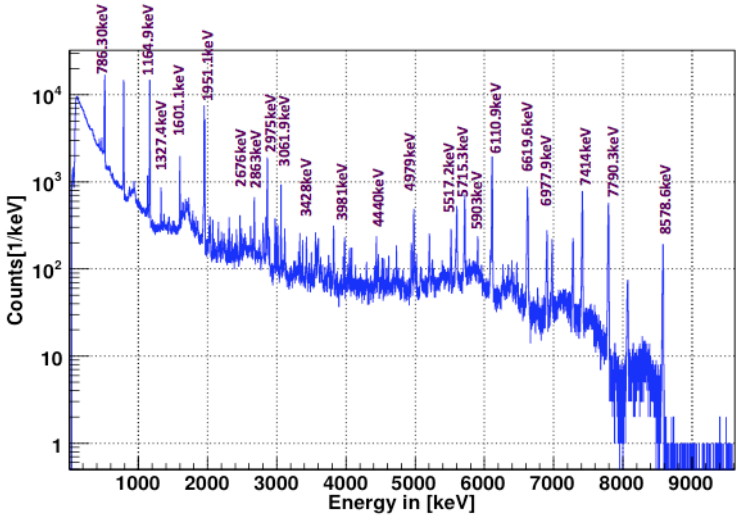

FIGURE 8.6: γ spectrum for ^{35}Cl(n,γ) reaction

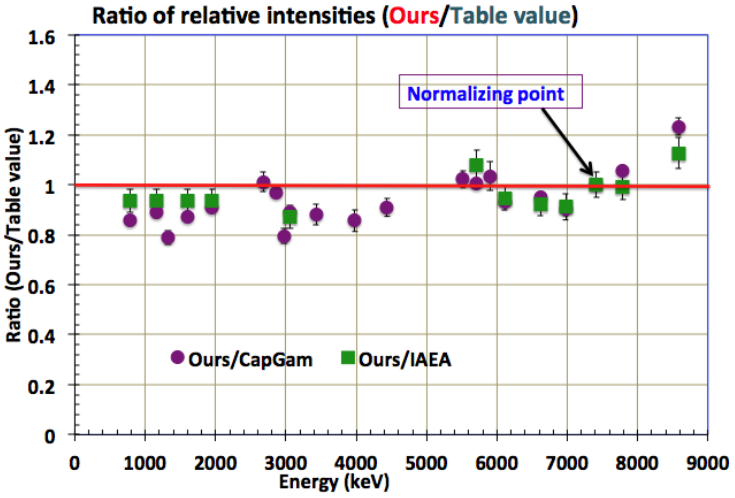

FIGURE 8.7: Ratio of relative intensities (Ours/Table value from the Table 8.2) for ^{35}Cl(n,γ) reaction

TABLE 8.2: Relative Intensity of γ-rays from ^{35}Cl(n,γ) reaction

Peak Energy (keV)	Relative Intensity ,I_R (%)				
	Our data	NNDC (CapGam) [44]	Shibata[12]	IAEA[12]	NNDC[12]
786.30+788.42	230.56±0.84	268.71±0.62	256.5(13)	246(15)	245.9 (58)
1164.9	240.68± 0.90	270.93±2.20	284.9(14)	257 (22)	278.9 (89)
1327.4	9.65±0.35	12.22±0.04	11.58(6)		11.3(7)
1601.1	32.09±0.46	36.87±0.10	35.36(18)	34.3(32)	32.4(12)
1951.1+1959.4	288.31±1.06	317.10±0.94	309.1(15)	308(18)	302.5(70)
2676	16.37±0.39	16.17±0.19			
2863	53.45± 0.60	55.27±0.14			
2975	9.07±0.33	11.41±0.04			
3061.9	30.49±0.46	34.25±0.09	33.56(17)	35(3)	32.6(10)
3428	7.30±0.35	8.29±0.04			
3981	8.70±0.33	10.11±0.08			
4440	10.37±0.39	11.41±0.04			
4979	26.94±0.58	37.47±0.13			
5517.2	17.45±0.54	17.07±0.08	16.48 (18)		
5715.3	55.51±0.88	55.27±0.21	52.99 (54)		
5902.7+5913.3	11.71±0.65	11.33±0.04	11.62 (14)		11.5(5)
6110.9	186.60±1.44	200.41±3.73	196.7 (20)	197(16)	190.1(77)
6619.6+6627.8+6642.0	117.52±1.15	123.44±0.6	123.4 (12)	127.4(76)	128.4 (36)
6977.9	20.34±0.59	22.51±0.12	22.27 (23)	22.3 (2)	21.5 (7)
7414.0	100.0±1.14	100±0.58	100.0 (10)	100.0 (80)	100.0(28)
7790.3	85.43±1.06	80.93±0.36	81.42(82)	86.1 (69)	86.3 (26)
8578.6	33.13±0.72	26.88±0.16	27.30 (26)	29.4 (24)	28.5 (19)

8.1.1.3 For Discrete γ-Rays from ^{157}Gd(n,γ)

Figure 8.8 shows the γ ray energy spectrum for ^{157}Gd(n, γ) reaction. Most of the γ ray peaks are full energy peaks. We calculated the discrete peaks only. The γ rays of interest are 181.94, 780.17, 897.51+897.62, 944.18, 962.12, 977.14, 998.41+1000.82+1004.04, 1107.67, 1119.2, 1184.01+1186+1186+1187.14, 1259.86+1263.51,
1320.5+ 1323.44+1327.18+1329.6+1329.6+1331.34, 1437.96, 4925.2, 5155+5142+5179+5186, 5436.4, 5582.1+5593+5610, 5776.7+5669+5661+5654+5676, 5783.8, 5903.2+5913 , 5995+6006, 6420.1, 6672, 6913, 6960 and 7857 keV. Then, the peak area of all the photo-peaks were calculated. The peaks area

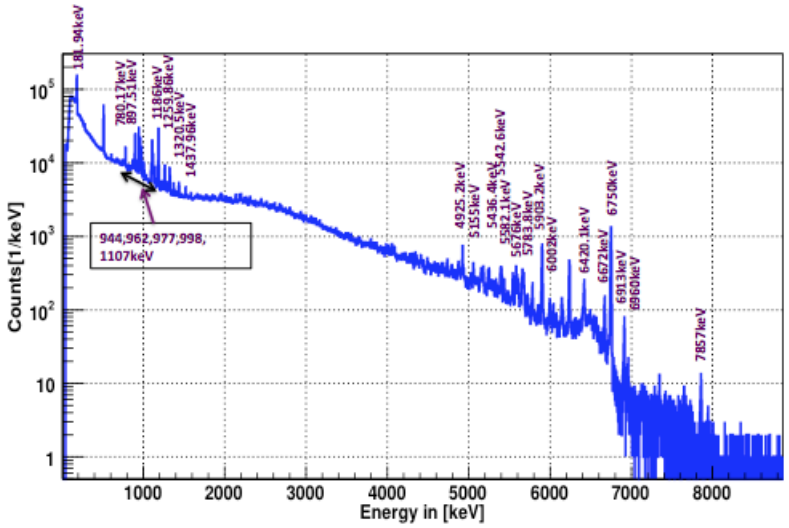

FIGURE 8.8: γ spectrum for ^{157}Gd(n,γ) reaction

or number of signals were corrected by photo-peak efficiency. Then the relative intensities of prompt γ rays was calculated by using the Eq. 8.2 The relative intensities were normalized by the 6750 keV γ-ray peaks for ^{157}Gd(n, γ) reaction. Table 8.3 shows that the comparison of relative intensities of prompt γ rays between our data and the values published by NNDC (CapGam) [44]. Figure 8.9 shows the ratio (Ours/CapGam) for ^{157}Gd(n,γ) reaction. The uncertainties in the Table 8.3 are due to statistical only.

TABLE 8.3: Relative Intensity of γ-rays from ^{157}Gd(n, γ) reaction

Peak Energy (keV)	Relative Intensity ,I_R (%)	
	Our data	NNDC (CapGam)[44]
181.94	641.32±1.87	664.01±86.57
780.17	79.44±0.86	90.57±9.96
897.51+897.62	185.49±1.12	224.57±33.53
944.18	247.39±1.12	309.69±34.20
962.12	153.23±1.04	197.41±21.78
977.14	104.38±0.98	139.84±13.08
998.41+1000.82+1004.04	100.48±1.04	102.92±11.55
1107.67	156.99±0.82	163.35±18.99
1119.2	113.60±0.80	113.02±2.48
1184.01+1186+1187.14	350.18±1.17	381.14±41.90
1259.86+1263.51	89.93±0.88	98.21±10.96
1320.5+1323.44+1327.18+1329.6+1331.34	81.34±0.86	90.17±9.89
1437.96	27.72±0.71	29.35±3.25
4925.2	22.20±0.60	24.63±3.87
5155+5142+5179+5186	25.13±0.39	24.64±3.72
5436.4	7.14±0.44	7.24±0.99
5542.6	9.30±0.45	11.62±1.53
5582.1+5593+5610	33.08±0.56	35.13±2.39
5676.7+5669+5661+5654	29.03±0.63	34.79±4.31
5783.8	9.24±0.40	10.49±1.46
5903.2+5913	49.45±0.65	51.06±5.91
5995+6006	7.02±0.28	8.3±1.33
6420.1	15.22±0.51	13.02±1.86
6672	8.11±0.30	7.97±0.80
6750	100.00±0.03	100.00±9.23
6913	5.72±0.22	5.45±0.60
6960	0.94±0.12	0.73±0.07
7857	0.93±0.12	0.73±0.07

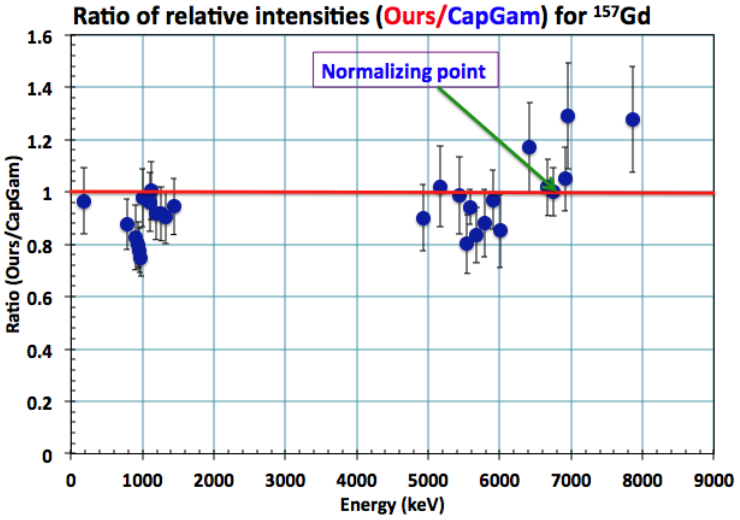

FIGURE 8.9: Ratio (Our data/Table value) for ^{157}Gd(n, γ) reaction

8.1.1.4 For Discrete γ-Rays from ^{155}Gd(n,γ)

Figure 8.10 shows that the γ ray energy spectrum for ^{155}Gd(n, γ) reaction. Most of the γ ray peaks are full energy peaks. We calculated the discrete peaks only. The analysis of discrete γ ray peak was done for the firs time. We have selected the peaks by peak selection method described in Appendix B. The γ rays of interest are 199.58, 261.32 297.37, 316.52, 337.94, 353.53, 459.32, 472.59, 532.77, 567.66, 625.93, 671.65, 715.65, 726.46 779.46, 840.84, 877.89, 897.83, 943.58 959.93, 969.93, 987.82, 1009.34, 1040.08, 1065.44, 1106.86, 1119.76, 1129.93, 1156.38, 1186.38, 1230.7, 1242.49, 1277.53, 1366.73, 1420.93, 1449.46, 1604.86, 1627.16, 1644.56, 1681.77, 1758.05, 1845.07, 1902.21, 1962.39, 2211.78, 2346.61, 3353.29 5349.1, 5588.07, 5661.1, 5699.49, 5836.34, 5919.74, 6034.27, 6193.16, 6236.49, 6278.75, 6319.8, 6348.2, 6429.48, 6483.8, 6621.93, 6707.54, 6871.49, 7217.65, 7261.09, 7289.99, 7383.67 and 8447.73 keV. Then, the peak area of all the photo-peaks were calculated. The

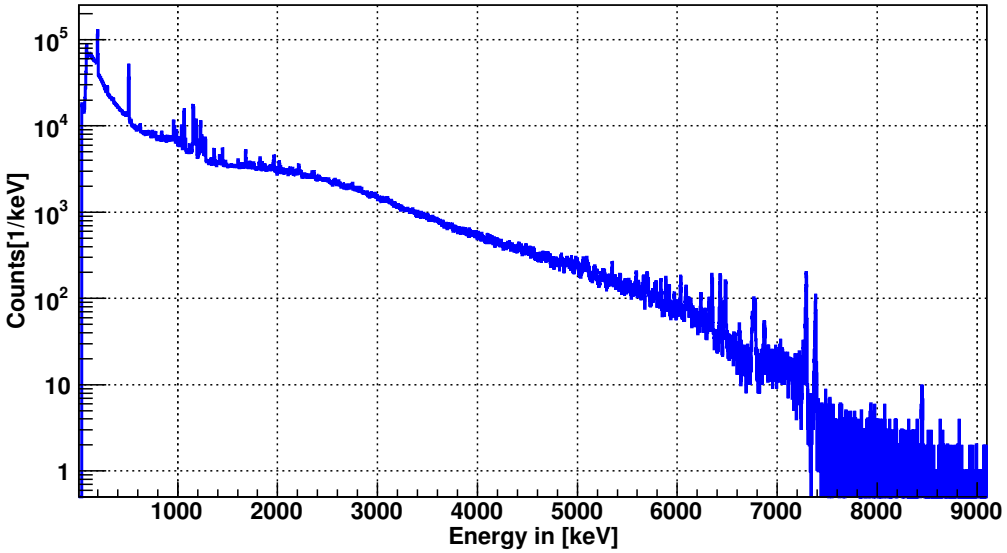

FIGURE 8.10: γ spectrum for ^{155}Gd(n, γ) reaction

peaks area or number of signals were corrected by photo-peak efficiency. Then the relative intensities of those discrete γ rays was calculated by using the Eq. 8.2 The value of relative intensity was normalized by the 199 keV γ-ray peaks. Table 8.4 shows that the relative intensities of discrete γ i.e value of our data. The uncertainties in the Table 8.4 are due to statistical only.

TABLE 8.4: Relative Intensity of γ-rays from ^{155}Gd(n,γ) reaction

Peak Energy (keV)	Relative Intensity,I_R (%) Our data	Peak Energy (keV)	Relative Intensity, I_R (%) Our data	Peak Energy (keV)	Relative Intensity, I_R (% Our data
199.58	100.00±0.25	1040.08	9.54±0.12	5349.1	0.97±0.07
261.32	0.71± 0.02	1065.44	20.01±0.13	5588.07	0.84±0.04
297.37	6.13± 0.16	1106.86	0.68±0.02	5661.1	0.94±0.06
316.52	0.04± 0.005	1119.76	2.18±0.03	5699.49	1.53±0.06
337.94	0.63± 0.017	1129.93	2.21±0.03	5836.34	0.58±0.05
353.53	3.78±0.03	1156.38	34.59±0.16	5919.74	0.64±0.05
459.32	0.65± 0.016	1186.38	15.25±0.13	6034.27	1.15±0.06
472.59	0.57±0.017	1230.7	8.99±0.11	6193.16	0.17±0.023
532.77	1.49± 0.023	1242.49	4.96±0.04	6236.49	0.56±0.03
567.66	0.86±0.018	1277.53	6.05±0.10	6278.75	0.26±0.03
625.93	2.88± 0.11	1366.73	4.18±0.12	6319.8	0.70±0.04
671.65	1.01±0.02	1420.93	2.11±0.11	6348.2	1.73±0.06
715.76	0.87±0.02	1449.46	4.06±0.12	6429.48	1.96±0.06
726.46	1.87±0.024	1604.86	1.32±0.10	6483.8	1.10±0.06
779.46	2.59±0.13	1627.16	0.99±0.02	6621.93	0.23±0.03
815.85	2.63±0.03	1644.56	1.09±0.03	6707.54	0.49±0.03
840.84	2.78±0.11	1681.77	4.57±0.11	6766.1	2.17±0.06
877.89	1.45±0.03	1758.05	2.30±0.03	6871.49	0.55±0.04
897.83	1.35±0.12	1845.07	1.43±0.03	7217.65	0.11±0.02
943.58	1.48±0.03	1902.21	0.38±0.02	7261.09	0.17±0.03
959.93	6.36±0.11	1962.39	5.80±0.13	7289.99	2.55±0.06
969.93	4.84±0.10	2211.78	2.84±0.13	7383.67	1.28±0.04
987.82	4.26±0.10	2346.61	0.95±0.03	8447.73	0.13±0.016
1009.34	2.05±0.11	3353.29	0.57±0.03		

8.2 Modeling for γ Ray Emission

We have used two Monte Carlo (MC) simulations based on Geant4 for γ-ray emission from Gd(n,γ) reaction. First one is the standard option Geant4 [52, 53]. And the second one is a GenericLAND Geant4 simulation (GLG4sim) model [66] which is developed for Kamioka Liquid Scintillator Antineutrino Detector (KamLAND) [67].

We have built our model following the GLG4sim scheme, where the γ rays were classified into two parts: (i) discrete prompt γ rays (ii) continuum spectrum. For prompt γ rays, the relative intensities were estimated from our data for the discrete photo-peaks. We have found that their relative intensities are consistent with the already published values by NNDC (CapGam) within the errors for ^{157}Gd(n,γ) shown in Table 8.3. The relative intensities of prompt γ rays for ^{155}Gd(n,γ) has been measured for the first time measured (shown in Table (8.4). The sum of relative intensities of discrete γ rays is about 2.9% for ^{157}Gd and about 3.8% for ^{155}Gd.

The continuum spectrum can be described in terms of the nuclear level density (NLD) and a set of photon strength functions (PSF). Figure 8.11 shows the emission probability of continuum γ rays for ^{158}Gd. Consider the initial energy level E_a and final energy level E_b. γ rays can be emit from initial to final level with energy E_γ=E_a-E_b.

The transition probability P(E_a,E_b) from the initial energy level to the final level , emitting the γ-rays energy E_γ

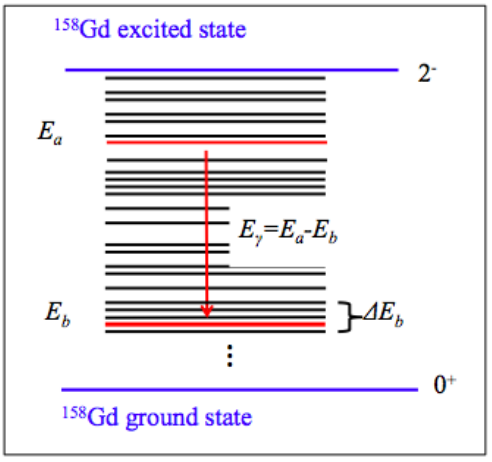

FIGURE 8.11: Emission probability of continuum γ rays

can be written using Fermi Golden Rule as

$$P(E_a, E_b)\Delta E_b = \frac{T(E_\gamma)\rho(E_b)\Delta E_b}{\int_0^{E_a} T(E_\gamma)\rho(E_b)dE_b} \tag{8.10}$$

with T(E_γ) transmission coefficient

$$T(E_\gamma) = 2\pi E_\gamma^3 f(E_\gamma, T) \tag{8.11}$$

where T(E_γ), f(E_γ,T), $\rho(E_b)$ and T are the γ-ray transmission coefficient, photon strength function (PSF), nuclear level density (NLD) and nuclear temperature respectively.

Electromagnetic decay from the neutron resonances is dominated by dipole transitions. The PSFs for the deformed nuclei like Gd are described by the sum of the two Lorentzian terms [68]

$$f(E_\gamma, T) = \sum_{i=1}^{2}[\frac{E_\gamma\Gamma_i(E_\gamma, T)}{(E_\gamma^2 - E_i^2) + E_\gamma^2\Gamma_i^2(E_\gamma, T=0)} + 0.7\frac{\Gamma_i(E_\gamma=0, T)}{E_i^3}]\sigma_i\Gamma_i \tag{8.12}$$

where E_i, Γ_i(E_γ,T), and σ_i are the parameters of the giant electric dipole resonances which have two components (i=1,2). Here, the γ-rays and temperature-dependent width is given by

$$\Gamma_i(E_\gamma, T) = [k_0 + \frac{E_\gamma - \epsilon_0^\gamma}{E_i - \epsilon_0^\gamma}(1-k_0)]\frac{\Gamma_i}{E_i^2}(E_\gamma^2 + 4\pi^2T^2) \tag{8.13}$$

and guarantees Γ_i(E_γ,0)=Γ_i. We used the parameters from the database of RIPL-2 [69]. The Hartee-

TABLE 8.5: γ rays Strength function for ^{156,158}Gd

Isotope	Energy, $E_{1,2}$ (MeV)	Cross-section, $\sigma_{1,2}$ (mb)	Level width,$\Gamma_{1,2}$ (MeV)
^{156}Gd	11.2	180.0	2.6
	15.2	242.0	3.6
^{158}Gd	11.7	165.0	2.6
	14.9	249.0	3.8

Fock-Bugliubov (HFB) model was also used NLD in the database of RIPLE-3 [70].

We compared the γ rays generated by the model with our data, as shown in Figure 8.12 and Figure 8.13. We obtained the fraction of the continuum to be 97.1% for ^{157}Gd , 96.2 % for ^{155}Gd and that of discrete γ rays to be 2.9 % for ^{157}Gd and 3.8 % for ^{155}Gd.

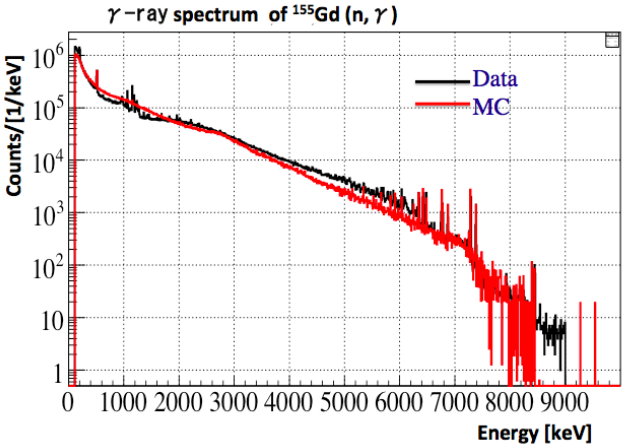

FIGURE 8.12: Energy spectrum for single γ rays from ^{155}Gd(n,γ)

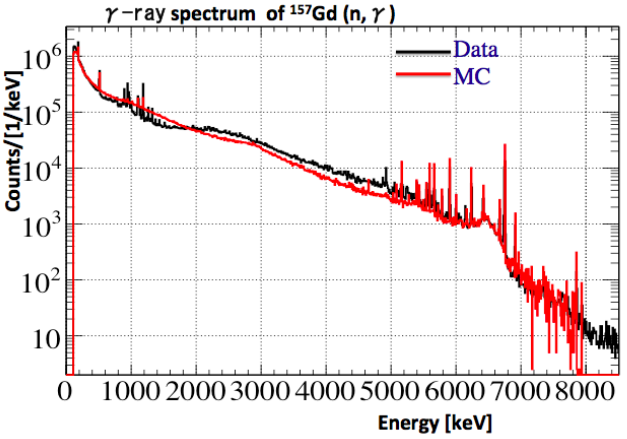

FIGURE 8.13: Energy spectrum for single γ rays from ^{157}Gd(n,γ)

The γ rays below 5 MeV energy region is dominated by continuum spectrum. We also note that the contribution of prompt γ rays (including their Compton scattering) to the total spectrum is very small, except for the energy region above 5 MeV, as shown in Figures 8.12 and 8.13. The agreement between our data and our model is within $\pm$40%.

Chapter 9

Discussions and Conclusion

The properties of Gd nucleus and the previous experiments of Gd (n,γ) experiments have been reviewed. An experiment was conducted to measure the energy of γ-rays from the thermal neutron reaction on enriched gadolinium targets (^{155}Gd and ^{157}Gd isotopes). The experiment was performed using Accurate Neutron-Nucleus Reaction Measurement Instrument (ANNRI) Germanium Spectrometer at Material and Life Science Experimental facility (MLF) of the Japan Proton Accelerator Research Complex (JPARC), which provides the most intense pulse neutron beam for neutron time-of-flight experiments in the world. The purposes of our experiments and analysis are to provide precise γ-ray spectrum of ^{155,157}Gd(n, γ) reactions and provide precise Gd decay model to neutrino physics field and other related fields.

We measured the γ rays produced from the ^{155,157}Gd(n,γ) reactions in the thermal energy region with the superior energy resolution of ANNRI Ge spectrometer. The background was measured by using empty target (target holder only) and it was estimated to be negligible (about 0.1%). The photo-peak efficiency of the spectrometer has been calibrated from 0.1 to 9 MeV using the standard radioactive sources (^{60}Co, ^{137}Cs and ^{152}Eu) and the prompt γ rays from ^{35}Cl(n,γ) reaction. The photo-peak efficiency of the spectrometer from 0.1 to 9 MeV was understood within $\pm 10\%$ accuracy.

Our data of relative intensities of prominent discrete γ rays from ^{157}Gd(n,γ) reactions are in good agreement with the values published by the Nuclear National Data Center (NNDC) (CapGam). The relative intensities of discrete γ rays from ^{155}Gd(n,γ) reaction have been measured for the first time. The accuracy of our result from the γ-ray spectrum measurement for our thermal neutron capture experiments should be better than others, as we used the most intense pulsed neutron beam and used Germanium spectrometer with high energy resolution.

We have also built a γ-ray emission model of ^{156,158}Gd decay, in which γ rays were classified into discrete prompt γ rays and continuum spectrum. The γ-ray emission model of ^{156}Gd decay has been

built for the first time. We have compared the data and our model, and found a fair agreement between them (shown in Figure 9.1 and Figure 9.2). This γ emission model of ^{156}Gd and ^{158}Gd will help us to generate γ emission model for natural gadolinium (^{nat}Gd).

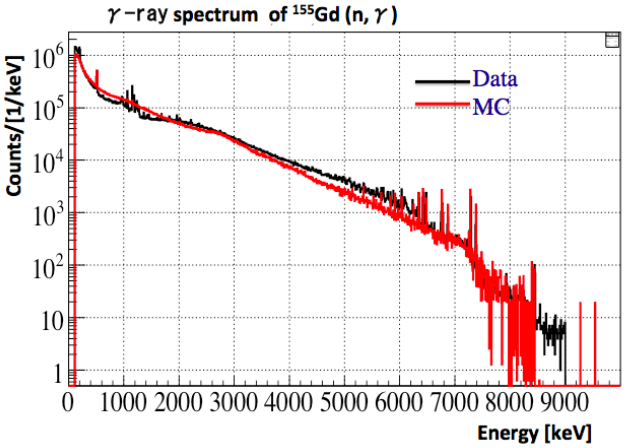

FIGURE 9.1: Energy spectrum for single γ rays from ^{155}Gd(n,γ)

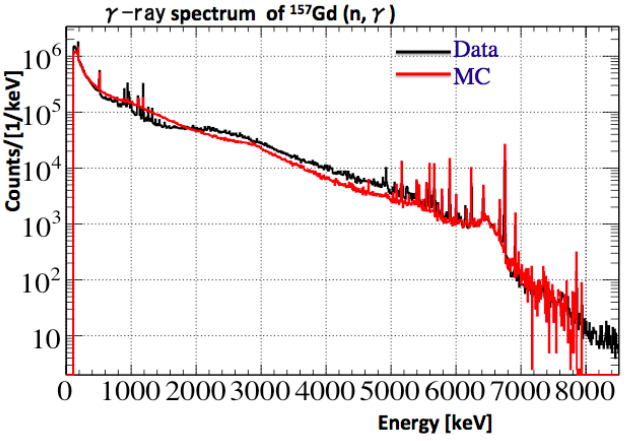

FIGURE 9.2: Energy spectrum for single γ rays from ^{157}Gd(n,γ)

We can compare our model with the currently used model for neutrino physics community. The model usually used is GLG4sim model and which was developed by Kamioka Liquid Scintillator Antineutrino Detector (KamLAND). Figure 9.1 shows the comparison between our data and the two models (GLG4sim model and our model) for ^{157}Gd(n,γ) reaction . Compared to GLG4sim, the agreement of our data and our model in the energy region between 0.1 to 8 MeV was improved by a factor three [71]. We have also identified more discrete peaks (about 15 peaks) in modeling than GlG4sim (6 peaks).

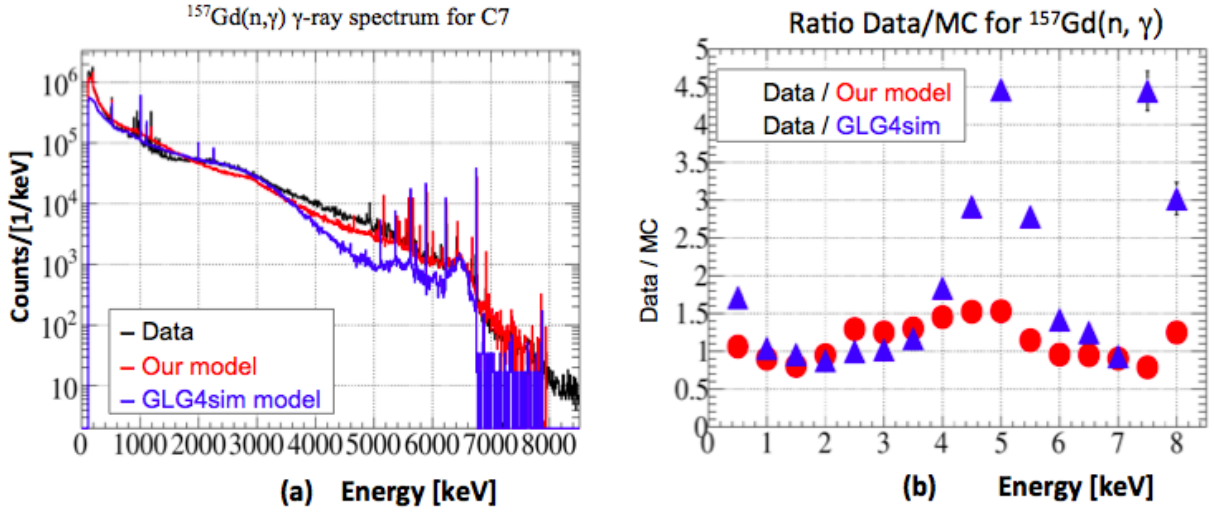

FIGURE 9.3: (a) Comparison of γ spectrum for ^{157}Gd(n,γ) reaction (b) Comparison of the ratio data/MC for ^{157}Gd(n,γ) reaction

In summary, we measured the γ rays produced from the ^{155,157}Gd(n,γ) reactions in the thermal energy region with the superior energy resolution of the ANNRI spectrometer with good accuracy. The photo-peak efficiency of the spectrometer has been calibrated from 0.1 to 9 MeV using γ rays from the radioactive sources (^{60}Co, ^{137}Cs, ^{152}Eu) and the prompt γ rays from ^{35}Cl(n, γ) reaction. The relative intensities of prominent discrete γ rays produced from ^{155}Gd(n,γ) and ^{157}Gd(n, γ) reactions were measured. Our data of relative intensities from ^{157}Gd(n, γ) were found in fair agreement with the previously published values. The relative intensities of prominent discrete rays from ^{155}Gd(n, γ) reaction were measured for the first time with good accuracy.

Appendix A

Photo-peak efficiency

A.1 Determination of C-factor

From section 7.1.2.2 we can get the number of events of γ_1 for detector A as

$$N_1^A = \beta T r_L^A \eta_1^A \epsilon_1^A (1 - C) \tag{A.1}$$

where C is the correction for the veto counter (BGO) trigger.
We have analysed the data set of ^{60}Co including the veto for measurement of the photo-peak efficiency. For this we need the correction for the veto counter trigger or C factor in our calculation. We have used the χ^2 formula from section 7.1.2.2 (using Eq. 7.28) as

$$\begin{aligned}\chi^2 = (\frac{N_1^A - abh(1-C)}{\sigma_1})^2 + (\frac{N_2^A - ach(1-C)}{\sigma_2})^2 (\frac{N_1^B - adi(1-C)}{\sigma_3})^2 + \\ (\frac{N_2^B - aei(1-C)}{\sigma_4})^2 + (\frac{N_3 - abefj}{\sigma_5})^2 + (\frac{N_4 - acdfj}{\sigma_6})^2\end{aligned} \tag{A.2}$$

We have determined βT for different C-values. The product βT is composed of β, which is the activity of the radioactive material (nominal activity), and T, which is the measurement time.

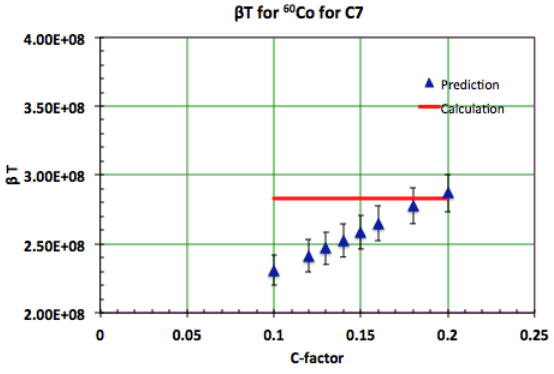

FIGURE A.1: βT calculation for different C-values for the veto

Then we have compared the predicted value of βT with the calculated value. Figure A.1 shows the comparison of βT for prediction and calculation for different C-value. One can see that at C=0.20 we get a good agreement between the predicted and calculated value of βT (shown in Figure A.1).

We can check our C-value calculation with other data sets. We have analysed data for non-veto (without BGO counter) case. Similar to the veto case, we have calculated the βT for different C-values using the Eq. A.2. We have found that the βT value for prediction and calculation are in good match at C=0.0 (shown in Figure A.2). Therefore, there is no need for any correction to the veto. We can conclude that we need to add a correction for veto counter trigger if we use the data with veto counter. The value of C is 0.20.

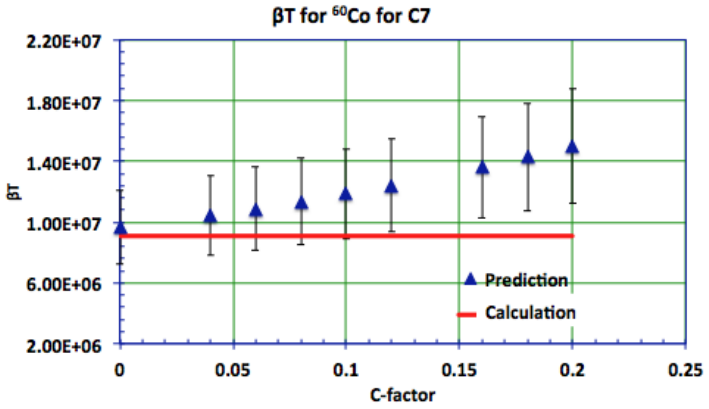

FIGURE A.2: βT calculation for different C-value for non-veto

A.1.1 Determination of C-factor from MC(Geant4)

We have analysed the MC data set of ^{60}Co with the veto counter for the photo-peak efficiency determination. So, we need to use the correction for the veto counter trigger in our calculation. We have used the χ^2 formula from Eq. 7.39 as

$$\chi^2 = (\frac{N_1^A - ab(1-C)}{\sigma_1})^2 + (\frac{N_2^A - ac(1-C)}{\sigma_2})^2 (\frac{N_1^B - ad(1-C)}{\sigma_3})^2 + (\frac{N_2^B - ae(1-C)}{\sigma_4})^2 + (\frac{N_3 - abe}{\sigma_5})^2 + (\frac{N_4 - acd}{\sigma_6})^2 \quad \text{(A.3)}$$

We have determined βT or a value for different C-values.

Then we have compared the predicted value of βT with the calculated value. Figure A.3 shows the comparison of βT for prediction and calculation for different C-value. Here, we can see that at C=0.22 we get a good agreement between the predicted and calculated value of βT (shown in Figure A.3). Which means at C=0.22 we get nominal value of activity from prediction.

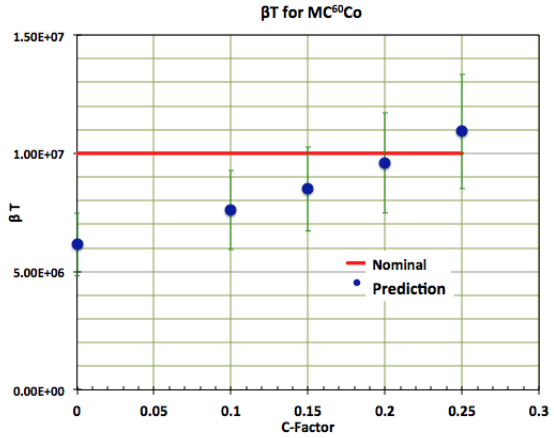

FIGURE A.3: βT calculation for different C-value for MC

A.2 Measurement of Photo-Peak Efficiency

We have determined the absolute photo-peak efficiency using ^{60}Co data and MC(Geant4) as well as relative photo-peak efficiencies form the radioactive source ^{152}Eu and the ^{35}Cl(n,γ) reaction. Then, we have calibrated the relative efficiencies with the absolute efficiencies. We have understood well within $\pm 10\%$ from 0.2 MeV to 9 MeV energy region.

Figure A.4 shows the calibrated photo-peak efficiencies for the upper cluster (Crystal number C1 to C7, where C7 is the center of the upper cluster)

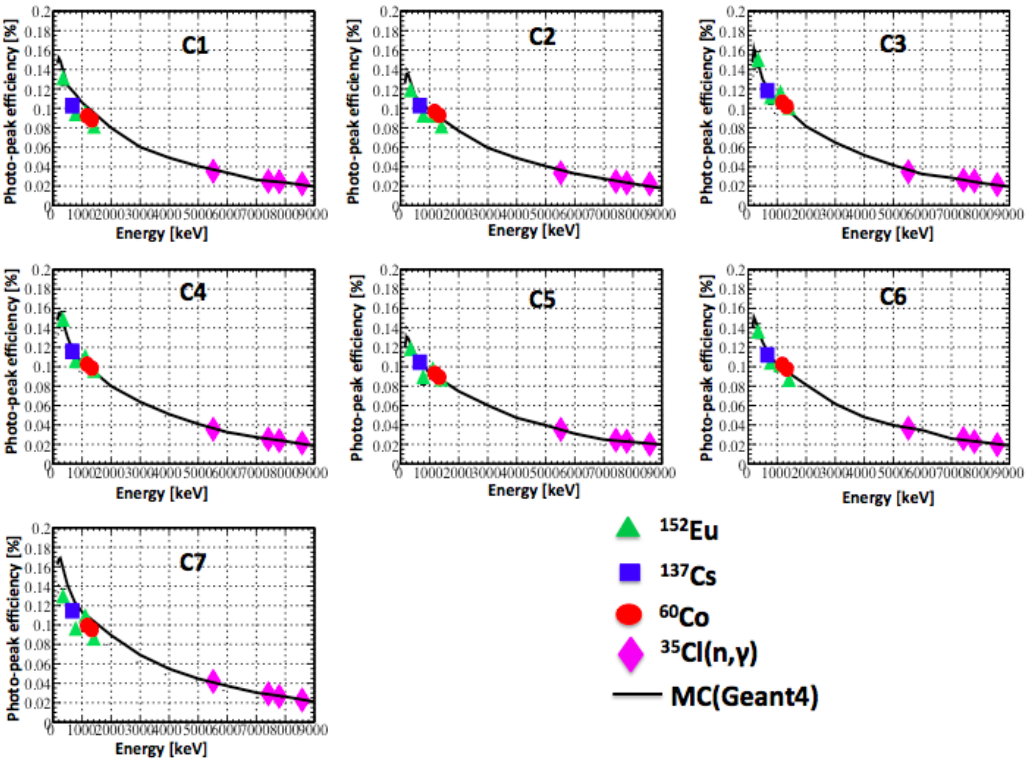

FIGURE A.4: Photo-peak efficiencies for the upper cluster

Figure A.5 shows the calibrated photo-peak efficiencies for the lower cluster (crystal number C8 to C14, where C14 is the center of the lower cluster)

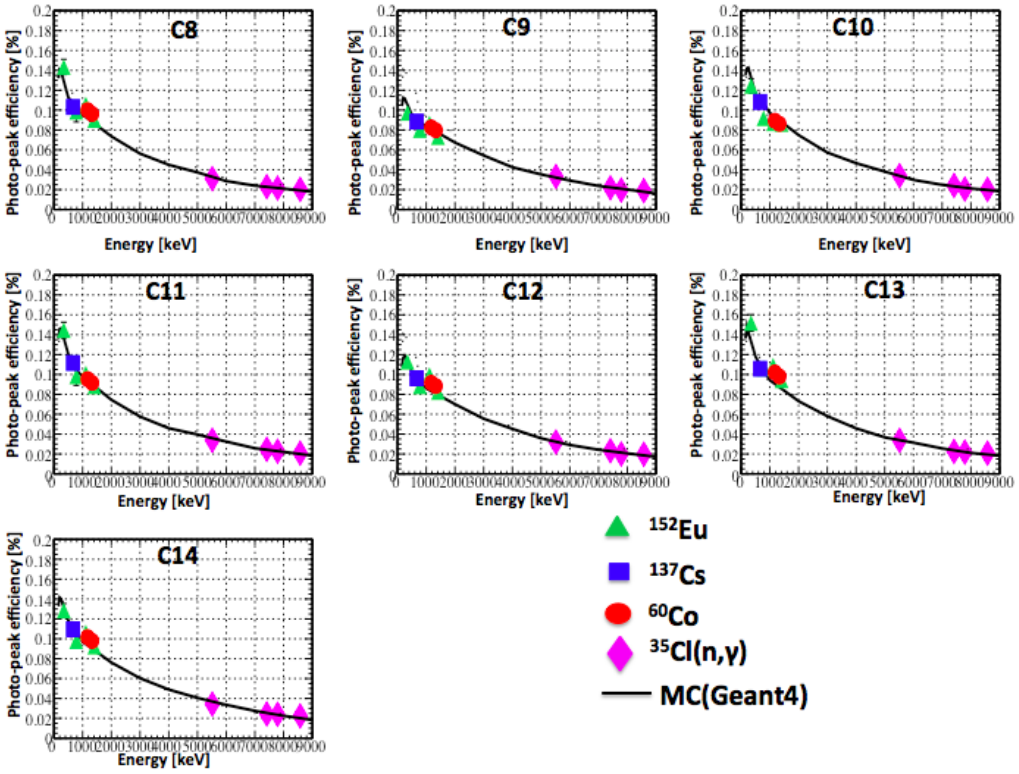

FIGURE A.5: Photo-peak efficiencies for the lower cluster

A.3 Measurement of the Energy Resolution

Figure A.6 shows the energy resolution for the upper cluster

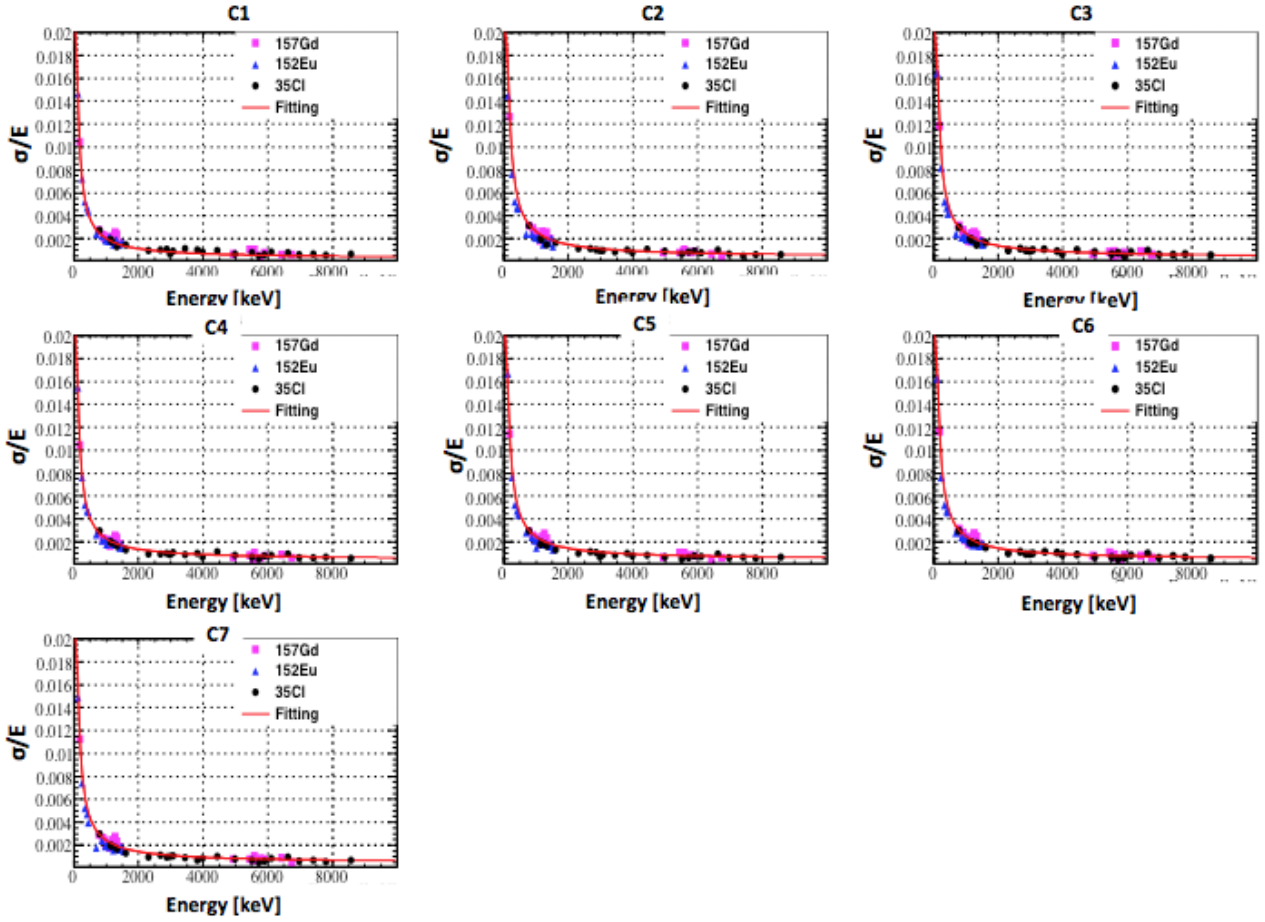

FIGURE A.6: Energy resolution of the upper cluster

Figure A.7 shows the energy resolution for the lower cluster.

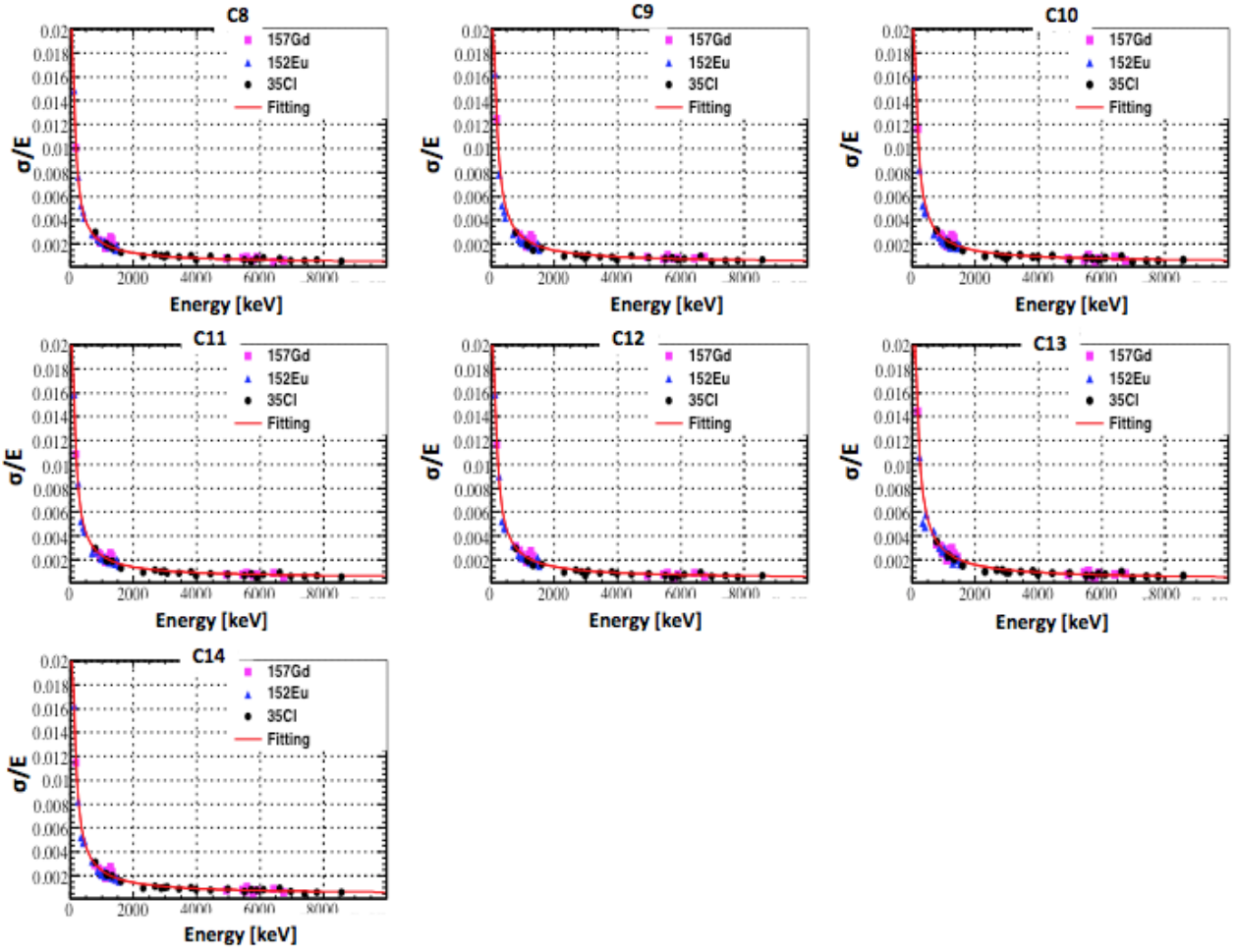

FIGURE A.7: Energy resolution for the lower cluster

A.4 Measurement of the Target Position

From section 7.5 we can get the χ^2 formula as

$$\chi^2 = \sum_{i=1}^{14} \left(\frac{y_i - y_i^{mc}.C_{ij}.r}{\sigma} \right)^2 + \left(\frac{r-1}{\sigma'} \right)^2 \tag{A.4}$$

where y_i is the experimental value,

y_i^{mc} is the Monte Carlo (MC) value,

C_{ij} is the 3-D Correction Factor,

r is the common normalization factor,

σ' = 0.02, (2% error) and

σ = 0.02×(1/14)=0.00143, The total number of degrees of freedom is 14.

A.4.1 Total Error Estimations

We have taken about 2% total errors originating from the systematic error due to the background subtraction and from the statistical error while counting the number events of peaks. The total error can be written as

$$\sigma_T = \sqrt{(\sigma_{stat})^2 + (\sigma_{syst})^2} \tag{A.5}$$

where σ_{stat} is the statistical error and σ_{syst} is the systematic error.
The statistical error, σ_{stat} can be written as

$$\sigma_{stat} = \sqrt{N_t} \tag{A.6}$$

where N_t is the total number of events.
The total number of event is sum of the signal event and number of background event. Which can be written as

$$N_t = N_{sig} + N_{BG}. \tag{A.7}$$

where N_{sig} is the number of signal subtracted from background and N_{BG} is the background event.
The statistical error in percentage (%) can be written as

$$\sigma_{stat} = \frac{\sqrt{N_t}}{N_{sig}} \times 100\% \tag{A.8}$$

The systematic error, σ_{syst} can be written as

$$\sigma_{syst} = \frac{(\Delta N)}{N_{method2}} \times 100\% \tag{A.9}$$

where ΔN=($N_{method2}$)-($N_{method1}$). $N_{method1}$ is the number of events counted from method-1 (shown in Figure A.8 and $N_{method2}$ is the number of events counted from method-2 (shown in Figure A.9). From

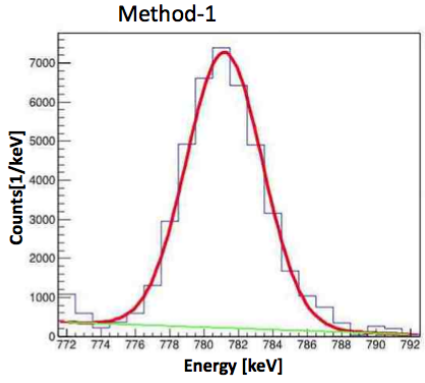

FIGURE A.8: Number of photo-peak event in method 1

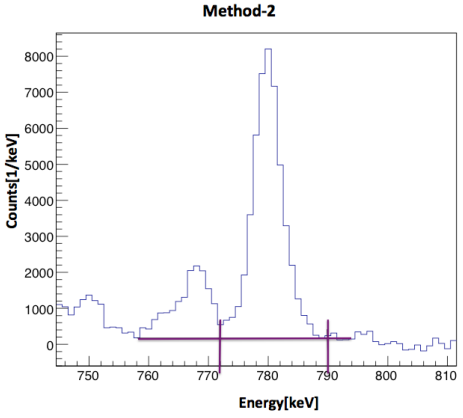

FIGURE A.9: Number of photo-peak event in method 2

this analysis, we have found that the total error while counting the number of events of a photo-peaks is about 2%.

A.5 Angle between the Ge detector

The co-ordinates of the center of all the Ge detectors were calculated. Then, the unit vectors of all the detectors passing through the center were calculated. Suppose, the radial vector from (0,0,0) position to center of crystal, C1 be $\vec{r_1}$ and can be written as

$$\vec{r_1} = 53.25\hat{i} + 30.75\hat{j} + 134\hat{k} \tag{A.10}$$

Then, the unit vector of C1 can be written as $\hat{n_1} = 0.3612\hat{i} + 0.2086\hat{j} + 0.9088\hat{k}$. Similarly the unit vector of C7 is $\hat{n_7} = 1\hat{k}$.
Then, the angle between C1 and C7 detector is given by

$$cos\theta_{17} = \hat{n_1}.\hat{n_7} = 0.9088 \tag{A.11}$$

where θ_{17} is the angle between the detector 1 and detector 2. Then angle we get, $\theta_{17} = 24.67\,\mathrm{deg} \approx 24.7\,\mathrm{deg}$.
Similarly, the angle between all the pair of detectors were calculated.

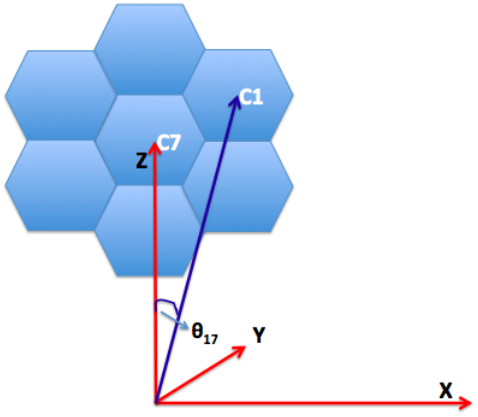

FIGURE A.10: Angle between the detectors of ANNRI

TABLE A.1: Angle between all the Ge-counters of ANNRI.

Ge-counter	Angle in [deg]													
	C1	C2	C3	C4	C5	C6	C7	C8	C9	C10	C11	C12	C13	C14
C1	0	24.1	42.4	49.3	42.4	24.1	24.7	137.6	155.9	180	155.9	137.6	130.7	155.3
C2	24.1	0	24.1	42.4	49.3	42.4	24.7	155.9	180	155.9	137.6	130.7	137.6	155.3
C3	42.4	24.1	0	24.1	42.4	49.3	24.7	180	155.9	137.6	130.7	137.6	155.9	155.3
C4	49.3	42.4	24.1	0	24.1	42.4	24.7	155.9	137.6	130.7	137.6	155.9	180	155.3
C5	42.4	49.3	42.4	24.1	0	24.1	24.7	137.6	130.7	137.6	155.9	180	155.9	155.3
C6	24.1	42.4	49.3	42.4	24.1	0	24.7	130.7	137.6	155.9	180	155.9	137.6	155.3
C7	24.7	24.7	24.7	24.7	24.7	24.7	0	155.3	155.3	155.3	155.3	155.3	155.3	180
C8	137.6	155.9	180	155.9	137.6	130.7	155.3	0	24.1	42.4	49.3	42.4	24.1	24.7
C9	155.9	180	155.9	137.6	130.7	137.6	155.3	24.1	0	24.1	42.4	49.3	42.4	24.7
C10	180	155.9	137.6	130.7	137.6	155.9	155.3	42.4	24.1	0	24.1	42.4	49.3	24.7
C11	155.9	137.6	130.7	137.6	155.9	180	155.3	49.3	42.4	24.1	0	24.1	42.4	24.7
C12	137.6	130.7	137.6	155.9	180	155.9	155.3	42.4	49.3	42.4	24.1	0	24.1	24.7
C13	130.7	137.6	155.9	180	155.9	137.6	155.3	24.1	42.4	49.3	42.4	24.1	0	24.7
C14	155.3	155.3	155.3	155.3	155.3	155.3	180	24.7	24.7	24.7	24.7	24.7	24.7	0

Appendix B

Analysis of Discrete Photo-Peaks

B.1 Selection of photo-peak

We have selected the photo-peaks by their significance. We have fitted the photo-peak by Gaussian and polynomial function.

$$F(x) = A_0 e^{-\frac{(x-A_1)^2}{2A_2^2}} + A_3 + A_4 x \tag{B.1}$$

where first term is the Gaussian function, 2nd and 3rd term are polynomial function.
Polynomial function will subtract the background.
The Gaussian function,

$$f(x) = A_0 e^{-\frac{(x-A_1)^2}{2A_2^2}} \tag{B.2}$$

where A_0 is the peak height, A_1 is the peak center and A_2 is the standard deviation of Gaussian function (which is known as σ).

Polynomial function,

$$Pol1(3) = A_3 + A_4 x \tag{B.3}$$

where A_3 is the starting point of the peak and A_4 is the ending point of the peak.

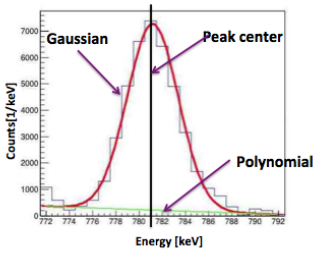

FIGURE B.1: Gaussian fitting of peak

We have tuned all the peaks from 100keV to 9 MeV and calculated A_0 for all the possible peaks and

error of A_0 is σ_0.

TABLE B.1: Selection of photo peak from γ-rays from ^{155}Gd(n,γ) reaction

Energy	A_0	σ_0	A_0/σ_0	Energy	A_0	σ_0	A_0/σ_0
199.58	85737	168	510.34	1644.56	463	12	38.58
261.32	696	16	43.5	1681.77	1927	22.8	84.52
296.37	5662	40	141.55	1758.05	585.8	11.99	48.86
316.52	93	6.8	13.68	1845.07	724.6	13.91	52.09
337.94	383	14	27.36	1902.21	186.33	6.83	27.28
355.76	1946	21	92.67	1962.39	1787	20.16	88.64
459.32	576	12	48	2111.58	284.1	7.9	35.96
472.59	453	15	30.2	2346.61	267.3	8.53	31.34
532.77	974	17	57.29	3353.29	93.8	3.9	24.05
567.78	591	12	49.25	5349.10	87.20	3.43	25.42
625.93	2002	21	95.33	5588.03	69.31	2.6	26.56
671.65	728	13	56	5661.64	84.88	2.75	30.86
715.76	463	18	25.72	5699.49	97.92	3.41	28.72
726.47	1131	18	62.83	5836.34	44.21	2.01	21.99
779.27	1642	18.5	88.76	5884.72	82.62	3.16	26.15
815.85	789	13.5	58.44	5919.74	62.01	3.42	18.13
840.83	1907	20.1	94.88	6034.27	112	4.55	24.62
877.89	890	16.3	54.60	6193.16	11.61	2.09	5.56
897.83	972	15.1	64.37	6236.49	55.75	2.86	19.49
943.58	799	16.5	48.42	6278.75	12.88	2.24	5.75
959.93	4638.2	41.8	110.96	6319.8	52.52	2.51	20.92
969.97	3062	38.7	79.12	6348.2	162.4	4.32	37.59
987.85	2816	24.6	114.47	6430.07	173.0	4.47	38.70
1009.34	1393	19.5	71.44	6483.8	115	4.95	23.23
1040.08	4976	33.66	147.83	6621.93	20.66	1.70	12.15
1065.4	11677	51.8	225.42	6707.54	10.88	1.23	8.85
1106.85	449.9	10.8	41.66	6766.1	190	5.3	35.85
1119.76	1342	17.4	77.13	6871.49	38.8	2.16	17.96
1129.95	1114	16	69.63	7217.65	10.76	1.65	6.52
1156.38	13302	49.01	271.41	7261.09	18.68	2.22	8.41
1186.45	5976	47.6	125.55	7289.99	238.8	6.79	35.17
1230.7	6321	52.7	119.94	7383.67	130.2	4.93	26.41
1242.49	2952	37.1	79.57	8447.73	5.85	0.98	5.96
1277.53	3377	31.91	105.83				
1366.27	2173	21.5	101.07				
1420.93	1056	16.67	63.35				
1449.46	2152	22.17	97.07				
1604.86	672.3	11.99	56.07				
1627.16	499.7	11.00	45.43				

We have selected the photo-peak by using the value of A_0/σ_0. A peak is called as a photo-peak if it has $A_0/\sigma_0 > 5.0$.

Appendix C

Publications List

Refereed papers:

1 . Pretam Kumar Das, K. Hagiwara,T. Tanaka, Y. Yamada, I. Ou, M.S. Reen, T. Yano, T. Mori, T. Kayano, R. Dhir, Y. Koshio, M. Sakuda, A. Kimura, N. Iwamoto, S. Nakamura and H. Harada "Measurement of the relative intensities of the discrete γ rays from the thermal neutron capture reaction ^{155,157}Gd(n, γ) using ANNRI detector (JPARC)" in proceeding of The 3rd International Symposium on Quest for the Origin of Particle and the Universe PoS (KMI 2017) 045.

Other paper:

1. Kaito Hagiwara, T. Tanaka, P. K. Das T. Yano, Y. Yamada, I. Ou, T. Mori, T. Kayano, M.S. Reen, R. Dhir, Y. Koshio, M. Sakuda, A. Kimura, S. Nakamura, N. Iwamoto and H. Harada "Comparison of γ production data from thermal neutron capture on gadolinium with the Monte Carlo simulation" in proceeding of The 3rd International Symposium on Quest for the Origin of Particle and the Universe, PoS (KMI2017) 035.

Poster:

1. Pretam Kumar Das "Measurement of relative intensities of the discrete γ-rays from the thermal neutron capture reaction ^{155,157}Gd(n,γ) using ANNRI detector(JPARC)", at the 3^{rd} international symposium on "Quest for origin of Particles and Universe", Nagaoya University, ES Hall, January 5-7, 2017, Nagaoya, Japan.

2. Pretam Kumar Das "Measurement of relative intensities of the discrete γ-rays from the thermal neutron capture reaction ^{155,157}Gd(n,γ) using ANNRI detector(JPARC)" at the workshop on "Revealing the history of the universe with underground particle and nuclear research, Okayama University", May 21-23, 2017, Okayama, Japan.

Oral presentation:

1. Pretam Kumar Das "Measurement of the relative intensities of the discrete γ rays from the thermal neutron capture reaction ^{155,157}Gd(nγ) using ANNRI detector (JPARC)", JPS meeting, March 18, 2017, Osaka University, Japan.

Bibliography

[1] J. M. Blatt, V. F. Weisskopf *Theretical Nuclear Physics, John Willey and sons*(**Seventh edition, 1963**).

[2] H. Feshbach, C.E. Porter, V.F. Weisskopf, *Phys. Rev.* **96**, 448 (1954).

[3] E. Fermi , E . Amaldi et al.,*Proc. Roy. Soc. A***146**, 483(1934).

[4] H. A. Bethe, *Phys. Rev.* **47**, 747 (1935).

[5] T. Hayakawa et al., EPJ Web Conferences. **122**, 05003 (2016).

[6] E. Margaret Burbidge et al.,*Rev Mod Phys.***29**, 547 (1957).

[7] S. F. Mughabghab, *Altas of Neutron Resonances ,Elsevier* **(5th edition, 2006)**.

[8] H. D. Choi et al., Nuclear Science and Engineering **177**, 219-232 (2014).

[9] K. Shibata et al., *J. Nucl. Sci. Technol.***48(1)**,1 (2011).

[10] G. Leinweber et al., Nuclear Science and Engineering **154**, 261-279 (2014).

[11] Nuclear Data Center, JAEA, < http://wwwndc.jaea.go.jp/ >.

[12] M. Shibata , A. Tojo et al., *Applied Radiation and Isotopes* **'3**, 60(2013).

[13] J. F. Beacom and M. R. Vagins, Phys. Rev. Lett **93**, 171101(2004).

[14] H. Watanabe et al., (Super-K Collab.): Astropart. Phys. **31**,320 (2009).

[15] J. C. Chow et al., AECL Nucl. Rev. **1**,(1) 21 (2012).

[16] D. R. O'Conner et al., Appl. Radiat. Isot. **41**, 1041 (1190).

[17] S. A. Enger ., Radiation Measurement **59**, 233 (2013).

[18] G. D. Stasio ., Neurological Reesearch **27**, 387 (2005).

[19] C. Xu et al(Super-Kamikande collaboration), *Journal of Physics* 718,062070(2016).

[20] super kamiokande, < http://www-sk.icrr.u-tokyo.ac.jp/sk/gallery/index-e.html >.

[21] S. Fukuda et al, (Super-Kamikande collaboration) *Phys. Lett. B*, 539,179 (2002).

[22] Y. Fukuda et al (Super-Kamikande collaboration) . *Phys. Rev. Lett.*, 81,1562 (1998).

[23] K. Abe et al, (T2K collaboration) . *Phys. Rev. Lett.*, 107,041801 (2011).

[24] Y. Kim *Nuclear Engineering and Technology***48**,285(2016).

[25] C. L. Cowan et al., *Science***124**103(1956).

[26] S. Oguri et al., < https://arxiv.org/abs/1404.7309 >.

[27] PANDA detector,< http://indico.phys.vt.edu/event/29/session/2/contribution/2/material/slides/0.pdf >.

[28] P. Saikumar et al., *Separation Science and Technology***48** (8), 1220(2011).

[29] CANDU Reactor, < https://daryanenergyblog.wordpress.com/ca/part-5_hwr/ >

[30] CANDU Reactor shutdown system,< https://www.slideshare.net/hitesh128/candu-reactors >.

[31] J. L. Kloosterman, Annals of Nuclear Energy **30**, 1807 (2013).

[32] Y. Horiguchi et al., Sci. Technol. Adv. Mater. 12, 044607 (2011).

[33] C. Salt, A. J. Lennox, and M. Takagaki, J. A. Magure and N. S. Hosmane., *Russian Chemical Bulletin*, 53(9),1871(2004).

[34] BNCT,< https://en.wikipedia.org/wiki/Neutron_capture_therapy_of_cancer >

[35] L. V. Groshev et al., Izv. Akad. Nauk SSSR, Ser. Fiz., 26, 1119 (1962).

[36] J. Voignier et al., Nuclear Science and Engineering **93**, 43-56 (1986).

[37] L. M. Bollinger et al., *Phys. Rev. C***2**, 1951(1970).

[38] J.Kroll et al., Phys. Rev. C 88, 034317 (2013).

[39] A. Chyzh et al., *Phys. Rev. C***84**, 014306 (2011).

[40] B. Baramsai et al., *Phys. Rev. C***87**, 044609 (2013).

[41] N. D. Scielzo et al., *Phys. Rev. C***81**, 034608 (2010).

[42] B. Baramsai et al., *Phys. Rev. C***85**, 024622 (2012).

[43] Natinal Nuclear Data Center,< https://www.nndc.bnl.gov/>.

[44] Thermal Neutron Capture γ's(CapGam),< http://www.nndc.bnl.gov/capgam/>.

[45] D. J. Griffiths *Introduction to Quantum mecjanics ,Pretice Hall* **(5th edition, 2006)**

[46] H. Feshbach, C.E. Porter, V.F. Weisskopf, *Phys. Rev.* **90**,166(1953).

[47] P. E. Hodgson, *Rep. Prog. Phys.* **34**, 765-819, 1971.

[48] S. N. Ghoshal, *Nuclear Physics, S.Chand and Company LTD.*(**Reprint, 2003**).

[49] M. U. Khandakar, *Int. Journ. Fund. Phys. Sci.***1(2)**,41(2011).

[50] G. F. Knoll, *Radiation detection and Measurement, Willey*(**4th edition, 2010**).

[51] Ge detector, < https://www.ortec-online.com/-/media/ametekortec/brochures/gem.pdf >.

[52] S. Agostinelli et al., Nucl. Instrum. Meth. **A506**, 250 (2003).

[53] Geant4 web page, < http://geant4.cern.ch/>.

[54] JPARC wiki, < https://en.wikipedia.org/wiki/J-PARC >.

[55] JPARC center,< https://j-parc.jp/index-e.html>.

[56] M.Igashira, < http://libra.inp.demokritos.gr/THERRAA/presentations/THERRAA(Igashira).pdf>.

[57] Y. K. M. Igasira and M. Oshima, Nucl. Instrum. Methods Phys. Res. A**600**, 332 (2012).

[58] Schematic view of MLF, < https://inspirehep.net/record/1257384/plots >.

[59] K. Kino et al., Nucl. Instrum. Meth. **A626-627**, 58 (2011).

[60] A. Kimura et al., J. Nucl. Sci. Technol. **49**, 708 (2012).

[61] F. Maekawa et al., Nucl. Instr. Meth. Phys. Res. A **620**, 159 (2010).

[62] Schematic view of ANNRI, < https://j-parc.jp/researcher/MatLife/en/instrumentation/images/BL04.pdf >

[63] I. Ou et al., *AIP Conference Proceedings* **1594**, 351 (2014).

[64] "ISOFLEX", < http://www.isoflex.com/>.

[65] Table of Radioactive Isotope, < http://nucleardata.nuclear.lu.se/toi/nuclide.asp?iZA=630152>.

[66] GLG4sim page, < http://neutrino.phys.ksu.edu/ GLG4sim/>.

[67] K. Eguchi et al., *Phys. Rev. Lett***90**, 021802 (2003).

[68] J. Kopecky et al., *Phys. Rev. C***47**, 312(1993).

[69] T. Belgya et al., *IAEA-TECDOC-1506***110**, 3107(2009).

[70] R. Capote et al., *Nucl. Data sheets* .

[71] K. Hagiwara et al., *PoS Conference Proceedins*, **submitted** (2017).

Acknowledgements

It is my great opportunity to express my thank and gratefulness to them who helped me for making possible of this dissertation.

I owe my deepest gratitude to my supervisor, Professor Makoto Sakuda ,Dept. of Physics, Okayama University who patiently gave me advices which inspired many ideas in this thesis. He taught me how to face the problems, how to investigate them, and how to solve them. Professor Sakuda also gave me wonderful advices, comments, and guidance while writing a paper and also presenting the paper. Moreover, he not only supplied me the scientific knowledge, but also enlightened me with the important knowledge in life.

This work was completed with the help of many people to whom I owe a great debt. My first and foremost thanks go to Prof. Sakuda Makoto for his support and valued advice throughout my graduate study. I am also grateful for giving me chance to do my experimental work at J-PARC.

I would like also to show my gratitude to my co-supervisors, Associate Professor Hirokazu Ishino and Assistance Professor Yausuke Koshio for spending the time for helping me and for giving me advices, suggestions and comments in doing the projects, writing papers, and proofreading of this work.

I would like to acknowledge Ministry of Education, Culture, Sports, Science and Technology of Japan (MEXT) for financially supporting my doctoral course, and also Pabna University of Science and Technology, Bangladesh for allowing me to do my doctors course.

I would like also to show my gratitude to my M.Sc. (Master) thesis supervisor Dr. Arun Kumar Basak, Professor Emeritus, Dept. of Physics, Rajshahi University, Bangladesh and M.Sc. thesis co-supervisors Dr Abdullah Shams Bin Tariq, Professor, Dept. of Physics, Rajshahi University, Bangladesh for helping me and for giving me advices, suggestions and encourage me throughout my research career. This is a privilege for me to express my sincere gratitude to my esteemed teacher Prof. Somnath Bhattacharjee, Department of Physics, University of Rajshahi, for his guidance, constant vigilance, direction and suggestions.

A huge debt of gratitude is owed the J-PARC collaborators and researchers of the ANNRI group for their hospitality and for the friendly environment. I would especially like to thank Dr. Atsushi Kimura for his encouragement of my research and many valuable discussions. From these people, I always found an answer to my questions related to nuclear physics clearly and quickly. Doing research with this effective working group was a great help in finishing my Ph.D. program in a relatively short time. I am especially indebted to Dr. Takatomi Yano, Kobe University, Prague, for his help on the Geant4 (MC) simulations.

I also offer thanks to all the members of our group specially my best friend and research mate Kaito Hagiwara for his helpful co-operation. And also thanks to Yoshiyuki Yamada for his co-operation. I aslo offter thank to Tomoyuki Tanaka for his help and co-operation.

I would like to offer special thanks to Dr. Rohit Dhir, Assistant Professor, Department of Physics, SRM Research , India and Ex-Research Assistant professor at Okayama University for his continuous inspirations and helps. I'd like to thanks Iwa Ou,Takashi Sudo student , Department of Physics , Okayma University for their encouragement and valuable advice throughout my research work. I would like to

express my special thanks to Mandeep Sing Reen, Doctor Student, Department of Physics, Okayama University, for his friendly helps and inspiration.

I would also like to offer special thanks to Dr. Sebastian, Assistant Professor, Department of Physics, Okayama Univeristy, for his continuous inspirations and helps. I'd like to thanks William Focillon M.Sc. student, Department of Physics, Okayma University for their encouragement and valuable advice throughout my research work.

I am deeply grateful to my mother, Sobi Rani Das and my father, Late Nimay Chandro Das for their constant prayer, encouragement and inspiration. My mother has been taking care of me and my family after my father death. I am always grateful to her for taking both the role. I will never be able to repay my debt to her by any means. She teaches me how to keep patience in critical moment and helps me to become laborious. She sacrifices every things for my happiness.

I am also grateful to my brother Pijush Kumar Das, my sister Chanda Rani Singho, brother-in-law Shadhin Kumar Singho, sister-in-law Suchana Das and my dear nieces Susmita Singho, Orpita Singho and my dear nephews Susmoy Singho and Priangshu Das for their supports, encouragements and inspirations. I also thankfully acknowledge the prayers of many relatives, colleagues, students, well-wishers and friends.

Without their help and encouragement, this thesis would not have been completed.